QUANTITATIVE FALL RISK ASSESSMENT WITH WEARABLE SENSORS

by

Zheng Xu

A dissertation submitted to the faculty of
The University of North Carolina at Charlotte
in partial fulfillment of the requirements
for the degree of Doctor of Philosophy in
Mechanical Engineering

Charlotte

2018

Approved by:

_____
Dr. Nigel Zheng

_____
Dr. Ronald E. Smelser

_____
Dr. Terry Xu

_____
Dr. Susan Trammell

_____
Dr. Jun-tao Guo

ABSTRACT

ZHENG XU. Quantitative fall risk assessment with wearable sensors. (Under the direction of DR.NAIQUAN NIGEL ZHENG)

Falling has become one of the leading causes to both fatal and non-fatal injuries among the elder adults and patients with dysfunctional mobility. The following consequence of a fall will be that the fear of falling can reduce the daily activities, leading to physical deterioration and social isolation. Falls and its related injuries can be predictable and preventable with specific interventions targeting the corresponding risk factors including muscle strength, balance and mobility. The initial step of an effective fall prevention program is to perform fall risk assessment to identify persons at high risk and then target specific interventions to reduce or eliminate falls. Due to several reasons such as unreliable subjective measures, high cost and clinical time constraints, effective fall risk assessment is still not routinely integrated into daily clinical practice. The inexpensive and easy-to-use wearable inertial measurement unit (IMU) provides the promising technique to assess fall risk, however there are still many issues for clinical practice at present. This objective of this dissertation was to investigate the feasibility, reliability and repeatability of using IMU sensors to assess fall risk for clinical use.

The accuracy of an IMU sensor was validated on the rigid body and human body using an optical motion capture system. A complimentary filter with gradient descent algorithm was used to verify the accuracy of built-in sensor fusion model. A simple template of magnetic mapping was built to quantify the magnetic disturbances and then a simplified interpolation model was developed to compensate the heading angle error in the complicated lab settings. Then different combinations of sensor configurations were evaluated among three different groups of subjects with six sensors placed on the body. The optimal configurations was explored according to the classification performance from three machine learning techniques. Sixty-five older adults from the senior center with single IMU placed in front of the chest were recruited. A self-report questionnaire was

provided as a common clinical assessment to divide sixty-five senior people into two risk levels. Meanwhile, three machine learning models were applied to classify the fall risk of these subjects according to their sensor data during three different physical tests

Both of the static and dynamic orientation accuracy from rigid body tests were within 2° achieved by built-in sensor fusion model while the static and dynamic accuracy for sensor orientations on human body were within 2.5°. The accuracy and precision of IMU measurements are sufficient for human motion applications without excluding the soft tissue artifact and unexpected sensor movement on the human body. For the magnetic disturbances, the heading estimation errors from static tests were significantly larger than that of dynamic test. The compensation method did improve the accuracy of heading angles in the static test. When performing the test with IMUs, starting in an undisturbed magnetic field will reduce the heading angle error and the closer IMU is to the floor, the larger the heading angle error will be. The optimal sensor configuration was achieved by the sensors placed on chest, wrist and shank together. A single sensor configuration can also produce very high accuracy like the chest sensor. Timed-Up-and-Go (TUG) test provided the best classification results for fall risk classification and the combination of multiple tests did not improve the classification performance. Support Vector Machine (SVM) model is the best machine learning technique among three models for fall risk classification. Overall, the wearable IMU sensor-based fall risk classification model has potential to improve the diagnosis of elder adults with risk of falling and allow pre-intervention to prevent future falls.

ACKNOWLEDGEMENTS

I would like to thank Dr. Nigel Zheng for not only his wise mentoring on the research study but also the positive impact of my life during the five and half years. He has provided me extensive personal and professional guidance. I also thank Dr. Ronald E. Smelser, Dr. Terry Xu, Dr. Susan Trammell and Dr. Juntao Guo for serving on my dissertation committee and providing constructive suggestion for my dissertation. I am grateful to Dr. Richard Peindl and Nahir A. Habet for subject recruitment and providing assistance on development of the validation device. I would like to thank both my colleagues and friends - Shangcheng Wang, Robert Jenkins, Shan Wei and Andrew Gao for data collection. I thank Dr. Julian Montoro-Rodriguez for his kindness and great help on the connection with senior center in the subject recruitment. I would like to say 'Thank you' to all the subjects participated in my study and all the staffs in the senior center. Also, I thank all of my friends giving me support and encouragement along the way. Most importantly, I would like to thank my parents whose love and support sustained me throughout the journey and my girlfriend who gave me inspiration all the time.

DEDICATION

To my parents, Hongbing Xu and Xifeng Hu and my girlfriend, Nan Zhang, I could not have finished the dissertation without you. Thank you for all of your support along the way.

TABLE OF CONTENTS

LIST OF TABLES

LIST OF FIGURES

LIST OF ABRREVIATIONS

ABC	Activities Balance Scale
AHRS	Attitude-Heading-Reference-System
ANOVA	Analysis of variance
AP	Anterior-posterior
AR	Augmented reality
ASIS	Anterior super-iliac spine
COMB	Combination
CV	Coefficient of variation
DOF	Degree of freedom
DVR	Dominant vertical rise
EKF	Extended Kalman Filter
ETF	Exaggerated trunk flexion
FFT	Fast Fourier Transform
FIR	Finite impulse response
FN	False Negative
FP	False Positive
FTSTS	Five-time-sit-to-stand
GRF	Ground reaction force

IMU	Inertial measurement unit
IMU_INT	The angle directly integrated from angular velocity
IMU_Quat	The angle computed from quaternion
KNN	k-Nearest Neighbor
Mean_diff	Mean difference
MEMS	Micro-Electro-Mechanical System
ML	Medial-lateral
MT	Momentum transfer
NB	Naïve Bayesian
P2P_VA	Peak to peak vertical acceleration
P2T	Peak to trough
PD	Parkinson's disease
PSIS	Posterior super-iliac spine
r	Correlation coefficient
RF	Random Forest
RMS	Root mean square
RMSE	Root mean square error
ROM	Range of motion
TN	True Negative
TP	True Positive

TUG	Timed-up-to-Go
SD	Standard deviation
SI	Superior-inferior
STS	Sit-to-stand
SVM	Support Vector Machine
UKF	Unscented Kalman Filter
V	Vertical
VR	Virtual reality
2D	Two dimension
3D	Three dimension
10MWT	10-meter walking test

CHAPTER 1: INTRODUCTION

1.1 Falling problems

Falling has become one of the major causes to both fatal and non-fatal injuries among the elder adults and patients with postural impairments and traumatic injuries. According to the US Centers for Disease Control and Prevention, each year a quarter of older adults over age 65 fall down (National Council on Aging, 2016). Every 29 minutes, there is an older adult dead following a fall (National Council on Aging, 2018). In 2014, the total cost of fall injuries was $ 31 billion and it may reach $ 67.7 billion with the increase of aging population. Falls result in more than 2.8 million injuries annually including 800,000 hospitalizations and more than 27,000 deaths (National Council on Aging, 2016). The fear of falling will also limit the old people's daily activities which may result in further physical decline and social isolation (National Council on Aging, 2016). There was a report from the United Nation predicting that the senior population over 65 will reach 2.1 billion by 2050 in the world (Pettinger, July 20, 2016). Except for the aging problem, some specific disease like stroke are potential factor leading to falls. For patients, every year about 700,000 to 1000,000 patients fall in United States hospitals (Currie, 2008). It is estimated that around 30 to 35 percent of those patients injured due to falls (Hitcho et al., 2004). The average cost for patients with a severe fall was $14,056 per patient (Haines et al., 2013; Morello et al., 2013).

1.2 Fall risk assessment background

Owing to the high cost caused by falling, it is necessary to figure out the factors related to the fall risk. In general, fall risk factors can be mainly categorized as extrinsic and intrinsic factors (Perell et al., 2001). Extrinsic factors are disturbances from outside environment which are primary causes for over 50% of all falls during experiment (Aurora Bueno-Cavanillas, Sep 1, 2000). The outside disturbances are difficult to predict due to the uncertainties and complication of

environment. Here, the study mainly focuses on the fall correlated with intrinsic factors. The intrinsic risk factors may include the chronic diseases, muscle weakness, cognitive impairment and aging problem (Perell et al., 2001). Many fall prevention techniques occurred to improve the safety of those people prone to fall, but a foundation should be built on the deep understanding of the fall risk assessment with various falling group. A simple example is that patients with Parkinson's disease (PD) will exhibit distinctive motion characteristics and risk level as that of patients with ankle injury. After fall risk assessment, specific interventions can be assigned to each individual group of patients.

Several physical performance tests have been introduced to assist clinicians to assess the mobility functions which is closely related to the prediction of fall risk since the 1970s. During the physical performance tests, the subjects are typically instructed to complete a series of basic motor tasks like level walking, turning, sit-to-stand and stand-to-sit (Rob van Lummel, Mar 30, 2017). Sometimes cognitive tasks were added to diagnose how multi-tasks would affect the motion. Nowadays many commonly used fall risk assessing methods consist of multiple tasks like Tinetti Test (Tinetti, 1986), Activities Balance Scale (ABC) (Powell, 1995) and Berg Balance Test (Thorbahn & Newton, 1996). These methods mainly measure the functional limitations and only some can test the risk of falling. They are widely performed by clinicians with regarding to medical diagnosis.

Balance assessment items		Score
I1	Sitting balance	0 to 1
I2	Arises from the chair	0 to 2
I3	Attempts to arise	0 to 2
I4	Immediate standing balance (1^{st} 5*s*)	0 to 2
I5	Standing balance (eyes closed)	0 to 2
I6	Romberg	0 to 2
I7	Standing balance (eyes opened)	0 to 1
I8	Turning 360 degrees continuously	0 to 2
I9	Sitting down	0 to 2
	Total Balance score	0 to 16

Gait assessment items		Score
I10	Initiation of gait	0 to 1
I11	Step length and height	0 to 4
I12	Step Symmetry	0 to 1
I13	Step Continuity	0 to 1
I14	Path related to the floor	0 to 2
I15	Trunk	0 to 2
I16	Walking stance	0 to 1
	Total Gait score	0 to 12

Category	Component	Score
Sitting balance	Sitting unsupported	0-4
Standing balance	Standing unsupported	0-4
	Standing with eyes closed	0-4
	Standing with feet together	0-4
	Standing on one foot	0-4
	Turning to look behind	0-4
	Retrieving object from floor	0-4
	Tandem standing	0-4
	Reaching forward with an outstretched arm	0-4
Dynamic balance	Sitting to standing	0-4
	Standing to sitting	0-4
	Transfer	0-4
	Turning 360 degrees	0-4
	Stool stepping	0-4
Total		0-56

Figure 1.1 left - The list of left table shows the score range of balance and gait assessment items in the Tinetti test (Tinetti, 1986); right - The list of right table shows the score range of sitting, standing and dynamic balance in the Berg Balance Test (Thorbahn & Newton, 1996).

As we see from the list of tasks, it is truly time-consuming for the senior subjects to complete all the tests. Not to mention some patients, when they are required to walk, rise from chair and other activities, it is burdensome for them especially during some long tests. Of course, there are the other types of clinical assessment tools which takes a little time but still a promising evaluation way. Timed-up-to-Go (TUG) (Podsiadlo & Richardson, 1991) is a successful test. It requires the subject to start from sitting on a chair, stand up, walk forward, turn around a cone, walk back to the seat and sit down which usually takes normal people less than ten seconds to complete whole process. Besides, another two simple tests - Ten-meter Walking Test can be employed to determine functional mobility and vestibular function. It is used to assess walking speed in meters per second over a short distance. All these actions are basic daily movement often compromised for elderly with functional limitations and motor dysfunctional patients. However, no matter what kind of clinical measurements are, the performances are commonly recorded by measuring time with stopwatch or measure distance with tape measure and some visual judgment

by raters which introduce more human error. For example, the Tinetti test interprets that a score of zero indicates the most impairment, while the higher numbers one and two indicate less impairment. Patients who score below 19 are at a high risk of falls; patients who score in the range of 19 – 24 have a moderate risk of falls; patients who score between 24 and 28 have a minimal risk of falling (Tinetti, 1986). It is difficult to give an accurate score of the assessment for each test which have the inherent drawbacks of being subjective and evaluator-dependent, and thus associated with potential bias. Besides, the poor specificity and poor sensitivity of different methods may reduce the accuracy of the clinical assessment. A research study about faller classification with Tinetti Test in 2000 showed that the specificity was only 11% for non-fallers (Shumway-Cook, Brauer, & Woollacott, 2000). Another example of poor sensitivity with Berg Balance Test was proved by Thorbahn, LDB et al where the sensitivity is as low as 53% (Thorbahn & Newton, 1996). It will be of great value to develop more convenient and consistent measurement way to support the clinicians' diagnosis and improve fall risk assessment.

With the development of techniques, a lot of equipment have been used to quantitatively measure the balance and motion of human such as optical motion capture system and Gait Rite etc. Optical motion capture systems are commonly used to analyze human motion in a typical motion lab. It is accurate enough usually regarded as golden standard in many studies. However, it suffers from inaccuracies linked to soft tissue artefacts and marker displacement due to the difficulties of locating anatomical landmark (Carcreff et al., 2018). Moreover, this system is quite expensive and has little mobility due to its size and cable connection which is not suitable for outdoor test and daily monitoring. Gait Rite is a kind of movable mat with built-in force sensors which is basically utilized to perform gait analysis. Its output is mainly limited to some variables for lower extremity without considering much about upper body motion. To overcome these limitations, it is necessary to develop better system for clinical use.

1.3 Research challenges

The state-of-art technology, wearable sensor, shows us other ways to assess fall risk of people in clinical use. Currently, wearable sensors are widely used in various fields such as robot control, medical server, human positioning, sports training and physical monitoring. For instance, wearable goniometer are light and cheap sensors but can only output angles while the other type of sensor – force sensitive resistor can only measure forces. These two wearable sensors are quite limited to measure the balance and gait of people.

A more powerful wearable sensor - Inertial Measurement Units (IMU) showed up when it was originally developed for the rockets in the early 1950s. Then the IMUs were gradually used in the navigation and aerospace field. With the development of Micro-Electro-Mechanical Systems (MEMS) technology, IMUs have become a very important and wide spread sensor technology where they are applied in from industry to ergonomic, from biomechanics to life science and from animation to virtual reality (VR) / augmented reality (AR) (Oberländer, September 2015). The IMUs' ease of use, light weight and mobility depending on miniaturized and wireless transmission technology have attracted high interest of scientists from different areas in its related technology. A common IMU consists of tri-axial accelerometer, tri-axial gyroscope and sometimes tri-axial magnetometer. With magnetometer, it is also called Attitude-Heading-Reference-System (AHRS). Attitude represents the roll and pitch angle, heading represents yaw angle. This combination makes it possible to track rotational and translational movements. In a 3D space, an accelerometer can only measure attitude relative to the direction of gravity. The importance of magnetometer is to provide an absolute heading angle relative to earth's magnetic field. The accelerometers are used to determine the acceleration of a rigid body. Velocity and distance can be computed by integration but needs an external reference point due to the drift caused by accumulating noise in the signal.

They are very sensitive to vibration and mechanical noise. Gyroscopes in general are devices that measure angular rate along different axes. They are stable in the short term but has low-frequency drift in the long term. For magnetometers, they can be used to measure the angle between heading direction of a subject and the magnetic north of the earth. But they are easily interfered by external magnetic field in the vicinity.

It is one of the reasons that IMUs are still not widely used in the clinical application. In a clinical setting, there are a lot of equipment which may cause magnetic disturbances to the magnetometer. Large magnetic disturbances will lead to large heading angle error. Also, the optimal configuration of IMUs such as number of IMUs, IMU placement on the human body when measuring human motion has not been investigated. No standardized variables have been defined by any studies to assess fall risks. The unknown connection between IMU data and clinical analysis limits the application to the use of fall risk assessment.

1.4 Research goal

This study aims to investigate the feasibility, reliability and repeatability of using IMU sensors to assess fall risk for clinical use. With so many gaps between usage of IMU and clinical use, it is important to find solutions to fill the gap. There are four major goals discussed in this dissertation.

The first goal is to check the accuracy of IMU sensors and validate it with a reference system. For all the wearable inertial sensors, a full set of calibrations and validation tests are executed in the factory before sending to the customers. While these tests are unknown to the users, complete assessment of the new sensors are supposed to be done by the users prior to putting into action. As human body is not rigid, validation tests will be performed on the rigid body initially

compared to a stereo-photogrammetry system which is often regarded as the reference system. Then a follow-up test on a human body will be completed. The whole procedure will let us go through the detailed signal processing and coordinate transformation. Minimizing the noise and drift are main tasks in the signal processing. Comparison between IMU and the reference system requires the data converted in the same reference frame which is realized by coordinate transformation. After all these steps, it is necessary to verify if the accuracy of IMU fits the need of clinical use.

The second goal is to build a template to quantify the magnetic disturbances and develop model to compensate the heading angle error in clinical settings. A custom-made device is built to carry out the mapping of magnetic field in the motion lab. The filming volume is divided into small grids and the magnetic field and heading angle at each grid point in static tests are measured. Time as an important factor is considered in the comparison between static and dynamic tests. A compensation model will be developed to adjust the error showing in the static tests. Then It will be applied on the dynamic test data to verify the function of the model.

The third goal is to evaluate the measurement performance of various configurations and explore the optimal configurations for Parkinson's disease patients (PKD). The measurement performance is going to be assessed by both data from the reference system and the output from clustering model. The error and correlation will be computed and compared. Sensitivity and specificity will be calculated in the evaluation of the clustering results.

The fourth goal is to apply the model-based approach for the quantification of fall risk among the community-dwelling senior people. Only a single IMU is placed in front of the chest. A customized questionnaire will be provided as a common clinical assessment which can put the senior people into two groups. According to the difference of extract key features from two groups at different risk level, the proposed approach will quantify the fall risk using pre-trained classifier.

1.5 Significances

This study provides a comprehensive understanding of wearable inertial sensors from multiple aspects, explores various current issues existing in the IMU for the clinical application and develops methods to solve these issues. The typical sensor fusion algorithm unexplained in the commercial IMUs are revealed here and validated by an optimization approach. It will be a nice reference to the sensor fusion techniques. The template for compensating the heading angle will benefit the users when using the IMUs to measure the patients' walking directions in the clinical settings without worrying about the magnetic distortions. The optimal IMU configurations will provide some reference to the users before designing the experiment and accomplishing data analysis. The quantification of fall risk based on a machine learning approach displays the promise of future clinical diagnosis with the use of IMUs.

Overall, if the IMUs can be used in the future clinical analysis, it will save time for clinicians. Besides, it can improve the accuracy and consistency of clinical diagnosis based on the sensor measurement instead of human subjective evaluations. Taking advantage of its simple operation, the sensor may provide an easy tool for elder individuals to measure their fall risk at home without going to the clinics. The most important part of this study is that it generates new knowledge from IMU data to assess the fall risk.

CHAPTER 2: INERTIAL MEASUREMENT UNIT

2.1 Background

In 1930s, IMUs began to be applied in aircraft navigation and large devices (Zhao & Yeatman, 2007). At that time, the usage of IMU was restricted to bulk application which is nothing related to human. MEMS IMU with an attractive feature of low cost, compact and low power consumption, was introduced to smaller size devices and human motion analysis. Nowadays, they are commonly built in many individual devices like smart phones, watch, wrist band and GPS devices. The broad usage of IMU can achieve this goal in terms of acceleration, angular velocity and angle rotations.

A regular IMU usually contains accelerometers and gyroscopes which can measure translational and rotational motion. It requires the sensor to register three mutually orthogonal axes for measuring three-dimensional (3D) movements. Without magnetometer, IMUs can only measure the orientation relative to the direction of gravity including roll and pitch angles. To provide a complete measurement of orientation in 3D space, a tri-axial magnetometer is combined with the IMU to track the heading angle relative to the earth magnetic north based on the magnetic field. With magnetometer, IMU is also called AHRS which are used in this study.

This chapter will discuss various components in the IMU. Some technical concepts and sensor fusion algorithm will be introduced prior to using IMU. A full schema about IMU data processing is going to be presented here as well. Validation tests are going to be completed to check if IMU's accuracy fits the needs of clinical study.

2.2 IMU components

As mentioned above, nine degree of freedom (DOF) IMU is composed by a tri-axial accelerometer, a tri-axial gyroscope and a tri-axial magnetometer. Each individual sensor has its own specific function which can be operated separately with proper settings. The following part will introduce the varieties and features of each component.

2.2.1 Accelerometer

An accelerometer is an electromechanical device used to measure accelerations according to the forces acting upon it. These forces can be static like the constant force of gravity or dynamic caused by moving or vibrating the accelerometer. It can provide the tilted angle with respect to the earth by measuring the amount of static or quasi-static acceleration due to gravity. To derive the velocity and distance from accelerometers, this can be simply done by integration of its measurements with an external reference point. In general, accelerometers can be classified as two groups: open-loop and closed-loop. Open-loop accelerometers have displaced proof masses with its displacement measurement while closed-loop accelerometers maintain the proof masses in a fixed position where the force (or current, power, etc.) to keep the position is gauged. According to the operational characteristics, there are three different types of accelerometers: mechanical accelerometer, capacitive accelerometer and piezoelectric accelerometer. The following image (Figure. 2-1) (Titterton, 2004) shows a simple mechanical accelerometer containing a proof mass and a spring. Based on the Newton's second law of motion, it states that the force **F** exerted on an object of mass m with an acceleration **a** is equal to **F** = m * **a**. Then Hooke's law states that the force **F** needed to extend or compress a spring by some distance x scales linearly with respect to that distance. The spring will generate an opposite force of same magnitude as the applied force to maintain its original state. The restoring force **F** can be expressed as **F** = k * x where k is the

stiffness of the spring. Therefore, the acceleration can be calculated through two equations if the mass, spring's stiffness and the displacement are known.

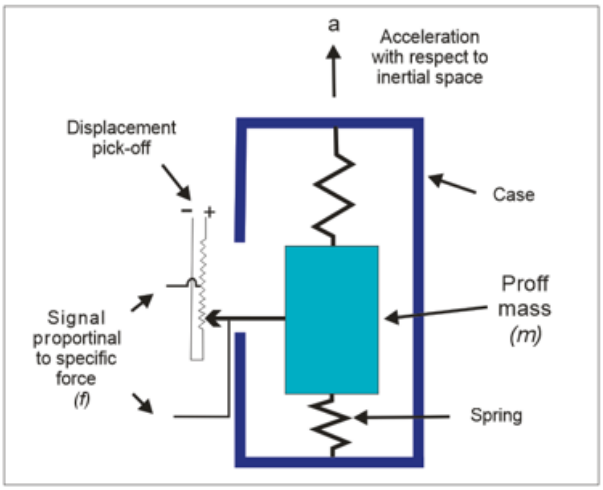

Figure 2.1 A typical accelerometer (Titterton, 2004)

Next one is the capacitive accelerometer. As you can see from the image (Figure. 2.2) below, it consists of a pendulum with a proof mass attached to it. A flexible component such as a pivot or hinge is connected to the pendulum. On the side of accelerometer, there is a pick-off device to detect the pendulum motion based on the change of capacitance between the pendulum and two electrodes by using a bridge circuit. Two symmetrical coils mounted onto pendulum to restore the original position of pendulum. When a current is running through the coils, it will generate an electromagnetic force to maintain the pendulum's original position and keeping the displacement at zero. The acceleration is proportional to the current which is the measurement for most device (Oberländer, September 2015). Usually, the case will be filled with low viscosity fluid to absorb shocks or vibrations.

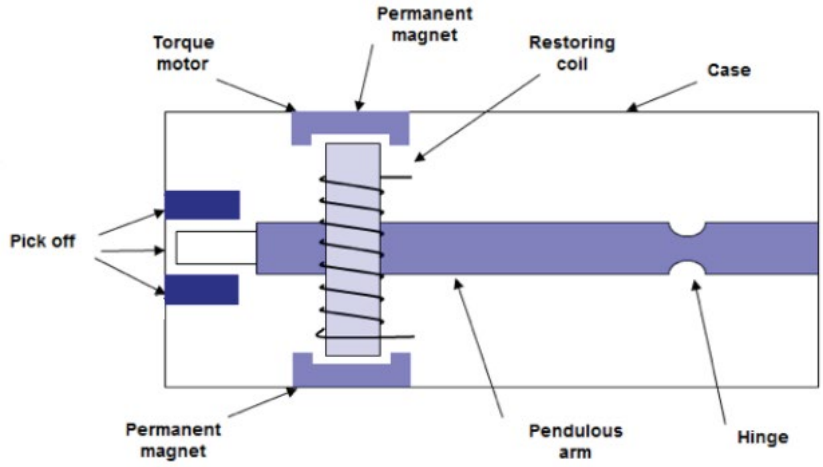

Figure 2.2 A capacitive accelerometer (Oberländer, September 2015)

The third type is the piezoelectric accelerometer. Piezoelectric effect is the ability of certain materials like quartz crystal to generate an electric charge in response to applied mechanical stress. The device is generally composed of a piezoelectric quartz crystal with the applied accelerative force on it. The crystal produces a voltage that is proportional to the accelerative force due to the special self-generating property (Oberländer, September 2015).

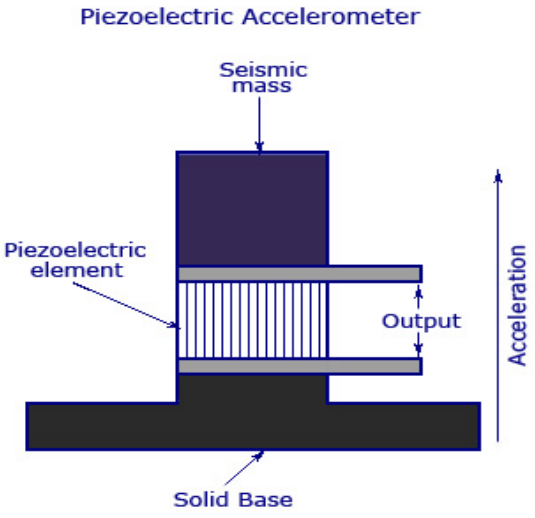

Figure 2.3 A piezoelectric accelerometer (Sivaranjith, Mar 12, 2018)

2.2.2 Gyroscope

A gyroscope is device measuring the angular velocity primarily for navigation before. Generally, most gyroscopes only measure along single axis. Three gyroscopes orthogonally mounted together are used to track 3-D angular motion (Oberländer, September 2015). There are three basic types of gyroscopes according to the working principles: mechanical gyroscope, vibratory gyroscope and optical gyroscope.

Mechanical gyroscopes are the most common or familiar type of gyroscopes. The image below shows a tri-axial gyroscope which includes a spinning wheel mounted in a set of gimbals. These three gimbals provide additional degree of rotational freedom for the spinning wheel and can rotate with respect to one another. The angle pick-off devices are installed at each end of the rotating axis. Relying on the conservation of angular momentum, a rotating body without any torques applied will be forced to remain in its constant state. When external torques or rotations are present in these devices, the gyroscope will maintain its orientation and measure the angular velocity due to the phenomenon of precession. If a spinning object has an external torque applied in a direction perpendicular to the spin axis, then precession occurs. In accordance with Newton's second law of motion, a torque will be applied to the wheel if the angular momentum will change to the direction of the applied torque vector. As the result of this torque, the wheel will rotate about the axis perpendicular to both the input axis (torque axis) and the spin axis of the wheel. A restraining spring attached to angle pick-off device acts against the torque while the angle pick-off devices will detect the angular changes relative to the original position (Oberländer, September 2015).

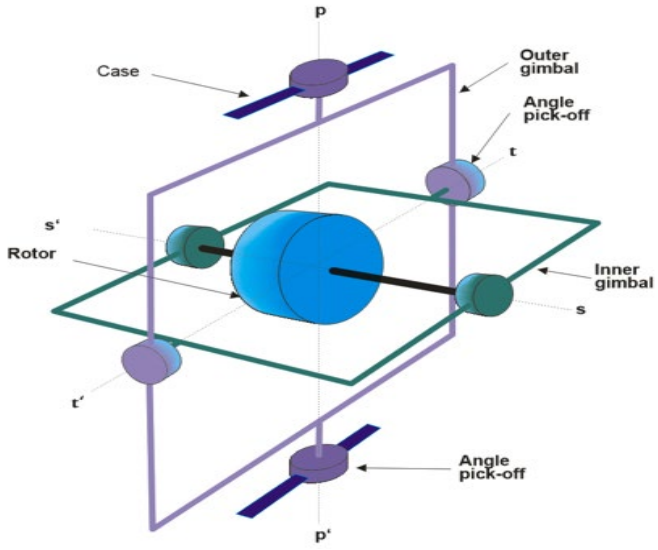

Figure 2.4 The schematic diagram of tri-axial gyroscope (Titterton, 2004)

Vibratory gyroscopes are MEMS devices on the foundation of Coriolis Effect stating that an inertial force acts on objects performing translation relative to a rotating reference frame. It usually contains a proof mass connected to an outer housing by a set of springs. This outer housing is connected to the fixed circuit board by a second set of orthogonal springs. The mass is continuously driven sinusoidally along the first set of springs. Any rotation occurring in gyroscope will induce the Coriolis acceleration to push the mass in the direction of the second set of springs. So the Coriolis force direction depends on the mass linearly moving direction along the first set of springs. The Coriolis force is detected by the capacitive sense fingers along the outer housing and the rigid structure. According to the different capacity for different sets of sense fingers, the sensor can track both magnitude and direction of angular velocity of the system with the mass moving back and forth perpendicular to the rotating axis (jadmin, April 19, 2016; Oberländer, September 2015).

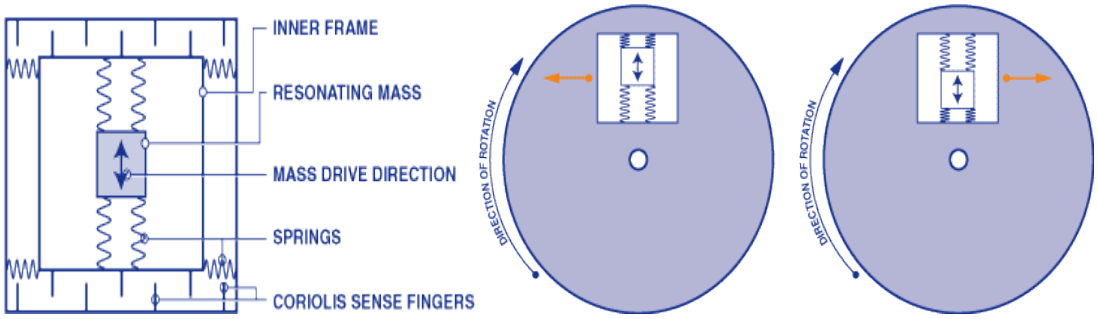

Figure 2.5 Left figure shows the schematic diagram of a typical vibratory gyroscope; Right figure shows the principle when vibratory gyroscope works (jadmin, April 19, 2016)

The discovery of laser technology led to the invention of optical gyroscopes in 1976 (Eric Udd, Nov 2, 2016). The advantage of optical gyroscopes is that there are no moving parts inside which makes it not susceptible to mechanical wear or drifting. Their functionality depends only on the constancy of the speed of light instead of conservation of angular momentum. It is operated on the basis of Sagnac effect stating that if a stationary light source emits two beams of light following the same path but in opposite directions, it will take same time for two beams of light arrive back to the source; one beam of light will slow down with respect to the other beam of light when the light source rotates. The difference in traveling time is proportional to the angular velocity. For these optical gyroscopes, they are typically used in naval and navigation applications, not commercially available (jadmin, April 19, 2016).

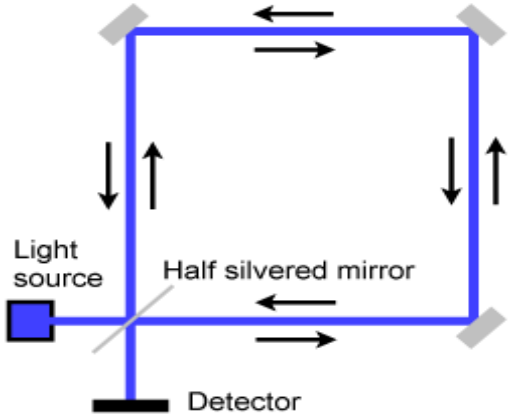

Figure 2.6 The working principle of a optical gyroscope (jadmin, April 19, 2016)

2.2.3 Magnetometer

A magnetometer is a device measuring the magnetic flux density at certain location which can be used to locate the magnetic north pole of the earth. It is capable of detecting fluctuations in the earth magnetic field because the magnetic flux density is proportional to magnetic field strength. Materials that possess magnetic fields or distort magnetic flux lines will distort the magnetic field generated by earth. During the test, the measurement of magnetometer is easily interfered by these materials in the environment. In general, magnetometers are classified into two categories. Scalar magnetometers measure only the scalar value of the magnetic flux passing through the sensor regardless of the direction while vector magnetometers measure the magnitude and direction of the magnetic field. For the scalar magnetometers, they are mostly used in the industry due to its size and function so they will not be introduced here. A typical example of vector magnetometers is the fluxgate magnetometer that can measure the strength of earth magnetic field in 3-D space by orienting the sensor along the direction of desired component (Preeti Jain, 2012). It basically contains a magnetically susceptible core lies within two excitation coils. One coil is excited by the AC supply where the core is magnetically saturated proportional to the alternate peaks of the signal (Oberländer, September 2015). The constantly changing field induces an electrical current in the second coil. Without external magnetic fields, the induced output current will be proportional to the original current. When the sensor is subjected to an external magnetic field, it will alter the current patterns. Therefore, it all depends on the strength of the background magnetic field.

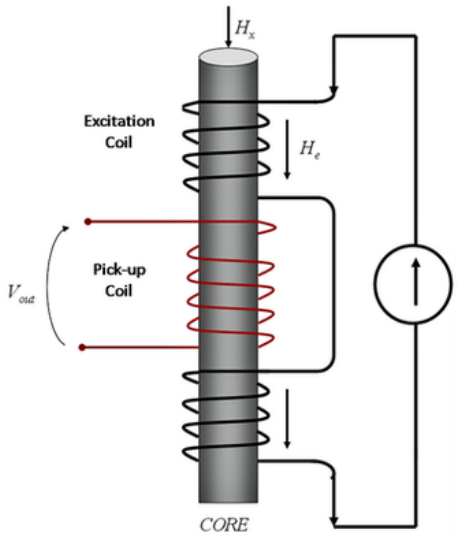

Figure 2.7 The schematic diagram of a typical vector magnetometer (Preeti Jain, 2012)

The most commonly used magnetometers nowadays are Hall effect magnetometers (Oberländer, September 2015). The basic idea of the Hall effect is that a force – known as Lorentz force will be generated to act upon the charge carrier with current flowing through in a magnetic field. The Lorentz force will compel the charge carriers to one side of the conductor, creating a voltage called Hall voltage (Leccadito, 2013; Oberländer, September 2015). The Hall voltage is a low level of signal and linear with respect to the field for given current and dimensions. Meanwhile, the detection of Hall voltage has low sensitivity and temperature stability.

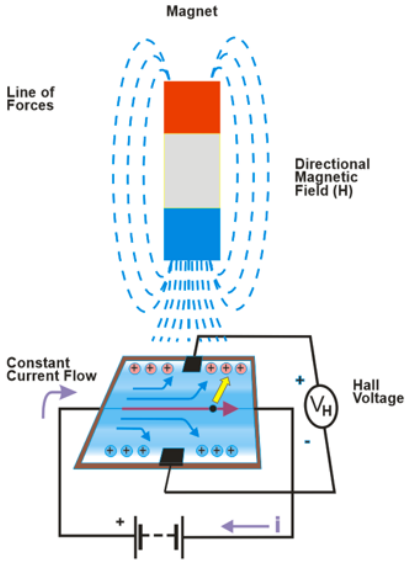

Figure 2.8 The principle of Hall effect for sensors (Oberländer, September 2015)

Hard/Soft Iron effect is described as the distortions of the earth's magnetic field due to external magnetic influences. Hard-iron distortion is created by materials that produce a constant, additive field to the earth's magnetic field. A speaker or magnetized iron, for example, will produce a hard-iron distortion. If this magnetic material is physically attached to the sensor without any relative orientation and position, the field and relative changes will be constant which causes a constant bias in the sensor output. Therefore, it is simple to compensate the hard-iron distortion through subtracting the constant offsets from the raw magnetometer data. Unlike hard-iron distortions additive to the earth's magnetic field, soft-iron distortion is considered as the deflections or alterations to the magnetic field by some materials. This type of materials does not necessarily produce magnetic field themselves so they will not be additive to the earth field. For instance, iron and nickel will generate soft-iron distortion to the surrounding magnetic field. The magnetic measurement of a sensor depends on the acted direction of soft-iron distortion whether it stretches or deflects the magnetic field which is totally different with the constant hard-iron distortion regardless of orientation. Thus, the compensation model for soft-iron distortion will be more complicated than that of hard-iron distortion. In most cases, hard-iron distortion will contribute

more to the total error than soft-iron distortion (VectorNav Technologies, 2011). To reduce the external magnetic disturbances, all the commercial sensors develops their own 3D calibration models to remove the Hard/Soft Iron distortions.

2.3 Commercial IMUs and its application

Accurate motion tracking of rigid objects is greatly important in some areas like autonomous cars, space-crafts and robotics. For ambulatory human analysis, it may be used ranging from daily monitoring of human activities to VR/AR (Sabatini, 2011a). In general, motion tracking systems derive the orientation estimates from electrical measurements of inertial, magnetic and optical sensors (Welch & Foxlin, 2002). In the human motion analysis, the inertial sensors combined with magnetic sensors are becoming popular. The latest MEMS technology succeeds to make the inertial sensors more miniaturized, lower cost and less power consumption which makes it possible to attach to human body. Compared to those stereo-photogrammetry systems, these wearable sensors are much more convenient and more portable to use in the daily movement monitoring. Nowadays, there are many commercial IMUs available in the market. The following table shows the features of some typical IMUs.

For most sensors, they all have their own specific areas for applications. To choose the wearable sensors for the study, a lot of factors were considered such as battery life, wireless connectivity, weight and number of sensors per system etc. Here, APDM Opal sensors (APDM Inc., Portland, OR, USA) are used in this study. These Opal IMU sensors encases 3-axis accelerometer, 3-axis gyroscope, 3-axis magnetometer, and a temperature sensor. The mass is 22 g and the dimensions are 48.4mm x 36.1 mm x 13.4 mm.

Table 2-1 Overview of commercial IMUs in the market

IMU Name	Sensor Fusion	IMU applications	Angle Accuracy	3D Calibration for Hard/Soft Iron effects
MTx (Xsens)	Kalman Filter	biomechanics; VR; animation	static (attitude): 0.5 deg; (heading): 1.0 deg; Dynamic: 2 deg	Yes
VN100 (VecNav)	Extended Kalman Filter	robotics; aerospace; VR	static (attitude): 0.5 deg; (heading): 2.0 deg; Dynamic (heading): 2 deg; (attitude): 1 deg	Yes
3Dm-Gx25-35 (MicroStrain)	Auto Adaptive Extended Kalman Filter	unmanned vehicle navigation, platform stabilization, personnel Tracking	±0.25° RMSE roll and pitch, ±0.8° RMSE heading	Yes
InertialCube2 (InterSense)	Adaptive Kalman Filter	No specific	±0.4° RMS roll and pitch, ±1.0° RMS heading	Yes
Sentral_09 (PNI)	Multi-state Kalman Filter	cell phones, tablets, TV remote controls and video game controls	±0.4° RMSE roll and pitch, ±2.0° RMSE heading	Yes
Opal (APDM)	Kalman Filter	Biomechanics; Motion capture	static (attitude): 1.15 deg; (heading): 1.50 deg; Dynamic: 2.80 deg	Yes

2.4 Experiment design

To identify the noise and drift level in the IMU data, static and dynamic tests were carried out on the rigid body. In many previous studies, inertial sensors were commonly placed on the trunk like sternum, low back, thigh and foot etc (Allseits et al., 2017; Bergamini et al., 2014; Esser, Dawes, Collett, & Howells, 2009; Keijsers, Horstink, & Gielen, 2006; Luinge & Veltink, 2005b;

Seel, Raisch, & Schauer, 2014; Tanaka, Motoi, Nogawa, & Yamakoshi, 2004; Trojaniello, Ravaschio, Hausdorff, & Cereatti, 2015a). As human body is a non-rigid body, sensors attached on these locations may shift and tilt due to skin stretch and elasticity of surface. A transparent box with plastic on the surroundings and wood on the bottom was used in the test to eliminate some of potential factors (Figure 2.9). Plastic box and wood use eliminates the disturbance otherwise may be created by used metals. Since a system error may occur in the test, multiple sensors were needed to check their validity. Besides, a pure rotation test was proposed to make sure the motion in a single plane so that the accuracy of sensors can be evaluated.

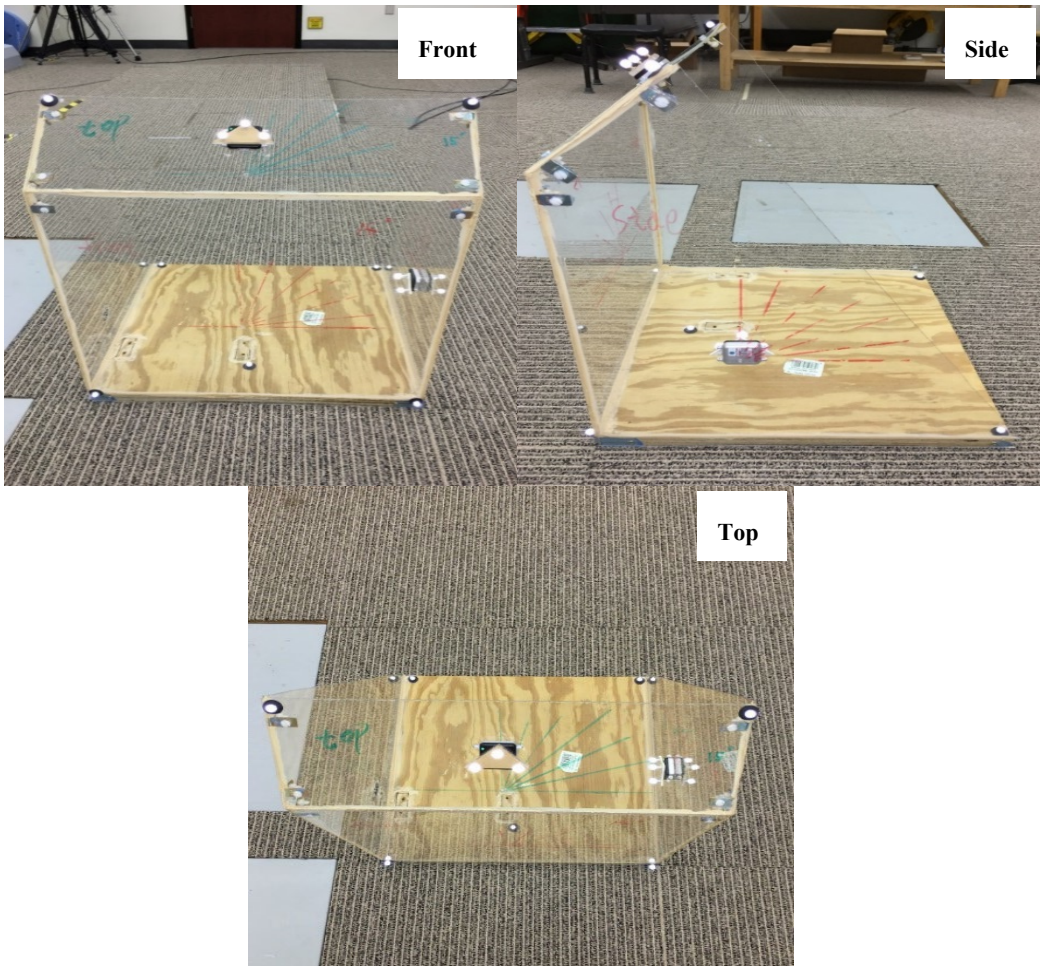

Figure 2.9 Front view, side view and top view of the rigid body

A larger triad was made of plastic with seven single markers attached to it which will increase the accuracy of reference system (Figure 2.10). A single IMU was placed onto the surface of the triad regarded as a rigid body. Also, there was a wood block attached to the bottom of triad used to fit in the track during controlled linear motion. The track was fully made of wood without any metal screws.

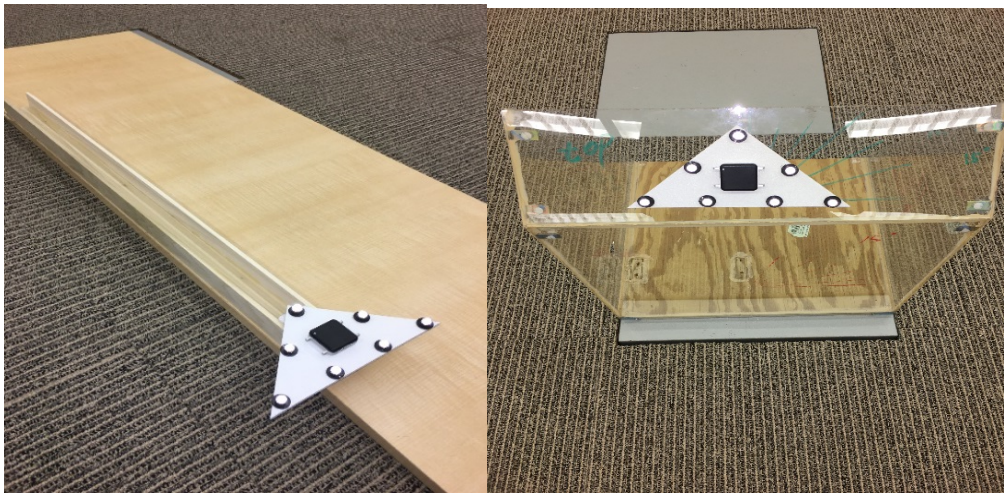

(a) **(b)**

Figure 2.10 (a) Constrained Linear Motion: Large triad with seven markers attached with IMU along wood track; (b) Pure Rotation: Large triad on the top slope of plastic box

The lab coordinate is the coordinate of VICON system. In the VICON system based on Figure 2.9, X axis is forward, Y axis is to the left, Z axis is upward. Pure rotation tests that is manually rotated 90 degrees about each lab axis were accomplished. The bottom line of box close to the floor was aligned with lab axis first and then the box was rotated by hands about the bottom line. In the validation test, in addition to same pure rotation tests with large triad on the same transparent box (Figure 2-10(b)), constrained linear motion was completed with manually push large triad along the wood track. Each constrained linear motion was repeated three times along the bottom edge of the box. Besides, rigid body was kept still to check the offset error of VICON and IMU in both tests.

After the validation on the rigid body, ten subjects including five young healthy subjects and five patients after ankle surgery. Each patient was instructed to walk three meters four times with normal speed. During walking, two inertial sensors attached with two triad respectively were placed on the front chest and low back. Ten single spherical retro-reflective markers were placed on the upper body: bilaterally on the shoulders, elbows, wrists, anterior super-iliac spine (ASIS) and posterior super-iliac spine (PSIS) (Figure 2.11). All the subjects offered their consents before testing. A static T-pose was performed followed by walking.

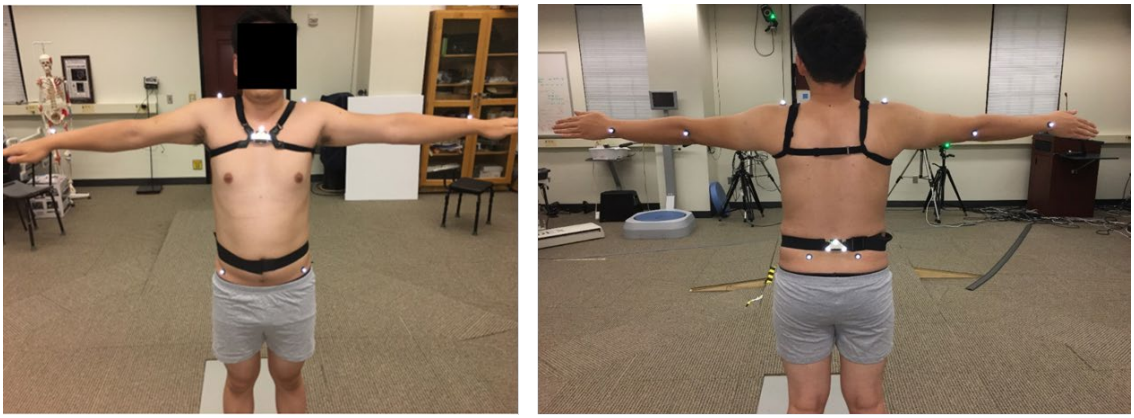

Figure 2.11 Front and back view of marker placement and sensor attachment in the experiment

A ten-camera optical tracking system (VICON, Oxford Metrics Ltd., Oxford, UK) was used as reference system to validate the accuracy of IMU sensor for monitoring the tests on both rigid body and human body. Data about the markers trajectory were collected at sampling frequency 120 Hz while IMU data were collected under Robust Synchronized Streaming Mode at sampling frequency 128 Hz. To synchronize the signal from VICON and Opal IMU, an external signal box (Figure 2.12) was used to send out signal from IMU. VICON will receive a pulse signal when IMU starts and ends. This external box was only used in the validation test.

Figure 2.12 External Sync Box which has three types of BNC connections

2.5 Data processing

To analyze the IMU data, a regular flowchart you can follow is shown below. Gyroscope, accelerometer and magnetometer have different calibration model respectively. ω, a, h are raw angular rate, acceleration and magnetic field. ω_c, a_c, h_c are calibrated angular rate, acceleration and magnetic field. Sensor fusion techniques are algorithms designed to integrate real-time data and measurement outputs into a unified interpretation for multiple sensors which are proprietary and unknown to the public in all the commercial inertial sensors. Sensor fusion are used to estimate the orientation of IMUs mainly regardless of the disadvantages of each individual component. In the next subsections, some sensor fusion techniques will be clearly explained. For all the calibrated signal from sensors, it is crucial to apply noise reduction process to minimize the error caused by noise. The main noise reduction technique used in the IMU data processing is low-pass filter with optimal cut-off frequency. Optimal cut-off frequency was determined by residual analysis (Winter, 1990).

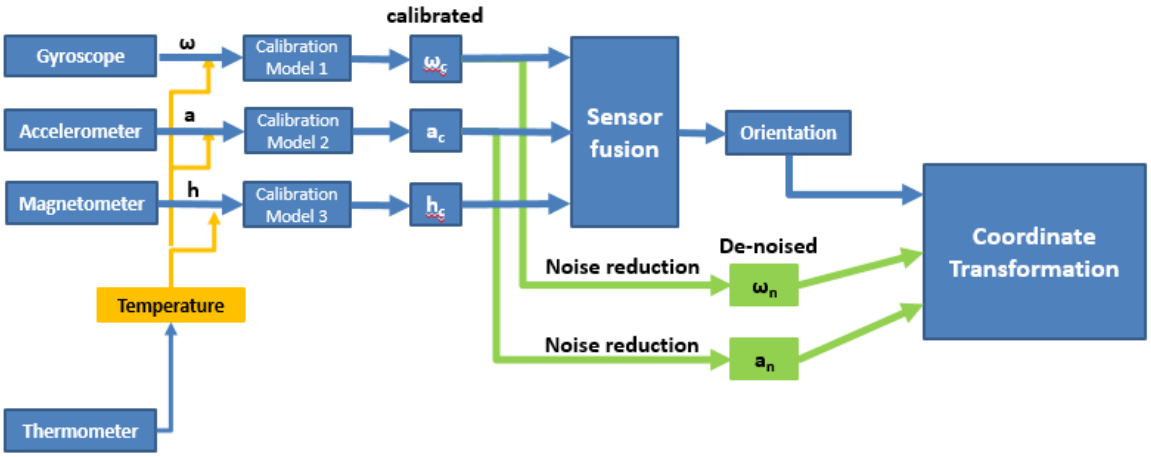

Figure 2.13 The flowchart of sensor data processing

There are two main coordinate frames related to the data measured by IMU. Sensor frame ***s*** is the coordinate frame fixed to the moving IMU. It is aligned with the casing. All the measurements by IMU are gauged in this frame. Navigation frame ***n*** is an absolute coordinate frame which is usually defined stationary with respect to the earth. Many researchers also call it global frame. The orientation of a rigid body in 3D space is actually the orientation of body frame in the navigation coordinate. In order to compare with the VICON reference system, all IMU data in the global frame needs to be transformed to the same VICON reference frame.

Markers position data was low-pass filtered with fourth-order Butterworth filter at cut-off frequency of 6 Hz. The same low-pass filtering with a cut-off frequency of 6 Hz was applied to IMU accelerometer data and gyroscope data to remove noise without losing signal integrity. Due to the different sampling frequency, the IMU data and VICON data need to be synchronized to calculate consistency. IMU measurements was resampled to 120 Hz first and then aligned with VICON angular velocity through cross correlation function. Since there was an external box used in the validation part, IMU data after resampling were synchronized with VICON through trigger signal received by VICON box. The signal will show rectangular pulse shape once IMU is triggered on and off (Figure 2.14).

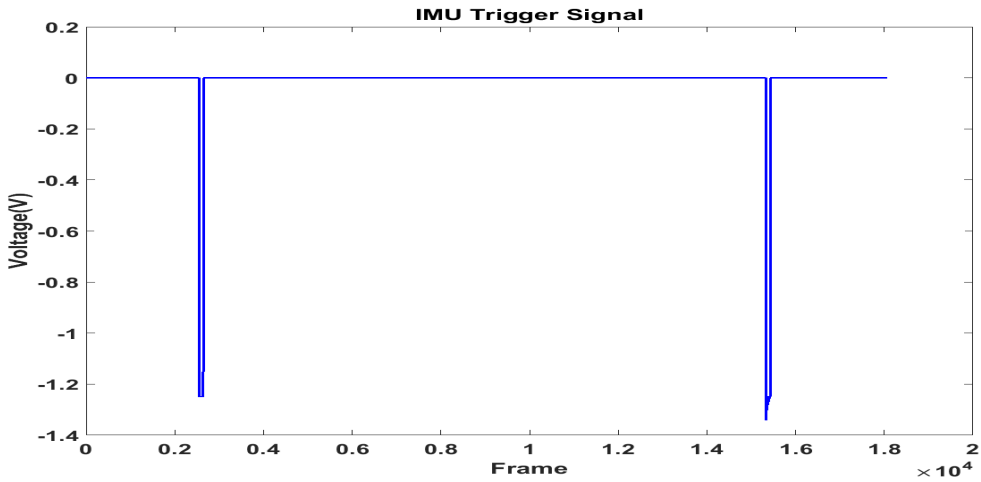

Figure 2.14 IMU External Sync Box trigger signal received by VICON system

In the process of resampling, function 'resample' will apply antialiasing finite impulse response (FIR) low-pass filter to data and compensates for the delay introduced by the filter. Large deviations from zero at the endpoints of data can result in big spikes for resampled data as FIR filter assumes that the input sequence is zero before and after the given samples. Here, ten frames of data points before the end point were usually taken off to reduce the error caused by resampling. The cross-correlation will measure similarity between IMU data and VICON data. Here, vertical accelerations from both system were applied with cross-correlation. Then the number of shifted frames between two measurements was computed from maximum cross-correlation value.

2.6 Sensor fusion

IMU is widely used to estimate the orientation of human body in the 3D space. Obviously, the integral of angular velocity from gyroscope can compute the orientation with known initial conditions. However, the gyroscope signal is prone to error due to low-frequency drift which will increase infinitely with time (Sabatini, 2011b). A gyroscope usually can provide accurate data in a short term while accelerometer can only provide accurate data in the long term. The accelerometer alone can measure inclination angles including pitch angles and roll angles, but it cannot always be

fully trusted due to its sensitivity to vibration and mechanical noise. Besides, the orientation estimates were computed referring to the gravity field. When the motion of objects shows high acceleration component, it is difficult to correctly calculate the orientation through acceleration signals. Therefore, the accelerometer alone to measure inclination angles is only reliable during static or slow motion (Veltink, Bussmann, de Vries, Martens, & Van Lummel, 1996). Adding with a tri-axial magnetometer, the heading angle can be measured in the horizontal plane. Nevertheless, there will be another problem that the magnetometer signal is critically disturbed in the vicinity of ferromagnetic materials especially acute within some indoor environments (Bachmann, Yun, & Peterson, 2004; de Vries, Veeger, Baten, & van der Helm, 2009). Since no single type of sensors can provide precise orientation estimates, it is of great importance to develop optimal sensor data fusion methods to compute the orientation more accurately.

The attitude of a rigid body in 3D space can be represented by rotation matrix, axis angle, Euler angle, quaternion (Diebel, 2006). In the most commercial IMU sensors, the orientation output are usually Euler angles and quaternion. The direct Euler angle calculation may lead to singularity problems and ambiguous results due to multiple rotation sequences although it can show the orientation more explicitly and visually. The quaternion will not have singularity and need higher computational load which is more widely used in the commercial sensors.

Many data fusion algorithms were developed to estimate the orientation of IMU mainly non-linear complimentary filter (Euston, Coote, Mahony, Kim, & Hamel, 2008; Hajdu, Brassai, & Szekely, 2017; Islam, Islam, Shajid-Ul-Mahmud, & Hossam-E-Haider, 2017; Madgwick, Harrison, & Vaidyanathan, 2011; Wu, Zhou, Chen, Fourati, & Li, 2016) and Kalman filter (Chang, Zha, & Qin, 2017; J. K. Lee & Choi, 2017; Sabatini, 2006; Trawny, 2005; Yun & Bachmann, 2006). Typical Kalman filter is a recursive filter processing linear dynamic system with Gaussian noise. But in lots of practical applications, the system can be non-linear and very complex which is

challenging to apply regular Kalman filter. To adjust to the real-world problems, multiple types of Kalman filters have been developed and were utilized in fusing inertial sensor data especially extended Kalman filter (EKF) (Sabatini, 2006; Trawny, 2005) and unscented Kalman filter (UKF) (de Marina, Espinosa, & Santos, 2012; Shiau, 2013; Zampella, 2012). In the EKF, non-linearization can be applied on both the state model and the measurement model. Nevertheless, if the non-linearity of model is so high, EKF will have particularly poor performance since the error covariance was computed from the non-linear model which can be complicated to determine the Jacobian matrix (Wikipedia, 2018). Taking advantage of unscented transform deterministic sampling technique, UKF was developed to help us reduce the calculation of Jacobians and deal with non-linear systems (Wikipedia, 2018).

The wide-spread use of Kalman filter has proved its accuracy and effectiveness, however, they have some disadvantages. It is complicated to implement the whole algorithm. The foundation to the basic Kalman process – linear regression iterations demand high sampling rate far exceeding the bandwidth of the subject (Madgwick et al., 2011). The real-world problems do not have good linear relations which usually requires large state vectors and a complicate model to linearize them. For example, the description of rotational kinematics in 3-D space typically demands large state vectors and an EKF implementation which leads to higher complexity. As all the Kalman filter built in the sensors are proprietary algorithms, it is necessary to use another simple way to verify the accuracy of the sensors. Here, the sensor fusion method using gradient descent algorithm developed by Madgwick was utilized (Madgwick et al., 2011).

Quaternion is usually defined as

$$q = [q_0, q_1, q_2, q_3] \tag{2-1}$$

q_0 is the scalar part, $q_1 * \vec{\mathrm{i}} + q_2 * \vec{\mathrm{j}} + q_3 * \vec{\mathrm{k}}$ is the vector part. So quaternion can also be represented by

$$q = q_0 + q_1 * \vec{\mathrm{i}} + q_2 * \vec{\mathrm{j}} + q_3 * \vec{\mathrm{k}} \tag{2-2}$$

In the commercial IMU, the quaternion represents the rotation of navigation frame relative to body frame. The derivative of quaternion obeys the vector differential equation denoted by angular velocity $\vec{\omega} = (\omega_x, \omega_y, \omega_z)$ in the body frame relative to navigation frame (Trawny, 2005)

$$\frac{d}{dt}{}^{s}_{n}q = \frac{1}{2}\Omega(\vec{\omega}){}^{s}_{n}q \tag{2-3}$$

where $\Omega(\vec{\omega})$ is a 4 x 4 skew symmetric matrix as

$$\Omega(\vec{\omega}) = \begin{bmatrix} 0 & \omega_z & -\omega_y & \omega_x \\ -\omega_z & 0 & \omega_x & \omega_y \\ \omega_y & -\omega_x & 0 & \omega_z \\ -\omega_x & -\omega_y & -\omega_z & 0 \end{bmatrix} \tag{2-4}$$

$$= \begin{bmatrix} -[\vec{\omega}\times] & \vec{\omega} \\ -\vec{\omega}^T & 0 \end{bmatrix} \tag{2-5}$$

To solve the first order differential equation, $\vec{\omega}$ is assumed to be constant over the integration interval Δt . Then the solution will be the following (Trawny, 2005).

$${}^{s}_{n}q\ (t_{k+1}) = \exp(\frac{1}{2}\Omega(\vec{\omega}_k)\Delta t){}^{s}_{n}q(t_k) \tag{2-6}$$

The initial conditions $q(0)$ are assumed to known or computed from the sensors. The derivative of quaternion can also be represented as

$$\frac{d}{dt}{}^{s}_{n}q = \frac{1}{2}\Xi({}^{s}_{n}q)\vec{\omega} \tag{2-7}$$

where

$$\Xi({}^{s}_{n}q) = \begin{bmatrix} q_4 & -q_3 & q_2 \\ q_3 & q_4 & -q_1 \\ -q_2 & q_1 & q_4 \\ -q_1 & -q_2 & -q_3 \end{bmatrix} \tag{2-8}$$

The main idea of Madgwick's method are derived from the knowledge that there are infinite solutions instead of a unique solution representing the sensor orientation when any measurement are given. Meanwhile, there is only one unique solution of quaternion to represent the orientation. Under this circumstance, a formulation of an optimization problem can be achieved through the combination of three parameters including the orientation of the sensor in the global frame ${}^{s}_{n}q$, a pre-defined reference field in the global frame ${}^{n}d$ and the measured field in the sensor body frame ${}^{s}x$. The objective function can be determined as follows according to the relation that the orientation of sensor is output as that aligns ${}^{n}d$ with ${}^{s}x$.

$$\mathbf{min}\, f({}^{s}_{n}q, {}^{n}d, {}^{s}x) = {}^{s}_{n}q \otimes {}^{n}d \otimes {}^{s}_{n}q - {}^{s}x \tag{2-9}$$

As gradient descent algorithm is one of the simplest optimization algorithms to implement and compute, it was used to solve this objective function. To start with gradient descent algorithm, an initial guess orientation ${}^{s}_{n}q_0$ and the step-size μ are determined to compute the estimate of orientation after n iterations (equation 2-10). An error direction is computed on the solution surface defined by objective function f and Jacobian J.

$${}^{s}_{n}q_{k+1} = {}^{s}_{n}q_k - \mu \frac{\nabla f({}^{s}_{n}q_k, {}^{n}d, {}^{s}x)}{\|\nabla f({}^{s}_{n}q_k, {}^{n}d, {}^{s}x)\|}, \text{ k = 0, 1, 2…n} \tag{2-10}$$

$$\nabla f({}^{s}_{n}q_k, {}^{n}d, {}^{s}x) = J^T({}^{s}_{n}q_k, {}^{n}d) f({}^{s}_{n}q_k, {}^{n}d, {}^{s}x) \tag{2-11}$$

The general form of the algorithm (equations 2-10 and 2-11) will be simplified if the direction of the field can be assumed to have less components in the principal axis in the global frame. Initially, an assumption is made that an accelerometer will only measure gravity and a magnetometer will only measure the earth's magnetic field. Here, ${}^{n}d$ can be represented by two reference field ${}^{n}g$ - field of gravity along vertical z axis and ${}^{n}b$- earth's magnetic field with two

components in horizontal axis and the vertical axis. ${}^{s}x$ can also be substituted by two normalized measurement – accelerometer measurement ${}^{s}a$ and magnetometer measurement ${}^{s}m$.

$$ {}^{s}_{n}q = [q_1, q_2, q_3, q_4] \tag{2-12} $$

$$ {}^{n}g = [0,0,0,1] \tag{2-13} $$

$$ {}^{s}a = [0, a_x, a_y, a_z] \tag{2-14} $$

$$ {}^{n}b = [0, b_x, 0, b_z] \tag{2-15} $$

$$ {}^{s}m = [0, m_x, m_y, m_z] \tag{2-16} $$

Substituting these variables into the objective function and Jacobian, the simplified equations will be as follows.

$$ f_g({}^{s}_{n}q, {}^{s}a) = \begin{bmatrix} 2(q_2q_4 - q_1q_3) - a_x \\ 2(q_1q_2 + q_3q_4) - a_y \\ 2\left(\frac{1}{2} - q_2^2 - q_3^2\right) - a_z \end{bmatrix} \tag{2-17} $$

$$ J_g({}^{s}_{n}q) = \begin{bmatrix} -2q_3 & 2q_4 & -2q_1 & 2q_2 \\ 2q_2 & 2q_1 & 2q_4 & 2q_3 \\ 0 & -4q_4 & -4q_3 & 0 \end{bmatrix} \tag{2-18} $$

$$ f_b({}^{s}_{n}q, {}^{n}b, {}^{s}m) = \begin{bmatrix} 2b_x(0.5 - q_3^2 - q_4^2) + 2b_z(q_2q_4 - q_1q_3) - m_x \\ 2b_x(q_2q_3 - q_1q_4) + 2b_z(q_1q_2 + q_3q_4) - m_y \\ 2b_x(q_1q_3 + q_2q_4) + 2b_z(0.5 - q_2^2 - q_3^2) - m_z \end{bmatrix} \tag{2-19} $$

$$ J_b({}^{s}_{n}q, {}^{n}b) = \begin{bmatrix} -2b_zq_3 & 2b_zq_4 & -4b_xq_3 - 2b_zq_1 & -4b_xq_4 + 2b_zq_2 \\ -2b_xq_4 + 2b_zq_2 & 2b_xq_3 + 2b_zq_1 & 2b_xq_2 + 2b_zq_4 & -2b_xq_1 + 2b_zq_3 \\ 2b_xq_3 & 2b_xq_4 - 4b_zq_2 & 2b_xq_1 - 4b_zq_3 & 2b_xq_2 \end{bmatrix} \tag{2-20} $$

Since the gravity or the earth's magnetic field cannot provide the unique 3D orientation of sensor individually, it is essential to combine two reference fields as described by equation (2-21) and (2-22). The solution surface defined by equation (2-21) has a global minimum point on the

condition that $b_x \neq 0$ which is different from the minimum line found on the solution surface defined by equations (2-17) and (2-19).

$$f_{g,b}({}^{s}_{n}q, {}^{n}b, {}^{s}a, {}^{s}m) = \begin{bmatrix} f_g({}^{s}_{n}q, {}^{s}a) \\ f_b({}^{s}_{n}q, {}^{n}b, {}^{s}m) \end{bmatrix} \tag{2-21}$$

$$J_{g,b}({}^{s}_{n}q, {}^{n}b) = \begin{bmatrix} J_g^T({}^{s}_{n}q) \\ J_b^T({}^{s}_{n}q, {}^{n}b) \end{bmatrix} \tag{2-22}$$

For the multiple iterations of equation (2-10), it will calculate new orientation and sensor measurements each time. The following equations show the computing process of new orientation represented by quaternion.

$${}^{s}_{n}q_{\nabla,t} = {}^{s}_{n}q_{\text{est},t-1} - \mu_t \frac{\nabla f}{\|\nabla f\|} \tag{2-23}$$

$$\nabla f = J_{g,b}^T({}^{s}_{n}q_{\text{est},t-1}, {}^{n}b) f_{g,b}\left({}^{s}_{n}q_{\text{est},t-1}, {}^{n}b, {}^{s}a_t, {}^{s}m_t\right) \tag{2-24}$$

In equations (2-23) to (2-24), ${}^{s}_{n}q_{\text{est},t-1}$ is the previous estimated orientation at time t-1 which is used to compute the estimated orientation ${}^{s}_{n}q_{\nabla,t}$ at time t. The subscript ∇ in quaternion means the quaternion is computed by gradient descent algorithm. ∇f indicates the objective function error determined by accelerometer measurements ${}^{s}a_t$ and magnetometer measurements ${}^{s}m_t$. If only the accelerometer measurements are used, the form of ∇f will be simplified without the magnetic field. The choice of appropriate value of μ_t will ensure the convergence rate of ${}^{s}_{n}q_{\nabla,t}$ not to overshoot due to a large step size. Therefore μ_t is calculated based on the following equation where α is an augmentation of μ_t accounting for the noise in accelerometer and magnetometer, ${}^{s}_{n}\dot{q}_{\omega,t}$ is the angular rate measured by gyroscopes and Δt is the sampling time interval.

$$\mu_t = \alpha \left\| {}^{s}_{n}\dot{q}_{\omega,t} \right\| \Delta t, \alpha > 1 \tag{2-25}$$

In reality, the initial orientation ${}^{s}_{n}q_{\omega,t}$ derived from gyroscope may start from incorrect condition due to the measurement noise. Besides, the instable accelerometer or the magnetometer exposed to magnetic disturbances will cause incorrect estimate for ${}^{s}_{n}q_{\nabla,t}$. A fusion algorithm is adopted to reduce the error and drift in the estimate orientation. The high frequency errors in ${}^{s}_{n}q_{\nabla,t}$ will be filtered out by ${}^{s}_{n}q_{\omega,t}$ and the integral drift from ${}^{s}_{n}q_{\omega,t}$ will be compensated by ${}^{s}_{n}q_{\nabla,t}$. The estimated orientation ${}^{s}_{n}q_{\mathrm{est},t}$ is obtained through fusing the orientation integrated from gyroscope ${}^{s}_{n}q_{\omega,t}$ and the orientation computed from gradient descent algorithm ${}^{s}_{n}q_{\nabla,t}$. Meantime, a weight factor λ_t is implemented in the equation (2-26).

$$ {}^{s}_{n}q_{\mathrm{est},t} = \lambda_t \, {}^{s}_{n}q_{\nabla,t} + (1-\lambda_t) {}^{s}_{n}q_{\omega,t} \tag{2-26} $$

The optimal value of λ_t occurs when the weighted rate of divergence of ${}^{s}_{n}q_{\omega,t}$ induced by integral drift is equal to the weighted rate of convergence of ${}^{s}_{n}q_{\nabla,t}$. Substituting $\frac{\mu_t}{\Delta t}$ and β for the convergence rate of ${}^{s}_{n}q_{\nabla,t}$ and the divergence rate of ${}^{s}_{n}q_{\omega,t}$ respectively, yields the new equation below.

$$ \lambda_t = \frac{\beta}{\frac{\mu_t}{\Delta t}+\beta} \tag{2-27} $$

Since α has no upper bound, Madgwick assumed α to be very large then μ_t is large which means a negligible ${}^{s}_{n}q_{\mathrm{est},t-1}$ in the equation (2-23) leading to the re-written equation (2-28). Another assumption is that β is negligible so that the equation (2-27) can be simplified as equation (2-29) where λ_t can also be assumed as zero.

$$ {}^{s}_{n}q_{\nabla,t} \approx -\mu_t \frac{\nabla f}{\|\nabla f\|} \tag{2-28} $$

$$ \lambda_t \approx \frac{\beta \Delta t}{\mu_t} \tag{2-29} $$

$$ {}^{s}_{n}q_{\omega,t} = {}^{s}_{n}q_{\mathrm{est},t-1} + {}^{s}_{n}\dot{q}_{\omega,t}\Delta t \tag{2-30} $$

Then the estimated orientation ${}^{s}_{n}q_{\mathrm{est},t-1}$ can be represented by equation (3-31) through substituting the equations (2-28), (2-29) and (2-30) into the equation (2-26). The equation (2-30) represents another form of the relationship between the integrated orientation from gyroscope and the estimated orientation ${}^{s}_{n}q_{\mathrm{est},t-1}$ which is derived from equation (2-7). In the substitution of equation (3-31), λ_t is used as two forms: one is zero, the other is the equation (2-29).

$$ {}^{s}_{n}q_{\mathrm{est},t} = \frac{\beta\Delta t}{\mu_t}\left(-\mu_t \frac{\nabla f}{\|\nabla f\|}\right) + (1-0)\,{}^{s}_{n}q_{\mathrm{est},t-1} + {}^{s}_{n}\dot{q}_{\omega,t}\Delta t \tag{2-31} $$

The equation (2-31) can be re-written as equation (2-32) where ${}^{s}_{n}\dot{q}_{est,t}$ is defined as the estimated orientation rate represented by equation (2-33).

$$ {}^{s}_{n}q_{est,t} = {}^{s}_{n}q_{est,t-1} + {}^{s}_{n}\dot{q}_{est,t}\Delta t \tag{2-32} $$

$$ {}^{s}_{n}\dot{q}_{est,t} = {}^{s}_{n}\dot{q}_{\omega,t} - \beta\frac{\nabla f}{\|\nabla f\|} \tag{2-33} $$

It is noticeable that the estimated rate of orientation change ${}^{s}_{n}\dot{q}_{est,t}$ is computed from the angular rate ${}^{s}_{n}\dot{q}_{\omega,t}$ measured by the gyroscope with subtracting the magnitude of gyroscope measurement error β along the direction based on accelerometer and magnetometer measurements. It can be seen that the whole algorithm only contains one adjustable parameter β. In the Madgwick's method, he defined β in equation (2-34) based on ω_β - the estimated angular velocity error of each axis from gyroscope.

$$ \beta = \left\|\frac{1}{2}q \otimes [0, \omega_\beta, \omega_\beta, \omega_\beta]\right\| = \sqrt{\frac{3}{4}}\omega_\beta \tag{2-34} $$

The results of gradient descent algorithm during static and dynamic tests were compared with those computed from the proprietary Kalman filter algorithm in the sensors. The sensor

measurements from ten subjects were used to validate the orientation accuracy of built-in Kalman filter in Opal. A common way to evaluate the orientation sensor performance is using RMSE between sensor angle output and reference system measurements to describe the roll, pitch and heading components (corresponding to the rotations around the sensor frame X, Y, Z respectively) in the decoupled Euler angles during static and dynamic tests (Madgwick et al., 2011).

2.7 Results

It is obvious that the accuracy during static T-pose are much lower compared to the computed root-mean-square-error (RMSE) in the dynamic tests from the results of both algorithms. In the Madgwick's method, the heading angle always showed the largest error (static RMSE: 1.50 ± 0.61 deg; dynamic RMSE: 2.56 ± 1.21 deg) among three components in the sensor angle output in both static and dynamic tests while only the static heading error (1.15 ± 0.59 deg) from Opal were larger than the other two static error (roll: 0.79 ± 0.30 deg, pitch: 1.15 ± 0.59 deg). The error of roll, pitch and heading did not present any significant differences ($p > 0.1$) between Opal Kalman filter and Madgwick's method. All the static and dynamic RMSE values of three Euler angles were within 2 deg for both algorithm implementations which means the level of accuracy is sufficient for human motion applications.

Table 2-2 The RMSE between IMU and VICON from two different sensor fusion techniques during static and dynamic tests

RMSE (deg)	Static Test			Dynamic Test		
	Roll	Pitch	Heading	Roll	Pitch	Heading
Opal Kalman Filter	0.79 ± 0.30	0.76 ± 0.50	1.15 ± 0.59	1.89 ± 1.06	1.98 ± 0.98	1.95 ± 1.99
Madgwick's Method	0.87 ± 0.45	0.69 ± 0.29	1.50 ± 0.61	1.95 ± 0.76	1.68 ± 0.78	2.56 ± 1.21

For the static test results (Table 2-2), it is obvious that VICON is more accurate and less noise compare to IMU in measurement from all aspects. The range error of triad position after system calibration in VICON is 0.2156 ± 0.0198 mm overall. It proves that VICON system can provide accurate position after calibration. Then average acceleration, angular velocity and angle were computed according to the markers' trajectory in three static tests. The offset error of VICON measurements including acceleration and angular velocity are almost zero where the average acceleration offset are all 0.0000 ± 0.0000 m/s^2 along three directions and the average angular velocity about three directions (XYZ) are -0.0001 ± 0.0005 deg/s, -0.0000 ± 0.0005 deg/s, -0.0001 ± 0.0005 deg/s respectively. Meanwhile, the average angle measured by VICON system are also quite small (X: -0.0092 ± 0.0103 deg, Y: -0.0071 ± 0.0098 deg, Z: -0.0008 ± 0.0095 deg) in the static test. Compared to VICON acceleration, IMU has higher bias on the acceleration in the X (0.0704 ± 0.0485 m/s^2) and Y direction (-0.1428 ± 0.0181 m/s^2). The angular velocity about X axis (0.9553 ± 1.0152 deg/s) in IMU are much larger than that about other two axes (Y: -0.0691 ± 0.1832 deg/s, Z: -0.2432 ± 0.1855 deg/s). Static angles measured by IMU about each axis are all lower than 0.25 deg which is accurate enough for clinical study. The large SD of angular velocity about X axis and angle about Z axis from IMU means the outputs are unstable and may have large

error range. Then the error range of each parameter were also checked for potential error. The error range of angular rate and angles are around 1 deg/s and 1 deg separately in 3D space. Overall, the static orientation of Opal IMU is superior to the manufacturer's orientation accuracy estimates of 1.15 deg (roll/pitch) and 1.5 deg (heading). The sensor measurement including acceleration and angular velocity are validated by VICON which are accurate enough for future clinical test.

Table 2-3 The bias and error range of both IMU and VICON in the static test

		X	Y	Z
Average Acceleration (m/s^2)	IMU	0.0704 ± 0.0485	-0.1428 ± 0.0181	0.0000 ± 0.0000
	VICON	0.0000 ± 0.0000	0.0000 ± 0.0000	0.0000 ± 0.0000
Average AngVel (deg/s)	IMU	0.9553 ± 1.0152	-0.0691 ± 0.1832	-0.2432 ± 0.1855
	VICON	-0.0001 ± 0.0005	-0.0000 ± 0.0005	-0.0001 ± 0.0005
Average Angle(deg)	IMU	-0.2303 ± 0.1704	-0.1415 ± 0.2940	-0.2084 ± 0.5183
	VICON	-0.0092 ± 0.0103	-0.0071 ± 0.0098	-0.0008 ± 0.0095
Error Range Acc (m/s^2)	IMU	0.0086 ± 0.0011	-0.0091 ± 0.0004	0.0089 ± 0.0023
	VICON	0.0122 ± 0.0021	0.0169 ± 0.0027	0.0209 ± 0.0058
Error Range AngVel (deg/s)	IMU	1.0998 ± 0.0470	0.9747 ± 0.3528	1.0705 ± 0.0668
	VICON	0.3594 ± 0.0231	0.5342 ± 0.1571	0.2903 ± 0.0505
Error Range Angle (deg)	IMU	0.8648 ± 0.2045	0.5882 ± 0.5185	1.2732 ± 0.7116
	VICON	0.0181 ± 0.0009	0.0263 ± 0.0072	0.0135 ± 0.0014

The constrained linear motion along each direction showed that the correlation coefficient 'r' between IMU acceleration and VICON acceleration were all extremely high ($r > 0.88$) meaning that the acceleration measured by IMU has high agreement with that measured by VICON. The RMSE indicated the precision in each test and the absolute difference between IMU and VICON represented the accuracy here [Taylor,L_2017]. The average RMSE of IMU for Z acceleration (0.769 ± 0.410 m/s^2) was much higher than that of other two axis (X: 0.052 ± 0.012 m/s^2, Y: 0.048 ± 0.018 m/s^2) which means it has lower precision along Z axis. Similarly, the higher mean difference in the Z direction (0.363 ± 0.222 m/s^2) implied lower accuracy compared to the accuracy in the other two directions (X: 0.041 ± 0.009 m/s^2, Y: 0.035 ± 0.006 m/s^2).

All the correlation coefficients of angular velocity and angles are higher than 0.95 which means IMU and VICON almost had greatly similar curve pattern on the angular velocity and angles during each main angular motion. The precision on angular velocity between IMU and VICON was all less than 4.039 deg/s. And the accuracy of angular velocity was within 2.706 ± 3.00 deg/s. The mean accuracy and precision of IMU for angles were within 2.42 ± 2.50 deg and 1.91 ± 1.48 deg., respectively.

Table 2-4 The correlation coefficient (r), RMSE and mean difference (mean_diff) of acceleration between IMU and VICON on the rigid body along each axis in the constrained linear motion test

	X only			Y only			Z only		
	r	RMSE (m/s^2)	Mean_diff (m/s^2)	r	RMSE (m/s^2)	Mean_diff (m/s^2)	r	RMSE (m/s^2)	Mean_diff (m/s^2)
Test 1	0.952**	0.052	0.040	0.941**	0.039	0.033	0.962**	1.170	0.579
Test 2	0.913**	0.065	0.050	0.884**	0.069	0.041	0.999**	0.351	0.136
Test 3	0.971**	0.041	0.033	0.972**	0.038	0.030	0.973**	0.787	0.374

* $p < 0.1$, ** $p < 0.05$

In the walking tests with sensors on the human body, the average precision (RMSE) of angles about three axes were all within 2 deg (X: 1.89 ± 1.06 deg, Y: 1.98 ± 0.98 deg, Z: 1.95 ± 1.99 deg). The measurements of accuracy along each direction were slightly lower than those precision values (X: 1.47 ± 0.77 deg, Y: 1.63 ± 0.81, Z: 1.64 ± 1.70 deg). The consistency of angles between Opal and VICON were comparatively lower than that from tests on the rigid body as the correlation coefficients were within 0.82. The mean precision along Z direction (0.60 ± 0.35 m/s^2) during walking was the best among those in three directions (X: 1.09 ± 0.44 m/s^2, Y: 1.06 ± 1.10 m/s^2). Similarly, the acceleration along Z direction was the most accurate among the measurements from three directions (X: 0.84 ± 0.31 m/s^2, Y: 0.81 ± 0.44m/s^2, Z: 0.48 ± 0.28 m/s^2). IMU had the highest agreement (r= 0.97 ± 0.04) with VICON measurements along Z direction while the agreements along the other two directions were relatively lower (X: 0.60 ± 0.26, Y: 0.66 ± 0.29).

2.8 Conclusion

The static and dynamic orientation accuracy (both RMSE < 2 deg) of built-in Kalman filter in Opal was validated by reference method where the two algorithm implementations had no significant difference of RMSE values comparing to the stereo-photogrammetry measuring system. The heading angle exhibited the largest error among the angle measurements around three axes in both static and dynamic tests from the Opal sensor. Besides, this chapter has demonstrated that the commercial Opal IMU has excellent accuracy and precision of acceleration, angular velocity and angle output. In the controlled rotation tests on the rigid body, the average accuracy and precision of angles were within 2.42 ± 2.50 deg and 1.91 ± 1.48 deg respectively. Meanwhile, the controlled linear tests on the rigid body showed reasonable results of acceleration with mean accuracy 0.77 ± 0.41 m/s^2 and mean precision 0.36 ± 0.21 m/s^2. The static and dynamic RMSE values for sensor

orientations on human body were within 2.0 deg, which is quite close to manufacturer's reported static (roll/pitch: 1.15 deg., heading: 1.5 deg.) and dynamic accuracy (2.80 deg.) estimates. Overall, the accuracy and precision of IMU measurements are sufficient for human motion applications without excluding the soft tissue artifact and unexpected sensor movement on the human body.

Table 2-5 The correlation coefficient (r), RMSE and mean difference (Mean_diff) of angular velocities and angles between IMU and VICON on the rigid body along each axis in the pure rotation test

Pure Rotation		AngVel (deg/s)			Angle (deg)		
		Test1	Test2	Test3	Test1	Test2	Test3
X only	r	0.997**	0.998**	0.997**	0.999**	0.998**	0.999**
	RMSE	2.085	1.395	1.285	3.480	1.179	1.366
	Mean_diff	1.749	1.256	1.167	2.421	0.865	0.981
Y only	r	0.996**	0.997**	0.997**	0.999**	0.999**	0.999**
	RMSE	2.405	4.039	3.424	1.712	2.823	2.857
	Mean_diff	1.82	2.706	2.29	1.248	1.997	2.071
Z only	r	0.998**	0.999**	0.996**	0.997**	0.996**	0.997**
	RMSE	2.154	2.121	2.396	0.539	1.085	0.825
	Mean_diff	2.018	2.027	2.162	0.373	0.924	0.565

* $p < 0.1$, ** $p < 0.05$

Table 2-6 The correlation coefficient (r), RMSE and mean difference (Mean_diff) of acceleration and angles between IMU and VICON on the human body along each axis in the walking

Walking	Angle (deg)			Acceleration (m/s^2)		
	X	Y	Z	X	Y	Z
RMSE	1.89 ± 1.06	1.98 ± 0.98	1.95 ± 1.99	1.09 ± 0.44	1.06 ± 1.10	0.60 ± 0.35
Mean_diff	1.47 ± 0.77	1.63 ± 0.81	1.64 ± 1.70	0.84 ± 0.31	0.81 ± 0.44	0.48 ± 0.28
r	0.69 ± 0.32	0.59 ± 0.33	0.82 ± 0.34	0.60 ± 0.26	0.66 ± 0.29	0.97 ± 0.04

* $p < 0.1$, ** $p < 0.05$

CHAPTER 3: MAGNETIC DISTURBANCES COMPENSATION

3.1 Background

With low-cost and more portable features the IMU including accelerometer, gyroscope and magnetometer are more desired compared to stereo-photogrammetry systems. Since the gyroscopes has low-frequency drift, it is not accurate to output the orientation simply using gyroscope. To overcome the limitation of gyroscope, the other two sensors – accelerometer and magnetometer are needed to compensate the angle measurements from gyroscope. In 3D space, accelerometer can only measure attitude (roll/pitch) relative to the direction of gravity. The magnetometers are applied to measure the heading angle. Unfortunately, they are sensitive to magnetic disturbances causing unexpected error to the heading angle. It is reported that IMU heading error was up to 30° near the floor in the motion lab (de Vries et al., 2009). Compared to the measurements of low limb kinematics outdoors, it yielded a lower repeatability on the transvers plane of each joint measured in the lab (Palermo, Rossi, Marini, Patane, & Cappa, 2014). The type of different mobility aiding device where IMUs were placed on and the IMUs positions would cause orientation errors up to 35.3 deg (Kendell & Lemaire, 2009). In 2007, Roetenberg et al. investigated that the root mean square error between IMU angle output and reference optical system could reach around 50 deg when placing nearby a large metal object while the RMSE would be reduced to 2.6 deg without any magnetic disturbances (Roetenberg, Baten, & Veltink, 2007). The timing related to the magnetic disturbance was revealed that the heading angle would return to the baseline with a 30-second delay after removing the magnetic disturbances (Robert-Lachaine, Mecheri, Larue, & Plamondon, 2017). What's more, the distance from the magnetic source plays an important role in producing the disturbances which stated that the magnetic disturbances can turn into negligible effect at a distance of one meter and exceed the Earth's magnetic field strength within a few centimeters from the source (Bachmann, Yun, & Brumfield, 2007). In a typical motion lab, there

are many kinds of metal equipment which will potentially generate magnetic disturbances to IMU heading angles. Therefore, it is necessary to map the indoor magnetic field before using IMUs which would help identify and possibly avoid the most disturbed area in the testing space. However, It is often unrealistic or quite cumbersome to adapt a wide range of settings like the ceilings, doors and walls for motion analysis in the test space (Robert-Lachaine et al., 2017). In the measurement volume, if the sources of the magnetic disturbance like constructive ferrous material or equipment containing iron are stationary relative to the sensor, the magnetic distortion can be calibrated depending on the theory of soft/hard iron effect; on the contrary, the generated magnetic field in the measurement volume will be affected (de Vries et al., 2009).

Several studies focused on developing novel Kalman-based sensor fusion techniques to manage the problem of magnetic disturbances. The main algorithms dealing with the magnetic disturbances are divided into two types: one is to reject the magnetic disturbances based on the threshold method or various sensor fusion models, the other one is to estimate the orientation without using the data from magnetometer (Ligorio et al., 2016). Nevertheless, all these methods have various limitations. The threshold-based method requires a priori knowledge of Earth's magnetic field used to discard the measurements when the differences are large enough to exceed the chosen threshold. The limitation of this method is that it is difficult to find the optimal threshold and if the threshold values are close to the values of actual magnetic features, the algorithm will exhibit erratic behavior which may lead to large errors (Ligorio et al., 2016). The disadvantage of the model-based method is that the augmented state vector with extra components for estimation of the magnetic disturbances will take more computational cost. The magnetic-free method for orientation estimation can only provide a relative heading angle relative to the initial posture instead of an absolute heading angle relative to Earth Magnetic North. Considering the limitations of all present methods, it is essential to develop a novel algorithm for compensating the sensor heading

errors in the environment surrounded by magnetic disturbances. The goal of this chapter is to build template to quantify the magnetic disturbances and develop a method to compensate heading angle error in the complicated lab or clinical settings. To reach the goal, checking the magnetic field and heading angle consistency at different time and locations will be helpful to find the potential relationship.

3.2 Method

3.2.1 Relationship between magnetic field and heading angle

The heading angle, which is an important variable to evaluate the path of walking in clinical assessment, can be regarded as the angle between the facing direction of a person and the direction along magnetic north. To investigate the algorithm linked with magnetic disturbances affecting heading angle, a comprehensive understanding of conversion from magnetic field measured by magnetometer to heading angle is crucial for later development. As seen from the figure, only magnetic field components in X and Y direction are used to determine the heading angle. To find the Hx and Hy components (Figure. 3-1 (a)) of the earth's magnetic field in the horizontal plane is the key point to accurately compute the heading from a compass or magnetometer (Caruso, 1997). In a real case, the sensors are often tilted in the 3D space which makes it more difficult to calculate the horizontal components of earth's magnetic field. Tilt angles can introduce large errors depending on the value of dip angle. A typical way of compensating the tilt angle is to take advantage of roll and pitch angles measured by accelerometer. Here, roll represents the orientation about X axis, and pitch refers to the orientation about Y axis (Figure. 3-1 (b)).

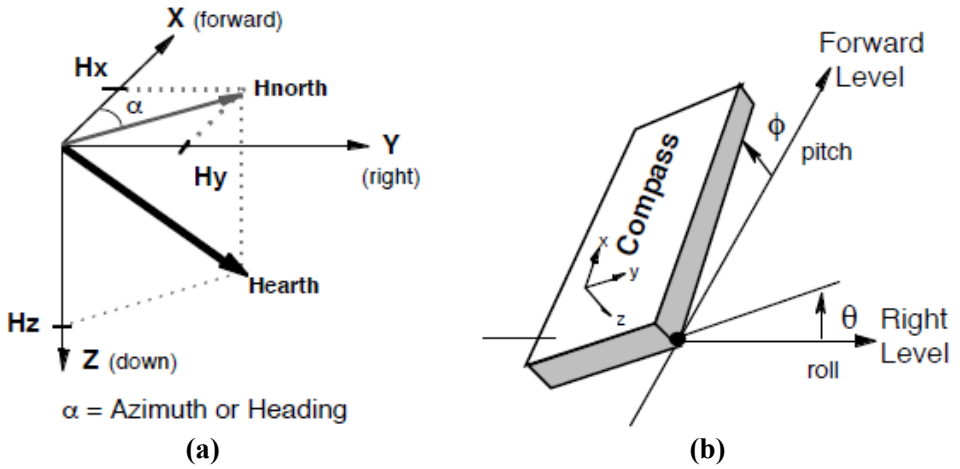

Figure 3.1 (a) Heading angle defined in the flat plane without any tilt angles; (b) A tilted compass referenced to the earth's horizontal plane (Caruso, 1997)

To correct the compass tilt, all three magnetic components (Mx, My, Mz) measured by compass are relied on so that the earth's magnetic field is fully rotated back to the horizontal plane with the assistance of roll and pitch. The equations (3-1) and (3-2) shown below indicate the whole procedure of transforming the magnetic reading from magnetometer back to the horizontal plane where X_H and Y_H represent the forward and side magnetic field of earth in the global frame (Caruso, 1997). Then the heading angle can be determined according to the relationship showing in the Figure 3.1(a).

$$X_H = M_X * \cos(\emptyset) + M_Y * \sin(\theta) * \sin(\emptyset) - \ M_Z * \cos(\theta) * \sin(\emptyset) \tag{3-1}$$

$$Y_H = \ M_Y * \cos(\theta) + M_Z * \sin(\theta) \tag{3-2}$$

$$Heading = \ \tan^{-1}(\frac{Y_H}{X_H}) \tag{3-3}$$

After a comprehensive understanding the relationship between magnetic field and heading angle, the initial step is to confirm if the magnetic distortion does exist in the lab checked by the sensor. Two IMUs were respectively placed on the shoulder and the foot of one subject. Then the subject was asked to randomly walk around the test volume in the lab (Figure. 3.2(a)). The total

magnitude of the magnetic field was computed from the three components measured by the sensor (Figure. 3.2(b)). The overall plot of magnetic field magnitude indicated that there exists large magnetic disturbance (magnitude deviation up to 50 uT) in the lab settings.

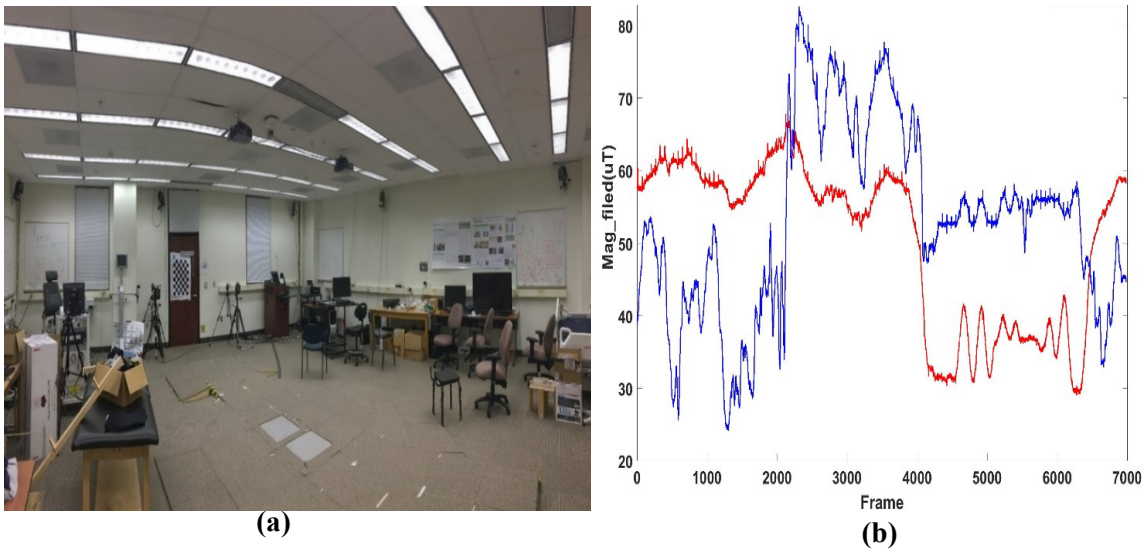

Figure 3.2 (a) The equipment settings in a typical motion lab; (b) The total magnitude of magnetic field measured by two IMUs in the motion lab. Red line represents the IMU on the shoulder, blue line represents the IMU on the foot

3.2.2 Experiment design

The inertial sensors were commonly placed on the body locations like sternum, pelvis and knee etc (Aminian, Najafi, Bula, Leyvraz, & Robert, 2002; Bolink et al., 2016; Cooper et al., 2009; Cuzzolin et al., 2017; Grimpampi et al., 2015; Kavanagh, Morrison, James, & Barrett, 2006; Mazza, Donati, McCamley, Picerno, & Cappozzo, 2012; Zijlstra, 2004). To investigate the magnetic field at these specific locations, a custom-made wood bar was inserted with three wood plates for sensor placement at different height around knee (50 cm), pelvis (100 cm) and sternum (150 cm) (Figure. 3.3(a)). The values of heights were set based on a standard human model (Clauser, 1969). At each height, the plane was evenly divided into eight grids including fifteen dots. The whole volume

could cover the measurement area for our regular experiment. To perform mapping, three sensors were simultaneously attached on the wood bar at each height during static and dynamic tests.

For static test, the wood bar attached with three IMUs was placed on the different locations (Figure. 3.3(b)) for 30 seconds stationary in the lab. All the sensors were fixed horizontally on the wood plate ensuring that its local sensor frame was manually aligned with lab frame. The static tests were performed three times on different days to check if the magnetic disturbances from the surroundings would change with time. In addition, the mid-points located between each grid point along X axis were found and the heading angles at each mid-point were collected for later validation of compensation method. In dynamic test, the wood bar with IMUs was held vertically by hand to slide along the X axis of the lab. The subject who held the bar was instructed to walk three times at two speeds: normal and slow starting at different locations (Figure 3.3(b)). When moving the wood bar to the other location, it is important to assure no relative motion between sensors and wood bar during both tests.

To validate the heading angle, six retro-reflective single markers (10 mm in diameter) were placed on the wood bar where the plane at each height had two markers on the edges separately and three extra triads were fixed on the top of IMUs. A ten-camera stereo-photogrammetry system (VICON, Oxford Metrics Ltd., Oxford, UK) is used to record the motion of the IMU at sampling frequency 120 Hz and define the lab reference frame. As seen from Figure 3-3(b), the lab coordinate system consists of forward X axis, side Y axis, upward Z axis. The origin of the testing volume was set as the right corner point as in the Figure 3-3(b). The sensors used here were Opal IMU (APDM Inc., Portland, OR, USA) that encases 3-axis accelerometer, 3-axis gyroscope and 3-axis magnetometer. The mass is 22 g and the dimensions are 48.4mm x 36.1 mm x 13.4 mm. Data were collected under Robust Synchronized Streaming Mode at sampling frequency 128 Hz. Before the

experiment, all the sensors were calibrated following the magnetometer calibration tutorial provided by the manufacturer.

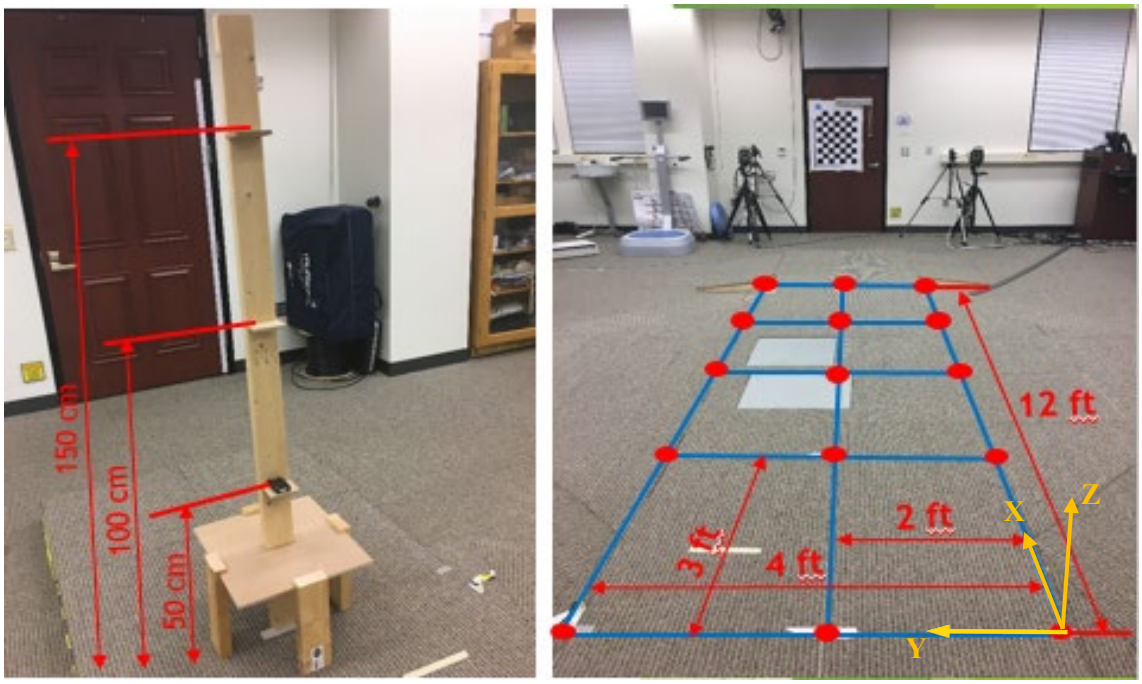

Figure 3.3 Mapping test set-up: left - vertical location; right - horizontal location

3.2.3 Data analysis

A low-pass filter with fourth-order Butterworth filter at cut-off frequency of 6 Hz was used to process markers position data in order to get rid of the high frequency noise. Then the same low-pass filter with a cut-off frequency of 6 Hz was applied to IMU accelerometer data and gyroscope data to remove noise without losing signal integrity. Since IMU data and VICON data were collected at different sampling frequency, a process of synchronization was completed that IMU measurements was resampled to 120 Hz first and then aligned with VICON vertical acceleration through cross correlation function. The cross-correlation will measure similarity between IMU data and VICON data. The maximum cross-correlation value can be used to compute the shifted frames between two measurements. The absolute heading angle of lab frame X is about 43.8° relative to Magnetic North of Earth.

The standard deviation of the heading angles at each location on different days was calculated to check if the consistency of magnetic field was affected by time. The static heading error was quantified as the average difference between mean VICON heading angle and mean IMU heading angle at each location, while the dynamic heading error was defined as the RMSE between VICON heading and IMU heading. One-way analysis of variance (ANOVA) method was applied to test the difference of heading errors among static tests, normal walking and slow walking and the deviation of heading angles on different days. Post-hoc test was then used to check the difference for each two groups.

The spline interpolation method was utilized to compensate the heading angle error in the static test. Then the heading errors computed at the mid-points from the compensation method were compared with the heading errors recorded by IMU and VICON on the same location. Paired t-test was employed to examine the difference between compensation heading errors and real-time heading errors. A custom-developed MATLAB (R2017a, MathWorks Inc., Natick, MA, USA) code was used to perform all the data analysis.

3.3 Results

The standard deviation of heading angle at each location on different days is up to 5.63° which indicated that the heading angle in the testing volume was relatively consistent in the time domain. One-way ANOVA results showed that the standard deviation of heading angles at each height on different days had no significant difference (Knee: 2.54° ± 1.58°, Pelvis: 1.68° ± 0.98°, Sternum: 1.47° ± 1.07°).

As seen from the 3D plot of heading angles in the lab (Figure 3-4), there were certain patterns of heading angles on each path along X axis during static test. Then the 2D plots of heading angles

on each plane exhibited the pattern clearly where the front area close to the origin of testing volume had less magnetic disturbances than the further side. Besides, the closer the sensor is to the ground, the higher heading angle errors are, which means more magnetic disturbances close to the floor.

Table 3-1 The standard deviation of heading angles at different location among different days (unit: °)

(x,y)	Knee	Pelvis	Sternum
(0,0)	3.10	2.28	1.93
(0,2)	1.46	1.53	1.96
(0,4)	2.32	1.21	1.29
(3,0)	4.15	0.44	1.24
(3,2)	3.17	1.23	1.44
(3,4)	5.63	1.48	1.86
(6,0)	4.56	0.46	1.43
(6,2)	0.91	1.13	0.53
(6,4)	0.00	1.63	0.10
(9,0)	3.90	1.32	1.19
(9,2)	3.18	3.03	4.55
(9,4)	1.20	0.87	1.96
(12,0)	1.53	2.89	0.50
(12,2)	0.99	3.97	0.23
(12,4)	2.00	1.76	2.00
Mean	2.54	1.68	1.47
SD	1.58	0.98	1.07

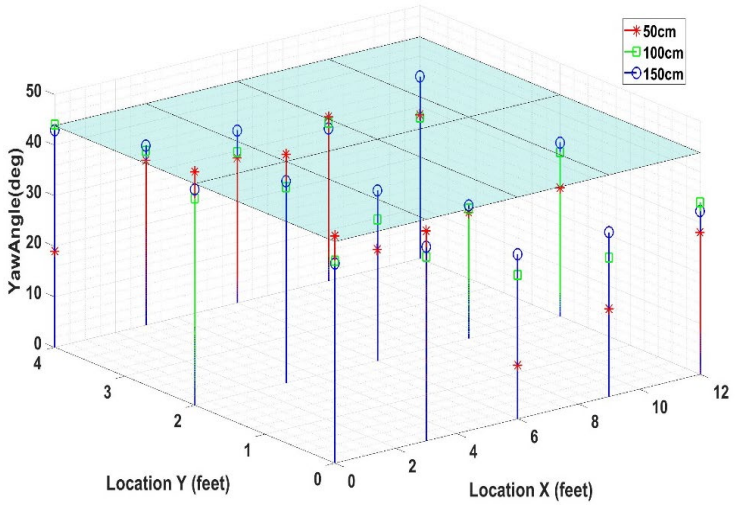

Figure 3.4 3D plot of heading angle at different height during static test where the plane is the standard reference heading angle, the red dot represents the heading angle at knee height, the green dot represents the heading angle at pelvis height and the blue dot represents the heading angle at sternum height.

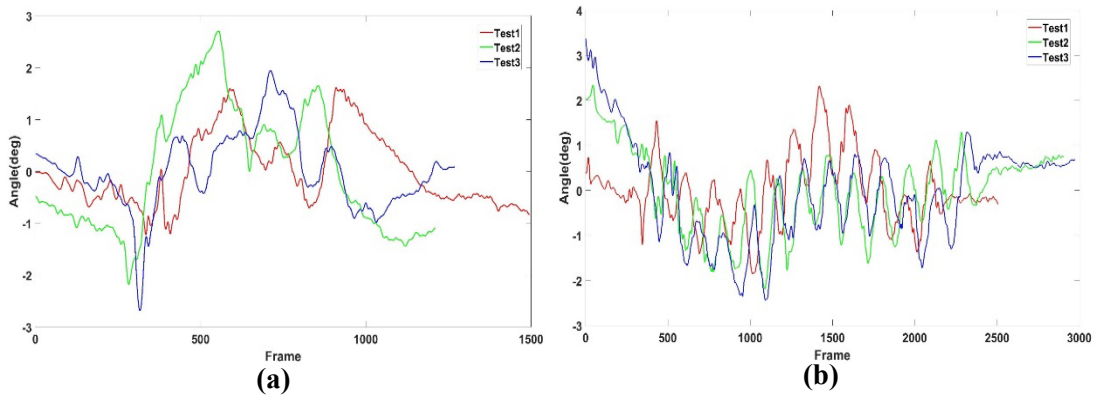

Figure 3.5 (a) The heading angle difference between IMU and VICON frame by frame during three times normal walking; (b) The heading angle difference between IMU and VICON frame by frame during three times slow walking.

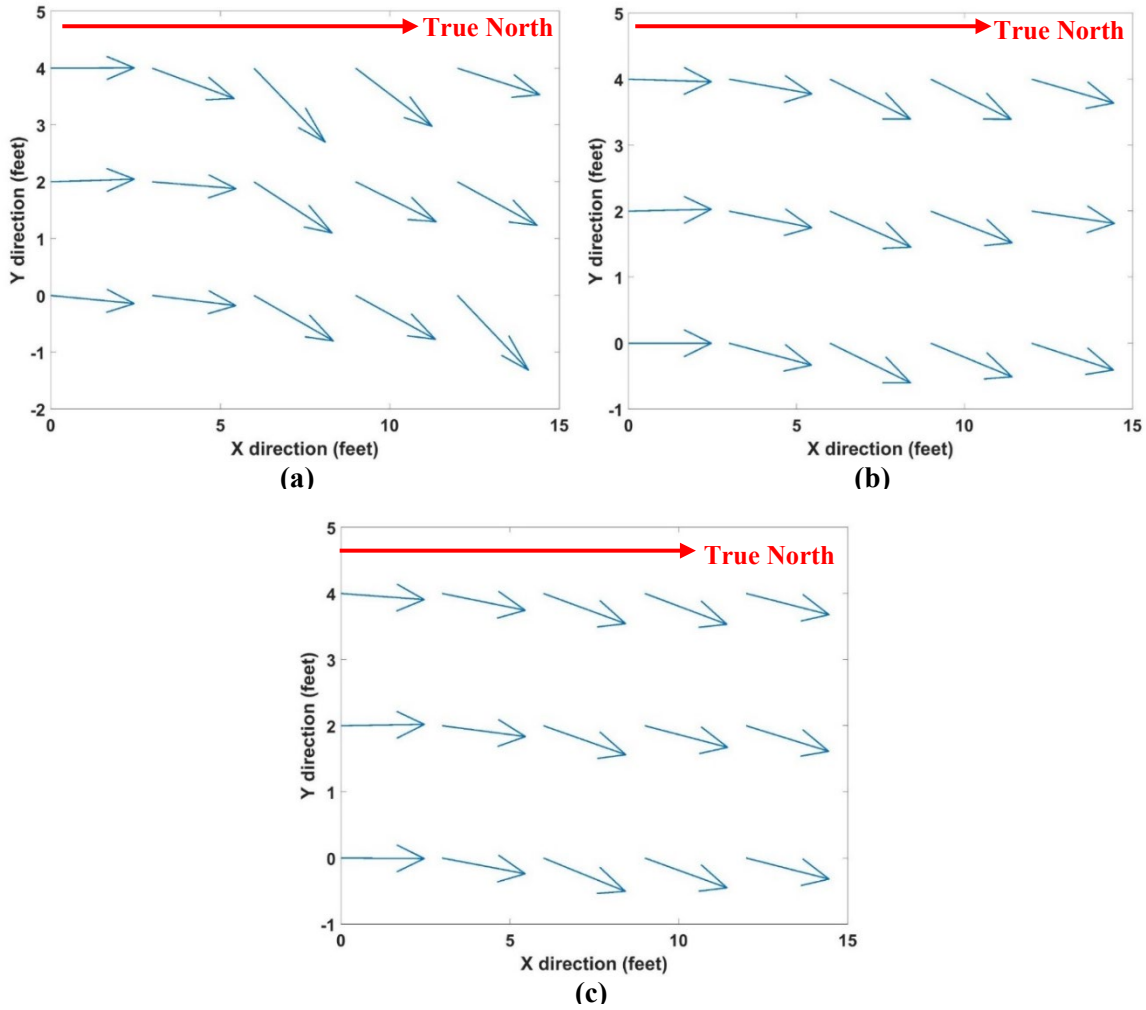

Figure 3.6 2D plots of heading angle direction at each location on three planes (a) plane at knee height (b) plane at pelvis height (c) plane at sternum height

Overall, the mean heading error in the static tests at different height were 9.46° ± 2.17° at knee, 5.24° ± 2.03° at pelvis and 4.20° ± 1.84° at sternum. The heading angle errors at both pelvis ($p < 0.05$) and sternum ($p < 0.01$) height were significantly lower than that at knee height. The heading error during static tests were much greater than those during dynamic tests (within 3°). In the dynamic tests, the mean heading errors at pelvis height were significantly higher ($p < 0.05$) than those at other two heights while the subject walking slowly. On the pelvis plane, the heading errors during normal walking were significantly higher ($p<0.05$) than those from slow walking while the heading errors on the knee and sternum planes had no significant different between normal walking

and slow walking. During slow walking the scale factor at each height had high positive correlation (>0.75) with static heading error in the central line aligned with lab frame X while correlations along other two lines were not strong.

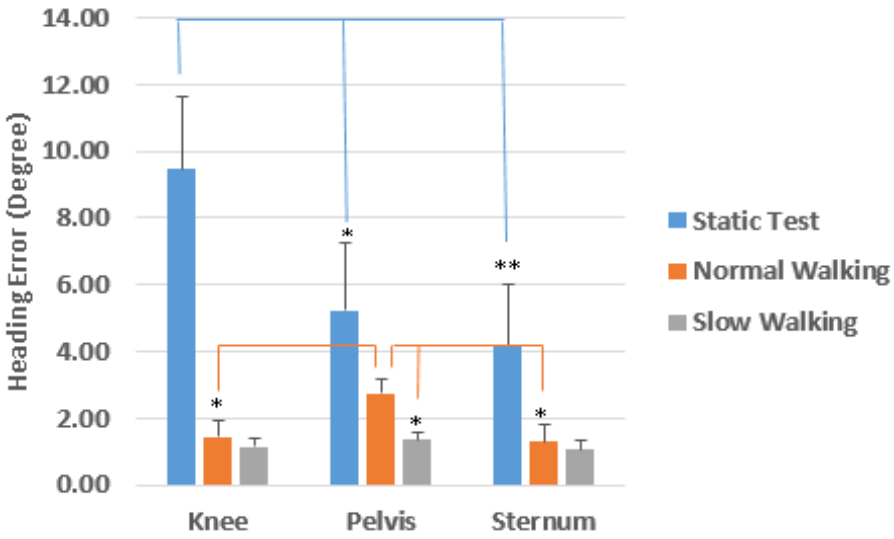

Figure 3.7 The heading errors at different heights during static tests and dynamic tests

The heading errors at validation points were compared between compensation results and measurement results. From Table 3-2, it is obvious that all the compensation results on three planes had significantly improved the accuracy of heading angles (Knee: 3.51 ° ± 1.57°, Pelvis: 2.24 ° ± 1.85°, Sternum: 1.98 ° ± 0.69°) in comparison with the measurement results (Knee: 8.71° ± 4.49°, Pelvis: 4.18° ± 2.13°, Sternum: 4.50° ± 1.37°). In the measurement results from the validation points, the heading errors at knee height showed significantly ($p < 0.01$) larger than the heading errors at pelvis and sternum height. On the contrary, the heading errors from compensation results did not show any significant difference ($p > 0.05$) among the three planes.

Table 3-2 The heading errors from both measurement results and compensation results on three planes

Heading Error (°)	Measurement	Compensation
Knee**	8.71° ± 4.49°	3.51 ° ± 1.57°
Pelvis**	4.18° ± 2.13°	2.24 ° ± 1.85°
Sternum*	4.50° ± 1.37°	1.98 ° ± 1.69°

* represents $p < 0.05$, ** represents $p < 0.01$

3.4 Discussion

This chapter proposes a simple method to compensate the heading angles during static test in the typical motion lab. The variation of the magnetic field (up to 10 uT) was considerable in our lab indicated by both measurement from magnetometer and heading angle errors (up to 30°). The magnetic disturbances were quantified through the errors of heading angles by a straightforward mapping technique. Then the heading errors of the IMUs were tested under dynamic tests evaluated with an external stereo-photogrammetry system.

In a typical motion lab, it is necessary to do magnetic mapping first and then avoid some high magnetic disturbances spot if possible. Similarly, in a clinical setting, there are also a lot of ferrous equipment around which requires a detailed mapping of the magnetic disturbances before any tests. One study claimed that the test should start in an area with minimum magnetic disturbances and continue within 20 – 30 seconds in a heavily distorted area to lower the heading angle errors (de Vries et al., 2009). In our case, the area close to the origin of the measurement volume can be considered as a ‘safe’ location to initiate the test.

When placing IMU on the human body, the larger distance to the ground will increase the accuracy of heading angle during the test since a variety of construction materials in the building contains ferrous metal. In our study it indeed exhibited that the average heading angle errors at knee height (9.46° ± 2.17°) were significantly higher than those at pelvis (5.24° ± 2.03°) and sternum (4.20° ± 1.84°) height. This finding matches the results one of the previous studies where the homogeneity of the magnetic field at 180 cm was about 3° significantly lower than the heading errors 30° at 5cm close to the floor (de Vries et al., 2009). However, in the another study it showed that the distortions of heading angle at the pelvis can reach 9.8° while the maximum errors occurring at lower leg and foot were 4.1° and 4.3° respectively (Robert-Lachaine et al., 2017) which are totally opposite to our findings.

The heading errors during static test were significantly improved by the spline interpolation method based on the certain pattern in our motion lab. The dynamic tests during normal walking and slow walking had very small heading error (within 3°) which was unexpected because the distortions (up to 30°) in the static tests were significantly higher in the same measurement area. The initial hypothesis would be that the heading errors at these pre-defined points during dynamic tests would exhibit similar accuracy as those from the results of static test. However, the results did not support the initial hypothesis. There are two main reasons related to this unexpected condition: one reason is the initial state of heading angles during the dynamic tests which includes little magnetic disturbances. The initial heading angles with minimum distortions did not quickly respond to the heavy magnetic disturbances when passing by each location due to the limited amount of time. Another reason is the convergence rate of built-in Kalman Filter in Opal IMU. The errors of heading estimation from will be affected by different convergence rate in the Kalman filter stated in the previous study (Rhudy, 2015). In our study, it is possible that the convergence rate was so slow that the heading angle estimated by Kalman filter could not reach the optimal state

which is closest to the real heading angle and simply keep the prior measurement from the initial state.

In the several previous studies, they mainly focused on the modification of the Kalman filter algorithm to enhance the accuracy of heading angles under the surroundings of magnetic disturbances (Roetenberg, Luinge, Baten, & Veltink, 2005; Sabatini, 2011b; Yuan, Yu, Zhang, Wang, & Liu, 2015). These methods can increase the accuracy to some degree. For instance, the mean heading estimation errors from a quaternion-based unscented Kalman filter algorithm were around 10° (Yuan et al., 2015). The average static errors and dynamic errors from a complementary Kalman filter in the controlled magnetically disturbed area was reduced from big errors up to 40° to 1.4° and from 11.9° to 2.6° respectively (Roetenberg et al., 2005). These results greatly varied from our measurements due to the different conditions of magnetic field. In addition, the complicated magnetic field in the real environment is extremely different with the controlled conditions performed in the previous studies. It is difficult to justify that the same algorithm with certain assumptions under controlled conditions will also work in the environment of a typical motion lab.

The future study can perform more kinds of dynamic tests which may present totally different results of heading errors, instead of only analyzing the walking test. It may improve the accuracy of compensation results if the process of mapping can be divided into more grids along X direction and more planes along Z direction for additional measurements. More subjects can be recruited to do the dynamic tests since the walking speed will affect the heading angle errors.

In conclusion, it is essential to map the magnetic field in the test area before experiment. When performing a test with inertial sensors, make sure it starts in an undisturbed field. The compensation methods can improve the accuracy of heading angles in the static test. The heading estimation errors from static tests are larger than that of dynamic test. Since the sensor placement

will influence the heading angles, it is recommended that placing the IMUs away from the floor is better option.

CHAPTER 4: OPTIMAL CONFIGURATION

4.1 Background

Parkinson's disease (PD) is a type of chronic disease with progressive neurodegenerative disorder that affects the patient's movement. It often occurs among people around age 60 or older, especially in the men's group (Mayo Clinic, 2018). There are many symptoms related to this disease including tremor in a limb or hand, bradykinesia (slow movement), rigid muscle, impaired posture and balance (Zago et al., 2018). In the United States, every year about 60,000 people are diagnosed with PD and approximately one million people will live with PD by 2020 (Parkinson's Foundation, 2018). A report in 2005 stated that the number of patients with PD over age 50 was around 4.1 - 4.6 million from five Western Europe countries and ten most populated countries in the world (about two thirds of the world population). By 2030, the number of PD population will reach 8.7 - 9.3 million (Dorsey et al., 2007). Since those symptoms of PD may cause potential falls to the patients, it is necessary to monitor their movement and assess the risk of falling for the PD group.

With the development of MEMS technology, many studies investigated the monitoring and diagnosis of PD symptoms and evaluate the patients' mobility in various activities with wearable sensors (Godinho et al., 2016; Kleiner et al., 2018; Mancini, Priest, Nutt, & Horak, 2012; Zago et al., 2018). The wearable sensors are recommended to be used in a lot of clinical applications owing to its portability, low-cost and easy implementation. Three wearable sensors positioned on the low back close to body center mass and both anterior shank succeeded to differentiate the freezing of gait between healthy subjects and PD patients by analyzing the frequency ratio from the anterior-posterior (AP) shank acceleration signals (Mancini et al., 2012). A common mobility test – Timed Up and Go (TUG) was carried out on thirty subjects with PD wearing portable IMUs which showed excellent reliability, accuracy and precision in quantifying the TUG duration (Kleiner et al., 2018).

Recently, a new study looked into the agreement of spatiotemporal gait parameters computed with both optical motion capture system and IMUs simultaneously in the PD patients through comparing eight parameters. It claimed that commercial IMUs needs further improvement on the accuracy of embedded algorithms to be applied for gait analysis in the population of subjects with PD (Zago et al., 2018). However, the inaccuracy arose caused by not only the insufficient accuracy of algorithms but also the selection of output parameters and activities. A proper choice of parameters and activities will definitely affect the accuracy and reliability of IMU output.

A company named Ambulatory Parkinson's Disease Monitoring (APDM) mainly concentrated on the development of gait and balance analysis system for PD patients. The system consists of up to six inertial sensors which are recommended to be attached on various locations, but without any reference related to the selection of output variables and activities. Except this type of specific wearable sensor in clinical application, many other devices with built-in inertial sensors like Apple watch and Fitbit are in the market, primarily for the home use. All these IMU-based systems in the home settings usually adopts single sensor which can only provide limited number of parameters and reduced accuracy and precision (Zago et al., 2018).

So far, only two studies have explored the topic of wearable sensor configurations mainly focusing on the sensor positioning (Bo et al., 2015; Carcreff et al., 2018). One study investigated the optimal IMU placement on the spine using the RMSE between IMU and optoelectronic system to determine when standing, walking and running (Bo et al., 2015); The other study examined the spatiotemporal gait parameters measured by wearable sensors at three different locations on the lower extremity among children with cerebral palsy to evaluate the measurement performances and determine the optimal configuration of sensor positioning (Carcreff et al., 2018). However, it is still unknown to the researchers how to choose the optimal sensor configurations on the whole body for the diversified subjects. Nowadays, with the wide use of Artificial Intelligence algorithms, some

studies have applied classification algorithms on the investigation of the best sensor location on the human body in the fall detection (Bourke, O'Brien, & Lyons, 2007; Bourke et al., 2010; Kangas, Konttila, Lindgren, Winblad, & Jamsa, 2008; Ozdemir, 2016; Ozdemir & Barshan, 2014; Yuwono, Moulton, Su, Celler, & Nguyen, 2012). However, there were conflicts among some reports where two reports stated that waist is the best location to detect falling due to its closest distance to center of gravity (Bourke et al., 2010; Ozdemir, 2016) while other reports claimed that chest or head place is better (Bourke et al., 2007; Kangas et al., 2008). Several studies concluded that arms or legs are not suitable segments of the human body to carry wearable sensors to predict fall risk since these segments are associated with higher accelerations (Bianchi, Redmond, Narayanan, Cerutti, & Lovell, 2010; Kangas, Konttila, Winblad, & Jamsa, 2007). Most of the studies associated with classification algorithms commonly extracted some features like maximum value, minimum value and mean value directly from the raw signal (Bourke et al., 2010; Ozdemir, 2016; Yuwono et al., 2012). From the point biomechanics of views, it will be more meaningful to compute more features like step time, body tilted angle, and step length which can directly exhibit the motion of human body.

The goal of this chapter is to explore the various combinations of sensor configurations and figure out the optimal configuration for the monitoring and diagnosis of PD. A machine learning algorithm will be utilized in this chapter to assist to evaluate the performance in the final decision-making.

4.2 Method

4.2.1 Experimental protocol

Eighteen subjects including six female and twelve male were recruited. All the subjects were divided into three groups: six young healthy subjects (height: 1.59 ± 0.71 m, weight: 67.41 ± 14.94 kg), six old healthy subject (height: 1.56 ± 0.65 m, weight: 87.41 ± 14.23 kg) and six old patients with PD (height: 1.58 ± 0.94 m, weight: 83.41 ± 8.41 kg). All the healthy subjects had no history of functional disorders or postural control problems. The patients with PD should have the ability to perform daily activities like walking and standing without any external assistance from other people. Patients walking with a cane or other type of assistive device could still be considered as potential subjects. An IRB protocol was approved related to this study and all the subjects were required to sign an informed consent form before testing.

According to some previous studies, the inertial sensors were commonly placed on the body locations like sternum, low back, wrist and foot etc (Aminian et al., 2002; Bolink et al., 2016; Cooper et al., 2009; Cuzzolin et al., 2017; Grimpampi et al., 2015; Kavanagh et al., 2006; Mazza et al., 2012; Zijlstra, 2004). In this study, six IMUs were placed on the both wrist, both ankle, low back and sternum respectively for all the subjects. On the top of each IMU, a single triad were attached for the validation of sensor motion. In addition, fourteen retro-reflective single markers (diameter 10 mm) were placed on the human body including four on the pelvis, four on both sides of the knee, eight on both sides of the foot (Figure 4.1(b)). All the subjects were asked to perform a static T-pose test before the experiment. Then the subjects were instructed to perform one of commonly used tests – walking. Each gait section was performed four times by the subjects with normal walking speed. For the safety issues, a metal frame with safety harness attached on was built to protect the subjects from falling down.

Here, the sensor configuration is defined as the sensor placement on the human body. As there are six sensors placed on the body, the combinations of sensor configurations can reach up to 63 possible options in theory. In this study, only 15 combinations out of 63 options were analyzed according to the feature of test and the symmetry of the segment. The following table (Table 4-1) showed the different combinations of sensor configurations for different tests. The wrist and shank locations both include two sensors on the left and right side of body.

Table 4-1 Combinations of sensor locations on the human body during walking. A – chest, B – low back, C – wrist, D – shank. COMB is combinations.

#	Chest	Low Back	Wrist	Shank	COMB
1	1	0	0	0	A
2	0	1	0	0	B
3	0	0	1	0	C
4	0	0	0	1	D
5	1	1	0	0	AB
6	1	0	1	0	AC
7	1	0	0	1	AD
8	0	1	1	0	BC
9	0	1	0	1	BD
10	0	0	1	1	CD
11	1	1	1	0	ABC
12	1	0	1	1	ACD
13	1	1	0	1	ABD
14	0	1	1	1	BCD
15	1	1	1	1	ABCD

0 represents not used, 1 represents used.

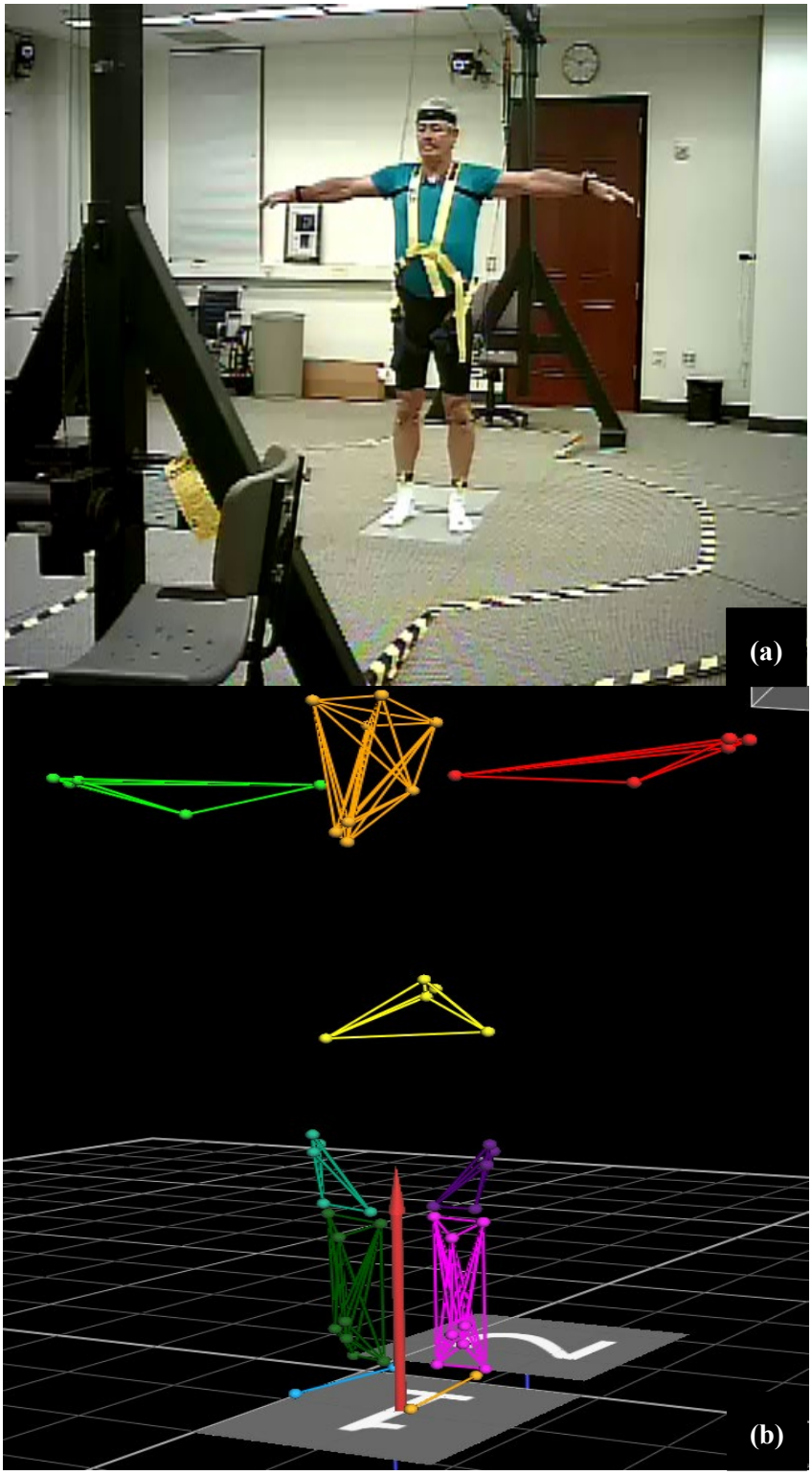

Figure 4.1 (a) Static T-pose before the test (b) whole marker set on the human body

A ten-camera stereo-photogrammetry system (VICON, Oxford Metrics Ltd., Oxford, UK) is used at sampling frequency 120 Hz to monitor the trajectory of markers as a golden standard reference system. The sensors used here were Opal IMU (APDM Inc., Portland, OR, USA) that encases 3-axis accelerometer, 3-axis gyroscope and 3-axis magnetometer. The mass is 22 g and the dimensions are 48.4mm x 36.1 mm x 13.4 mm. Data were collected under Robust Synchronized Streaming Mode at sampling frequency 128 Hz.

4.2.2 Data analysis

Data analysis was split into three steps: preprocessing, feature extraction and classification. To compare the sensors from different body segments and different subjects, it is necessary to preprocess the accelerations, angular velocities and angles. A low-pass filter with fourth-order Butterworth filter at cut-off frequency of 6 Hz was applied on the raw acceleration and angular velocity. Then all the sensor signals were transformed to the global coordinate frame with X – forward direction, Y – pointing to the left, Z – pointing up initially. After transformation into the global frame, the gravitational accelerations were subtracted from the vertical accelerations. A custom-developed MATLAB (R2017a, MathWorks Inc., Natick, MA, USA) code was used to perform all the data analysis.

For walking test, the maximum, minimum, mean and variance values of accelerations, angular velocities and angles from all sensors were extracted. The step time was computed by locating the key frame at peak on the shank angular velocity in the sagittal plane. The asymmetrical ratio of step time, arm swing angular velocity and leg swing angular velocity were calculated from the following equation (Yogev, Plotnik, Peretz, Giladi, & Hausdorff, 2007).

$$\text{Gait asymmetry} = 100 * |\text{right parameter}/\text{left parameter}| \quad (4\text{-}1)$$

With fifteen combinations of sensor configurations, three types of machine learning techniques were used to differentiate the three groups. Accuracy, sensitivity and specificity were utilized to evaluate the performances of machine techniques. To determine the performance parameters, four possibilities need to be considered in a confusion matrix. The first one is the true positive (TP) where the classification technique shows the occurrence of PD matching the actual result that the subject is real PD. Second case is the true negative (TN) when a subject is healthy and the algorithm does not show the disease. TP and TN are true decision given by the classification. Then the false decisions given by algorithms are false positive (FP) and false negative (FN). FP, known as 'Type I error', refers to the case that the subject does not have PD but the algorithm predicts that the subject has PD while FN , 'known as Type II error', refers to the reversed condition of FP which is the most dangerous and unwanted case.

The performance parameters can be formulated using the definitions above. Accuracy measures how well the algorithm predicts the TP and TN overall.

$$Accuracy = \frac{TP+TN}{TP+TN+FP+FN} * 100 \tag{4-2}$$

Sensitivity measures the proportion of positives that when the subject is PD, the classifier also grouped this subject into PD group. This is an important parameter to evaluate the performance of a model for diagnosis of PD which indicates how well the classifier predicts the PD.

$$Sensitivity = \frac{TP}{TP+FN} * 100 \tag{4-3}$$

Specificity measures the proportion of negatives that are correctly identified as healthy group. It refers to the ability of correctly identify healthy people and indicates how well the algorithm predicts the healthy group.

$$Specificity = \frac{TN}{TN+FP} * 100 \tag{4-4}$$

A good classifier is expected to provide high accuracy, sensitivity and specificity. For the specific case related to diagnosis of PD, the success of the algorithm relies on the frequency of FN decisions mostly. A missed diagnosis of PD, FN, is a serious mistake for the model. Meanwhile, a false diagnosis of healthy people, FP, should be avoided in the algorithm since it may cause many troubles to the users. For an ideal classifier in this study, FP and FN are expected to be 0. There is always a tradeoff between sensitivity and specificity for any classification algorithm.

Due to the limited number of subjects, the training data set from the formulation of the decision rule was used to estimate the classifier error which is known as re-substitution. In general, the re-substitution may introduce bias and provide optimistic results. The reason using re-substitution in this study is that the main goal is to use the classification performance from the various sensor configurations to determine the optimal sensor configuration.

Three different machine learning techniques including k-Nearest Neighbor (KNN) Classifier, Naïve Bayesian (NB) Classifier, and Random Forest (RF) were used to classify the subjects into three groups based on various sensor configurations. Each algorithm will be briefly introduced in the following part.

As one of the simplest methods in machine learning, KNN algorithm is basically used to classify the most similar data points in the training dataset (Duda, 2001). The nearest neighbor k ($k > 0$) which is a user-defined value is the most important parameter to make decision of the classes through the majority voting. A proper k value should be defined specifically for the specific problem since the KNN algorithm is sensitive to the composition of local dataset. The bias will be increased with the increasing of k value but the sensitivity will be reduced. A smaller k value provides less stable results with the increasing of the variance. Therefore, the choice of k value is quite essential in the KNN method. Here, k was set as 3 after trying the k values in the range from 1 to 10.

NB algorithm is a probabilistic classifier using maximum likelihood in the Bayesian settings (Duda, 2001). The likelihood in NB is defined by the normal density discriminant function. The class decision is made by using the maximum likelihood indexes for the given test vector. There are two main parameters for each class in the function: one is the mean of the training vectors, the other is the covariance matrix of training vectors.

RF algorithm is a popular ensemble method to build predictive models for both classification and regression problems. It uses multiple learning models to gain better results where the algorithm consists of an entire forest of random uncorrelated decision trees. A random subset of features are considered in each decision tree in the forest which will increase the diversity in the forest leading to more robust predictions overall. In this study, the max depth for all trees was set as 3 in the forest and the number of trees was set as 20.

4.3 Results & Discussion

The following three tables (Table 4-2, 4-3, 4-4) presented the classification performance of three machine learning algorithms based on sensor combinations. Overall, KNN shows the lowest average sensitivity (57.78%), specificity (74.29%) and accuracy (68.52%) compared to the results of NB (average sensitivity – 96.67%, specificity – 89.44% and accuracy – 80.37%) and RF (average sensitivity – 86.67%, specificity – 94.24% and accuracy – 87.41%). The best classification results (sensitivity – 100%, specificity – 100% and accuracy – 100%) among all the sensor combinations under three algorithms is achieved with the sensor combination of chest, wrist and shank using NB algorithm. As mentioned above, higher sensitivity is better choice for this study. Among three algorithms, NB algorithm will be recommended to the similar study in the future.

In the results of KNN algorithm, the best accuracy (77.78%) is achieved by using single sensor on the chest meanwhile the specificity (91.67%) from single chest sensor is highest among

all the combinations. When the features of all six sensors are used for classification, the KNN algorithm gives 72.22% accuracy. The single sensor on the low back and two sensors on both wrist provides the highest sensitivity (66.67%) as that from the seven different sensor combinations, which are chest_lowback, chest_shank, wrist_shank, chest_wrist_shank, chest_lowback_shank, lowback_wrist_shank and all sensor included. The phenomenon proves that the increasing of number of sensors does not guarantee the best classification results. The lowest sensitivity (16.67%) is given by sensor combination of low back and wrist.

Table 4-2 The classification performances of KNN based on fifteen combinations of sensor configurations. A – Chest, B – Low Back, C – Wrist, D – Shank, COM - Combination.

COMB	Sensitivity	Specificity	Accuracy
A	50.00	91.67	77.78
B	66.67	72.73	66.67
C	50.00	75.00	66.67
D	66.67	66.67	66.67
AB	66.67	66.67	66.67
AC	50.00	83.33	72.22
AD	66.67	75.00	72.22
BC	16.67	75.00	55.56
BD	50.00	66.67	61.11
CD	66.67	75.00	72.22
ABC	50.00	83.33	72.22
ACD	66.67	75.00	72.22
ABD	66.67	66.67	66.67
BCD	66.67	66.67	66.67
ABCD	66.67	75.00	72.22

The performances of NB algorithm are promising and satisfactory. When six sensors are used in the calculation, NB produces good results with 100% sensitivity, 100% specificity and 94.44% accuracy, however, the best sensor combination is chest_wrist_shank giving all 100% for three evaluation parameters. When each single sensor combination is examined, it is clear that chest sensor, labeled as A, gives alone the best sensitivity (100%), specificity (91.67%) and accuracy (94.44%) with NB algorithm. Twelve out of fifteen total sensor combinations reaches the highest sensitivity (100%) with NB algorithm which will be quite useful for diagnosis of PD in the future. The lowest sensitivity (83.33%) from NB algorithm is even higher than that (66.67%) from KNN algorithm. Two individual sensor combination wrist and shank produces the lowest sensitivity respectively.

Table 4-3 The performances of NB based on fifteen combinations of sensor configurations. A – Chest, B – Low Back, C – Wrist, D – Shank.

COMB	Sensitivity	Specificity	Accuracy
A	100.00	91.67	94.44
B	100.00	33.33	38.89
C	83.33	83.33	83.33
D	83.33	77.78	66.67
AB	100.00	100.00	66.67
AC	100.00	91.67	94.44
AD	100.00	91.67	94.44
BC	100.00	88.89	77.78
BD	100.00	100.00	61.11
CD	83.33	83.33	83.33
ABC	100.00	100.00	88.89
ACD	100.00	100.00	100.00
ABD	100.00	100.00	72.22
BCD	100.00	100.00	88.89
ABCD	100.00	100.00	94.44

RF produces 100% sensitivity, 100% specificity and 94.44% accuracy with all sensors used in the classification process which is the same as NB. The best accuracy (94.44%) is achieved by four different sensor combinations which all includes chest sensor and shank sensor. The chest sensor gives the best classification results (100% sensitivity, 90.91% specificity and 88.89% accuracy) among four individual sensor location while low back sensor alone produces the worst classification performances (50% sensitivity, 83.33% specificity and 72.22% accuracy).

Table 4-4 The performances of RF based on fifteen combinations of sensor configurations. A – Chest, B – Low Back, C – Wrist, D – Shank. (unit : %)

COMB	Sensitivity	Specificity	Accuracy
A	100.00	90.91	88.89
B	50.00	83.33	72.22
C	83.33	100.00	83.33
D	100.00	83.33	88.89
AB	100.00	90.91	88.89
AC	100.00	100.00	94.44
AD	100.00	90.91	88.89
BC	66.67	100.00	88.89
BD	50.00	83.33	72.22
CD	83.33	100.00	83.33
ABC	100.00	100.00	94.44
ACD	100.00	100.00	94.44
ABD	100.00	90.91	88.89
BCD	66.67	100.00	88.89
ABCD	100.00	100.00	94.44

The best result among double, triple and quadruple sensor configurations are 66.67% sensitivity, 75.00% specificity and 72.22% accuracy for KNN where four different combinations all including shank sensor achieve this result. Then all 100% for sensitivity, specificity and accuracy is achieved by 'ACD' combination under NB. The sensor combinations containing chest and shank gives the best results (100% sensitivity, 100% specificity and 94.44% accuracy) using RF algorithm.

Overall, the best performance (100% sensitivity, 91.67% specificity and 94.44% accuracy) of single sensor combination is produced by the chest sensor using NB algorithm. Table 4-5 summarizes the average sensitivity, specificity and accuracy of each single sensor combination for three machine learning techniques. It is clearly seen that chest sensor has the best average classification performance (83.33% sensitivity, 91.41% specificity and 87.04% accuracy) while the low back sensor produces the worst classification results (72.22% sensitivity, 63.13% specificity and 59.26% accuracy). The reason for this performance is because low back does not produce much movement relative to the whole trunk which is not affected much by interpersonal differences in the body movement of the subjects while the position of chest sensor varies depending on the subjects' gender, posture and body shape which causes an increase of interpersonal differences and directly increases the classification performances of differentiating the PD patients.

Table 4-5 The average sensitivity, specificity and accuracy of three machine learning techniques at each individual sensor location (unit: %)

Location	Sensitivity	Specificity	Accuracy
Chest	83.33	91.41	87.04
Low back	72.22	63.13	59.26
Wrist	72.22	86.11	77.78
Shank	83.33	75.93	74.07

The overall results proved that it is possible to gain very high accuracy with single sensor configuration. The classification performance and the number and location of sensor units does not show any strong relationship since the accuracy is not improved apparently with the increasing of the number of sensors.

Compared to the previous study, one report about the sensitivity analysis of sensor location claimed that the best results were obtained with the knee range of motion using four IMUs placed on the shank and thigh bilaterally and range of motion (ROM) appeared as a key contributor for the classification accuracy. Besides, this study also declared that the increasing number of sensors does not determine a direct increase in classification accuracy which matches the findings in our study (Caramia, Bernabucci, D'Anna, De Marchis, & Schmid, 2017).

There are several limitations of this study. The features were all extracted from the processed data, thus inherently compressing the information coming from raw data. Excluding the feature set from raw data may hide possible effects at different level since the whole feature set was quite ample. The classification performance in this study was related to re-substitution error which is overestimated compared to the true error, even though it could be still used to differentiate the PD patients. To solve this issue, more subjects need to be recruited and more activities need to be performed for future study so that the data set can be divided as training data and test data for cross validation. In the future, it is necessary to include the different extracted parameters combining with different sensor configurations to comprehensively investigate the diagnosis of PD patients. It is still one of the great research challenges to find the optimal balance among sensor locations, number of sensors, test activities and specific computed parameters in wearable sensors for clinical applications. Last but not least, the PD patients can be assigned to different stages which shows different motion feature. It is essential to classify the PD patients into different stages for more accurate diagnosis.

4.4 Conclusion

This study has shown that the ability of wearable sensors based on gait features can assist to discriminate the patients with PD from the young healthy and old healthy individuals depending on the number and location of sensors placed on the human body. The classification accuracies are not directly affected by the increasing number of sensors. The optimal sensor configuration was achieved by the sensors placed on chest, wrist and shank together. A single sensor configuration can also produce very high accuracy like the chest sensor. The choice of machine learning techniques did have influence on the final classification performances. Here, the Naïve Bayesian algorithm was recommended to differentiate the PD patients.

It is possible for the clinicians to choose the features and the sensor placement to define the gait-related manifestations, not specifically for PD patients, when referring to the research of this study. The use of wearable sensors for motion capture has represented a big step towards the digital monitoring process in a variety of clinical applications. Integrated with advanced machine learning techniques, the wearable sensors may move the clinical application closer to the decentralization of diagnostic decisions as well.

CHAPTER 5: FALL RISK ASSESSMENT

5.1 Feasibility of single IMU during walking

5.1.1 Introduction

Gait is one of most common and highly demanding movement in daily life. Patients with some postural control diseases and traumatic injuries, like Parkinson's disease and trauma brain injury, may have gait disorders. Features of various pathological gait can be used for diagnosis of injury/diseases, assessing treatment outcomes, and designing rehabilitation protocols. Gait analysis is also used for assessing balance system and risk levels for fall (Bergamini et al., 2014). Thus, gait analysis plays an important role in clinical study and biomechanics research. Optoelectronic motion capture systems using stereo-photogrammetry are widely used in gait analysis (Bergamini et al., 2014; Bolink et al., 2016; Buckley, Galna, Rochester, & Mazza, 2017; Cuzzolin et al., 2017; Esser et al., 2009; Gonzalez, Lopez, Rodriguez-Uria, Alvarez, & Alvarez, 2010). Unfortunately, these systems are expensive and have limited use in non-lab setting environment. A gait laboratory often needs a large space, a skilled biomechanist, and not accessible to many clinicians.

With rapid development of MEMS, sensors are becoming cheaper, lighter and smaller. These advantages bring inertial sensors – one of the most important members of MEMS to human motion analysis field. Inertial sensors including accelerometer, gyroscope and magnetometer are usually combined as IMU. Compared to complex and expensive camera-based motion capture system, IMUs are low-cost and often can be used in an office or a hallway. IMUs have obvious advantages for monitoring outdoor activity and tracking a body movement for a much longer period (hours, even days). Many researchers placed single IMU on the lower trunk where is close to center of mass of whole body to quantify the gait movements (Bergamini et al., 2014; Bolink et al., 2016; Buckley et al., 2017; Cuzzolin et al., 2017; Esser et al., 2009; Gonzalez et al., 2010; Grimpampi,

Bonnet, Taviani, & Mazza, 2013; Henriksen, Lund, Moe-Nilssen, Bliddal, & Danneskiod-Samsoe, 2004; Johnston, Patterson, O'Mahony, & Caulfield, 2016; Kavanagh, Barrett, & Morrison, 2004; Kavanagh et al., 2006; Kose, Cereatti, & Della Croce, 2012; Luinge & Veltink, 2005a; Trojaniello, Ravaschio, Hausdorff, & Cereatti, 2015b; Zijlstra, 2004) and distinguish healthy people and patients with movement dysfunction (Cuzzolin et al., 2017; Grimpampi et al., 2013; Parisi et al., 2016; Trojaniello et al., 2015b; Yang, Zhang, Novak, Brouwer, & Li, 2013). Meanwhile, other IMU placement locations were also popular in the gait analysis especially on the lower limb which can easily provide step length, cadence, speed etc (Bolink et al., 2016; P. Esser, Dawes, Collett, Feltham, & Howells, 2012; Grimpampi et al., 2013; Johnston et al., 2016; Kavanagh et al., 2006; Kose et al., 2012; McCamley, Donati, Grimpampi, & Mazza, 2012; Moon et al., 2017; Sabatini & Mannini, 2016; Zijlstra & Hof, 2003). However, only a few studies carried out gait analysis with IMU put on the upper body like sternum (Keijsers et al., 2006; Luinge & Veltink, 2005a; Tanaka et al., 2004). In the study of Tanaka, S. et al., they placed three IMUs on the shank, thigh and sternum during gait, nevertheless walking speed was computed only from lower limb IMUs. Gyroscopes and accelerometers on the pelvis and trunk were used by Luinge et al. to measure orientation of human body compared with optokinetic system which is only limited to orientation measurement (Luinge & Veltink, 2005a). Keijsers et al. put multiple accelerometers on the body including one sensor on the sternum to distinguish on and off states for patients with Parkinson's disease rated by a trained observer (Keijsers et al., 2006).

The aim of this paper is to investigate the feasibility of single IMU on the sternum during gait validated with reference system for assessing movement of patients with dysfunctional motion and healthy people. It is also necessary to understand what kind of meaningful information can be provided by single IMU on the sternum in walking.

Table 5-1 Description of some representative studies with IMU in gait analysis

Study	Subjects	Sensor Type	Sensor Location	Sampling rate (Hz)	Gold Standard	Estimated Parameters
Zijlstra,W (Zijlstra & Hof, 2003)	25 healthy	tri-axial Accelerometer	dorsal pelvis	100	Force Plates	step time; step length
McCamley,J (McCamley, Donati, Grimpampi, & Mazza, 2012)	18 healthy	IMU	lower lumbar spine	100	Instrumented mat	step time
Esser,P (Esser, Dawes, Collett, Feltham, & Howells, 2012)	10 PD	IMU	L4	100	SP system	step time; stride length; vertical velocity and displacement
Grimpampi, E (Grimpampi et al., 2013)	13 Stroke, 11 PD	IMU	lower lumbar spine	100	SP system	pelvic angles

5.1.2 Method

Ten subjects (eight males and two females) were recruited in this study, including five control subjects and five patients (after orthopedic surgery on the ankle) with a mean age of 32.3 ± 8.9 years, height of 67.9 ± 3.7 inch, and body mass of 170.4 ± 31 lbs. The protocol was approved by IRB and all subjects gave their informed consent.

After attaching an IMU (Opal, APDM Inc., Portland, OR, USA) above their sternum through elastic straps, subjects were required to perform static T-pose trial with their upper-body straight upward for three seconds. Participants were then instructed to complete three-meter walking wearing single IMU on the sternum at self-selected speed as they normally do. Two level

walking trials were recorded. Between walking trials, subjects were asked to pause for three seconds.

The IMU that encases 3-axis accelerometer, 3-axis gyroscope and 3-axis magnetometer weighted 22 g and is 48.4mm x 36.1 mm x 13.4 mm in dimension. Data were collected at sampling frequency 128 Hz. A ten-camera stereo-photogrammetry tracking system (VICON, Oxford Metrics Ltd., Oxford, UK) was used as reference system to validate the accuracy of IMU sensor for monitoring gait. Five single spherical retro-reflective markers and one triad attached on IMU on the upper trunk (Figure 5.1). VICON motion data were collected at 120 Hz.

Figure 5.1 IMU placed on the sternum with triad attached to it and other markers on the upper body

Markers position data was low-pass filtered with fourth-order Butterworth filter at cut-off frequency of 6 Hz. Then the same low-pass filtering with an optimal cut-off frequency for each individual determined by a residual analysis was applied to IMU accelerometer data and gyroscope data to remove noise without losing signal integrity. Since IMU data and VICON data were collected at different sampling frequency, synchronization processing was performed by resampling IMU data at 120 Hz and aligning with VICON data through cross correlation. To compare IMU data with VICON data, all the data should be transformed into the same reference frame. For VICON data, a least root mean square method (Spoor & Veldpaus, 1980) was carried out to determine trunk orientation from markers' positions. For IMU data, the IMU local frame was

set to align with that of VICON. With magnetometer in the Opal IMU, it provides quaternion data 'q' of orientation in the earth magnetic coordinate system (EMS) with built-in Kalman filter reducing orientation error. To reset the initial orientation to zero,

$$q_{ini} = q_j * q_0' \tag{5-1}$$

q_0' is the conjugate of initial quaternion at T-pose and q_j is the quaternion of each frame. q_{ini} is the initialized quaternion through quaternion product. To convert quaternion to Tait-Bryan angles (second type of Euler angles) directly, a certain rotation sequence 'Z-Y-X' was set for the conversion. All the gyroscope and accelerometer data were converted to EMS through the quaternion first.

$$Acc_E = q_j * Acc_j * q_j' \tag{5-2}$$

$$AngVel_E = q_j * AngVel_j * q_j' \tag{5-3}$$

q_j is the same as that in the previous equation and q_j' is the conjugate of q_j from the sensor fusion. Acc_j and $AngVel_j$ are the local acceleration and angular velocity from IMU. Acc_E and $AngVel_E$ are the acceleration and angular velocity in the EMS. Then the transformation matrix was applied to transform all data to the same global lab coordinate system (GLS) of VICON. The transformation matrix 'R' was created through the fixed rotation angle 'α' (about 43 deg in our lab) between earth magnetic coordinate and VICON lab coordinate. Acc_G and $AngVel_G$ are the acceleration and angular velocity in the GLS in the following equations.

$$R = \begin{bmatrix} \cos\alpha & -\sin\alpha & 0 \\ \sin\alpha & \cos\alpha & 0 \\ 0 & 0 & 1 \end{bmatrix} \tag{5-4}$$

$$Acc_G = R * Acc_E \tag{5-5}$$

$$AngVel_G = R * AngVel_E \quad (5\text{-}6)$$

To evaluate the feasibility of single IMU on the chest, VICON measurement of the sensor from three markers attached to it was set as reference data. Two methods were used to calculate angles from IMU consisting of direct integration of $AngVel_G$ (IMU_INT) and direct quaternion q_j to Euler angles (IMU_Quat). Acceleration (Acc_G) were integrated twice to obtain position for IMU measurements in three directions. Since the integration error increases proportionally with time (Maklouf, 2014), a simple 'detrend' function (MATLAB, The Mathworks Inc., Natick, MA, USA) was added to remove the linear drift after integration.

From the acceleration data, peak-to-peak vertical acceleration (P2P_VA) and step time were calculated. P2P_VA was the average of the ranges from positive peaks to successive negative peaks. Step time of IMU was defined as the time between two consecutive peaks of vertical acceleration (McCamley et al., 2012). The precision and accuracy of IMU on the basis of VICON measurements was represented with RMSE and average of absolute value of difference (Mean_diff) (Taylor, Miller, & Kaufman, 2017). Also, the consistency between IMU and VICON was expressed by the correlation coefficient (***r***). Bland-Altman plots were applied to show the agreement of step time and P2P_VA between two systems. Paired t-test was used to assess the difference of two systems. All the data analysis was performed using our custom MATLAB codes (The Mathworks Inc., Natick, MA, USA).

5.1.3 Results

Overall, IMU_Quat angles have high accuracy (all within 1.64° ± 1.70°) and precision (all within 1.98° ± 0.98°) about three directions. However, yaw angles from IMU_INT have larger error and difference (11.89° ± 3.59° and 10.07° ± 3.01°) with reference data while roll and pitch angles

show better precision and accuracy (both within 2.54° ± 1.69°). Average correlation coefficient indicates that angles from IMU_Quat display higher consistency than that of IMU_INT in all the directions. Among three directions of IMU_Quat angle, yaw angle exhibits highest consistency with reference data (Table 5-2).

In the Anterior-posterior (AP) and Medial-Lateral (ML) direction, the IMU acceleration, velocities and displacement had greater error and differences than those in the vertical (V) direction. Besides, the average correlation coefficient of the IMU acceleration, velocities and displacement in vertical direction is highest (Acc: r = 0.96 ± 0.04, Vel: r = 0.98 ± 0.03, Disp: r = 0.90 ± 0.06) among three observed directions.

The paired t-test revealed that step times from both VICON and IMU were consistent in patients group (VICON step time: 0.53 ± 0.08s, IMU step time: 0.54 ± 0.08s) and control group (VICON step time: 0.51 ± 0.06s, IMU step time: 0.51 ± 0.05s) and had no significant differences ($p > 0.05$). Meanwhile, no significant difference ($p > 0.05$) was found for P2P_VA between VICON and IMU in patients (VICON P2P_VA: 7.99 ± 3.05 m/s^2, IMU P2P_VA: 7.71 ± 2.85 m/s^2) and control (VICON P2P_VA: 8.97 ± 2.87 m/s^2, IMU P2P_VA: 8.64 ± 2.49 m/s^2). The Bland-Altman plot (Fig. 2) indicated that VICON and IMU had good agreement on the measurement of step time and P2P_VA and most subjects are within two standard deviation (Mean ± 2*SD).

Table 5-2 Means and SD of RMSE, mean difference and correlation coefficient between different groups of angles for all subjects

Angle		*RMSE* (°)	*Mean_diff* (°)	***r***
IMU_INT	Roll	2.19 ± 1.37	1.74 ± 1.10	0.64 ± 0.33
vs	Pitch	2.54 ± 1.69	2.10 ± 1.39	0.38 ± 0.50
VICON	Yaw	11.89 ± 3.59	10.07 ± 3.01	0.21 ± 0.44
IMU_Quat	Roll	1.89 ± 1.06	1.47 ± 0.77	0.69 ± 0.32
vs	Pitch	1.98 ± 0.98	1.63 ± 0.81	0.59 ± 0.33
VICON	Yaw	1.95 ± 1.99	1.64 ± 1.70	0.82 ± 0.34

Table 5-3 Means and standard deviations (SD) of RMSE, mean difference and correlation coefficient between different groups of accelerations, velocities and displacement for all subjects

	Acceleration (m/s^2)			Velocity (m/s)			Displacement (m)		
Direction	*RMSE*	*Mean_diff*	*r*	*RMSE*	*Mean_diff*	*r*	*RMSE*	*Mean_diff*	*r*
AP	1.10 ± 0.43	0.85 ± 0.31	0.60 ± 0.26	0.18 ± 0.09	0.15 ± 0.09	0.39 ± 0.23	1.74 ± 0.29	1.54 ± 0.25	0.32 ± 0.74
ML	1.07 ± 0.59	0.83 ± 0.42	0.66 ± 0.29	0.12 ± 0.07	0.10 ± 0.06	0.66 ± 0.30	0.03 ± 0.02	0.03 ± 0.02	0.43 ± 0.38
V	0.70 ± 0.34	0.55 ± 0.28	0.96 ± 0.04	0.04 ± 0.02	0.03 ± 0.02	0.98 ± 0.03	0.009 ± 0.006	0.007 ± 0.005	0.90 ± 0.06

* AP is anterior-posterior direction, ML is medial-lateral direction, V is vertical direction.

5.1.4 Discussion

Gait analysis with low-cost and easy-to-go IMUs has become one of the commonly used tests in biomechanics and clinical research. Previously, gait speed, cadence, step length and step time were usually generated in these studies according to the IMU placement location mainly including lower limb and pelvis (Esser et al., 2012; McCamley et al., 2012; Moon et al., 2017; Sabatini & Mannini, 2016; Zijlstra & Hof, 2003). No one has finished the feasibility study of gait analysis with single IMU on the upper trunk like sternum. The upper trunk normally has greater swing than the lower trunk during activities of daily living, which will be easier for clinicians to observe. This paper presented a feasibility study of single IMU placed on the sternum in level walking validated with a reference stereo-photogrammetry system and provided meaningful information of gait for bio-mechanists and clinicians.

Table 5-4 Mean and SD of range of angles and accelerations of patients and control in three directions.

Axis		Angle (°)		Acceleration (m/s^2)	
		Patient	Control	Patient	Control
X	VICON	11.00 ± 4.09	7.06 ± 1.71	4.41 ± 1.31	5.11 ± 1.82
	IMU	12.63 ± 6.43	9.50 ± 3.39	5.41 ± 1.97	6.15 ± 2.95
Y	VICON	11.26 ± 6.32	8.99 ± 3.54	4.39 ± 0.86	5.03 ± 1.43
	IMU	11.57 ± 6.35	7.99 ± 1.96	7.46 ± 4.23	7.06 ± 3.11
Z	VICON	16.55 ± 7.98	9.99 ± 2.85	10.33 ± 3.00	10.19 ± 3.07
	IMU	17.48 ± 5.66	10.32 ± 3.45	11.12 ± 3.43	10.54 ± 3.11

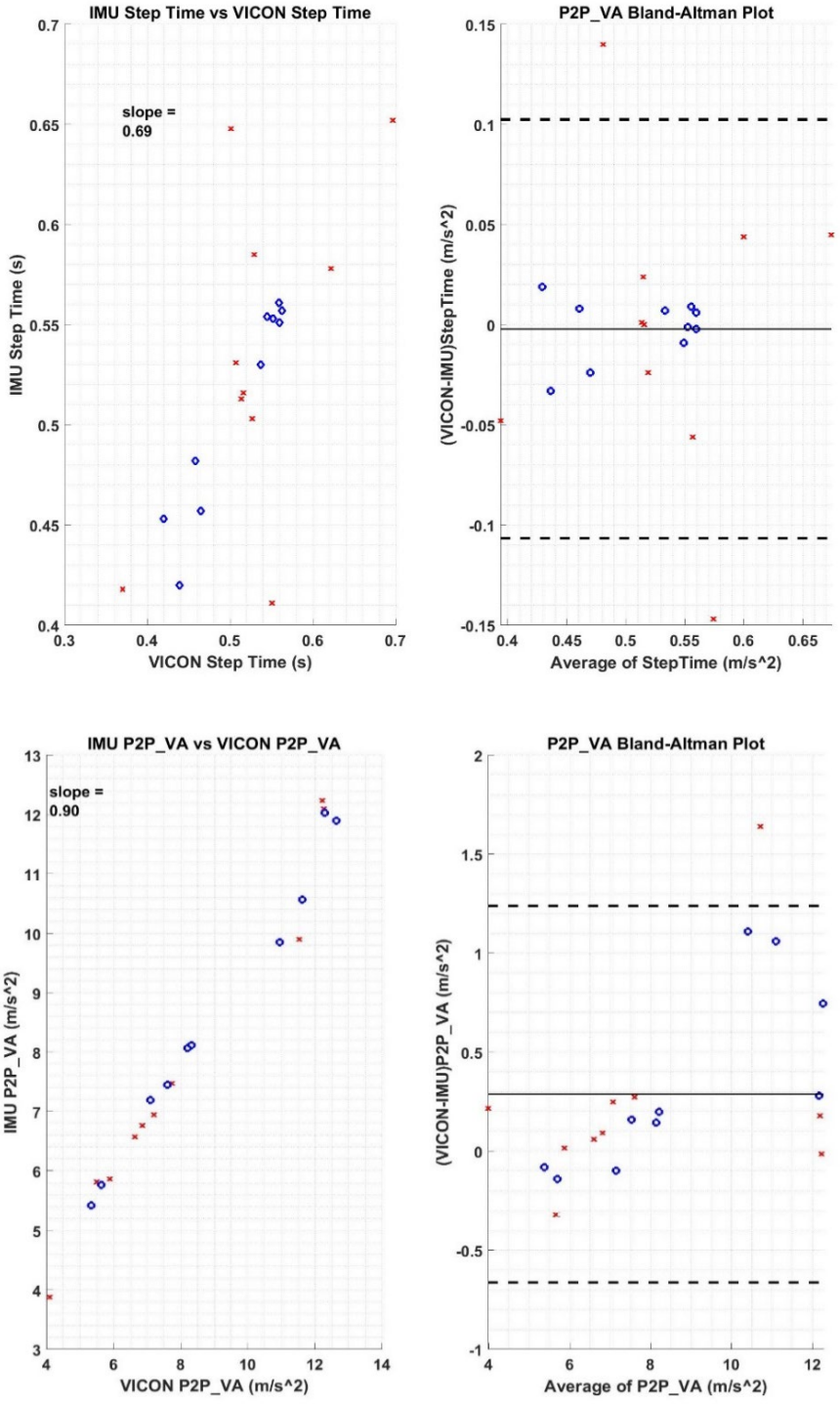

Figure 5.2 (a) Top plot is the Bland-Altman plot of step time between VICON and IMU; (b) Bottom plot is the Bland-Altman plot of P2P_VA between VICON and IMU. In both plots, blue circle represent control group, and red cross represent patient group. The dashed lines on the right plots represent the lower and upper limits of agreement (Mean ± 2*SD) respectively

In clinical applications, the body segment orientation is one of the important variables (Muro-de-la-Herran, Garcia-Zapirain, & Mendez-Zorrilla, 2014). Acceleration was also used in the gait analysis especially vertical acceleration of trunk (Buckley et al., 2017; Gonzalez et al., 2010; Henriksen et al., 2004; Kavanagh et al., 2006; Steins, Sheret, Dawes, Esser, & Collett, 2014; Zijlstra, 2004). Therefore, accelerations and orientation angles of the trunk in 3D space were selected as key parameters for this IMU feasibility study. There were two methods of orientation calculation presented in this study. The results evidently showed us that angles determined from magnetometer were more accurate than that from gyroscope and magnetometer fusion, especially in the yaw angle, due to a larger drift of angular velocity. Here the angles calculated from the magnetometer was suggested in the future angle calculation during gait analysis. The results of angles from magnetometer are in accordance to outputs from other studies. Previously, a study completed by Bolink et al. focused on validating pelvic angle with single IMU compared with an optoelectronic motion capture system which found average RMSE of range of motion (ROM) for frontal plane and sagittal plane were 2.68°~4.44° and 2.70°~8.89°. However, the Pearson's correlation coefficients were between 0.85 and 0.94 for two angles which are higher than results in this paper (Bolink et al., 2016). It may occur due to Bolink et al. only analyzed healthy subjects' data while five traumatic patients after surgery were included in this study. Patients may have much greater range of motion which is related to unstable gait. Favre et al. demonstrated a functional calibration procedure for 3D knee angles using IMU with magnetic markers' validation and obtained all mean errors of knee angles below 2° in three planes (Favre, Aissaoui, Jolles, de Guise, & Aminian, 2009). In the report by Bauer et al., they assessed the lumbar spine ROM with IMU and presented that RMES of sagittal plane ROM and frontal plane ROM were 4.1°~4.4° and 1.8°~1.9° correspondingly (Bauer et al., 2015).

Considering the linear motion parameters, vertical position, velocity and acceleration are most accurate and reliable based on precision, accuracy and correlation coefficients among three directions during gait. This is consistent with the results of average relative difference between IMU and optoelectronic system from all healthy subjects including acceleration -0.190 ± 0.088 m/s^2, velocity -0.012 ± 0.025 m/s and position -0.047 ± 0.060 m by Esser et al. (Esser et al., 2009). To estimate the displacement in the walking direction during gait, some researchers placed IMUs on the foot to estimate the step length with a popular algorithm – 'Zero Velocity Update' (Alvarez, Gonzalez, Alvarez, Lopez, & Rodriguez-Uria, 2007; Bae & Tomizuka, 2013; Sabatini & Mannini, 2016) while other researchers compute step length from IMUs attached to the pelvis with an inverted pendulum model (Esser et al., 2012; Steins et al., 2014; Trojaniello et al., 2015b; Zijlstra & Hof, 2003). In this study it is not recommended to use similar algorithm to compute step length due to the reason that sternum is far away from the center of mass in the body and trunk motion pattern is totally different from foot motion pattern. Here it can be seen that large bias was shown in the walking direction which will lead to underestimated walking speed and step length for IMU. The side position of body from IMU had good accuracy and precision but low correlation with VICON caused by tiny motion in the sideway. Meanwhile, yaw angles displayed the largest range of motion and vertical acceleration plays a major role of total acceleration after removing the gravity. It indicated that single IMU on the sternum during gait will exhibit higher accuracy and precision along the dominant axis (vertical direction) while the measurement in the non-dominant axis will enlarge the error. This kind of consequences might be caused by the ability of the sensors and algorithm to detect and use gravity to produce accurate orientation estimates (Godwin, Agnew, & Stevenson, 2009).

As stated above, it will be greatly beneficial in clinic if IMU can assist clinicians to distinguish patients and healthy people. The upper trunk orientation in three directions

demonstrated that patients possess larger range of angles which is consistent with our common knowledge. Step time and P2P_VA are two main parameters to tell patient from healthy controls. Post-hoc analysis did not show significant difference between patients and control which was affected by the patient group containing three patients almost recovered and two patients severely injured with bracelet on. The different severity of patients also leads to the large SD of data for the patient group. In addition, three subjects in control group are above ten years older than the other two subjects resulting in apparently longer step time and lower peak vertical acceleration. Even though this study did not succeed to distinguish patients and control through IMU measurements, it is still reliable and accurate to use single IMU on the sternum to evaluate abnormal gait according to the high agreement between IMU and VICON in the patients group.

A few limitations should be recognized in this study. To begin with, the level of injury should be assessed to eliminate the potential source of error when recruiting patients. The size of sample needs to be increased to improve the range of different motion pattern. Another limitation of this study was the orientation angles calculated from IMU. No matter the angle from integration of angular velocity after combining the quaternion or the angle from quaternion only was used, they both take advantage of quaternion data from IMU which were combined signals from accelerometer, gyroscope and magnetometer fusion. This fusion algorithm performing data filtering to remove drift and noise was from the development of the manufacturer which is unknown to the users (Buckley et al., 2017). Overall, our study results demonstrate that it is feasible to apply single IMU on the sternum in the gait analysis to measure orientation angles of trunk and vertical acceleration, velocity and position. Step time from vertical acceleration and peak-to-trough vertical acceleration of IMU also works for assessing gait among patients and healthy controls.

5.2 Feasibility of single IMU during FTSTS

5.2.1 Introduction

As one of a highly demanding movement of daily living, sit-to-stand (STS) is often compromised for elderly with functional limitations which is frequently used as assessment method to evaluate stability of dysfunctional patients. Quantification of STS for people with pathological movements will be helpful to appraise the degree of impairment. Meanwhile, the understanding of the chair-rise strategies may lead to improved treatment recommendations. The strategies of STS mainly include momentum transfer (MT), exaggerated trunk flexion (ETF) and dominant vertical rise (DVR) (Scarborough, McGibbon, & Krebs, 2007). Previous studies usually measure STS movement and determine the type of chair-rise strategy with common motion lab equipment like force plate and stereo-photogrammetry system (Galli, Cimolin, Crivellini, & Campanini, 2008). It will have a promising usage if a cheaper and more portable IMU can provide similar function as well. The goal of this study was to explore the feasibility of quantifying STS transition with IMU and investigate whether single IMU on the chest can identify chair-rise strategy.

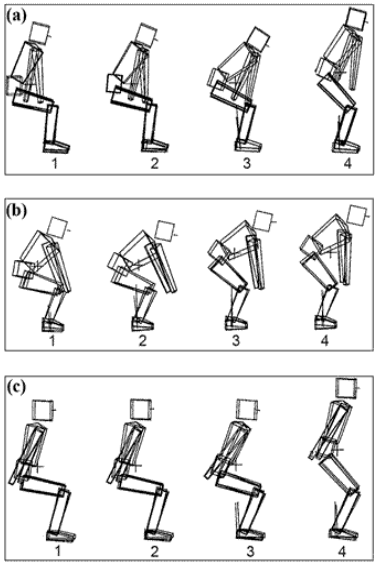

Figure 5.3 Three main chair-rise strategies: (a) momentum transfer (b) exaggerated trunk flexion (c) dominant vertical rise (Scarborough et al., 2007)

5.2.2 Method

Nine healthy subjects (six males and three female, age 27.5 ± 8.2 years, height 1.70 ± 0.35 meters) were instructed to complete Five-Time-Sit-to-Stand (FTSTS) wearing single Opal IMU (APDM, sampling frequency 128 Hz) on the sternum with each leg on a separate force plate. Between each sit-to-stand and stand-to-sit, subjects were asked to pause for three seconds. Two force plates (AMTI) were applied to measure ground reaction force (GRF) at sampling frequency 1500 Hz. A ten-camera optical tracking system (VICON, sampling frequency 128 Hz) was used as reference system to validate the accuracy of IMU sensor for monitoring FTSTS. Correlation coefficients were computed among various parameters from IMU and other equipment.

Three types of chair-rise strategies were defined based on the observation of VICON model during STS. The investigator classified all the subjects' chair-rise strategies based on the definitions of each strategy (Figure 5.4). Then K-means cluster was used to identify different strategies according to the following sensor measures: peak trunk flexion angle, peak trunk flexion angular velocity, peak trunk forward acceleration, peak trunk vertical acceleration. All these variables are average values from FTSTS for each subject.

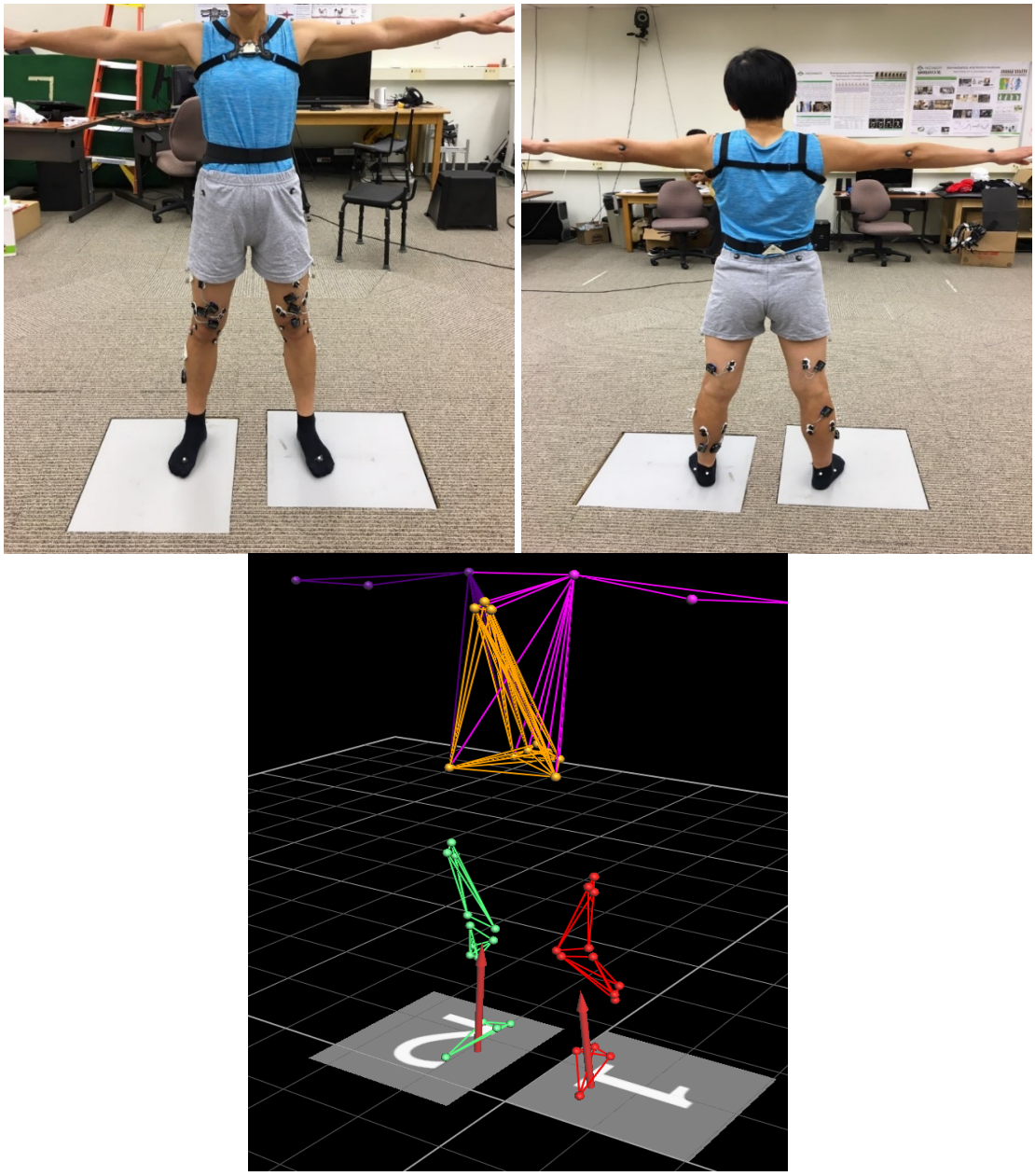

Figure 5.4: Experiment set-up: Top left - front view; Top right back view; Bottom - VICON model with all the markers

5.2.3 Results

The time of peak vertical acceleration occurred almost at the same time as peak total vertical ground reaction force according to high correlation coefficient (0.993±0.014). However,

the correlation (0.735±0.202) between peak acceleration and peak total force is comparatively lower. Significantly high consistency was found between IMU and VICON for vertical acceleration (0.990±0.004) and pitch angular velocity (0.982±0.011).

From observation results by VICON model, most of subjects (number = 5) used MT strategy. Both ETF strategy and DVR strategy were performed by two subjects respectively. The Spearman's rank-order correlation coefficient between observation strategy groupings and K-means clustering groupings was notable ($r = 0.50$, $p = 0.18$). Both peak trunk flexion angle and peak trunk flexion angular velocity differed significantly across the three chair-rise strategy groups ($p < 0.05$) while no significant difference was noted in peak trunk forward acceleration and peak trunk vertical acceleration across the strategy groupings ($p > 0.1$).

Table 5-5 Correlation coefficient between IMU peak acceleration vs Force Plate and IMU vs VICON

Subject ID	peak acceleration keyframe vs Total peak Force keyframe	peak acceleration vs peak Total Force	IMU VertAcc vs VICON VertAcc	IMU Pitch AngVel vs VICON Pitch AngVel
1	0.9906	0.8215	0.9798	0.9883
2	0.9999	0.3910	0.9875	0.9910
3	0.9999	0.3975	0.9909	0.9722
4	0.9996	0.8820	0.9961	0.9923
5	0.9996	0.8367	0.9967	0.9923
6	0.9942	0.8275	0.9892	0.9884
7	0.9950	0.8111	0.9929	0.9824
8	1	0.9002	0.9907	0.9742
9	0.9999	0.9082	0.9916	0.9791
Mean	0.9934	0.7353	0.9902	0.9818
SD	0.0135	0.2022	0.0049	0.0110

Table 5-6 Cluster analysis results of chair-rise strategy groupings based on four variables from IMU

Variable	MT	EFT	DVR
Peak Trunk Flexion Angle (deg) *	37.98 ± 0.01	58.30 ± 10.10	24.94 ± 4.00
Peak Trunk Flexion AngVel (deg/s) *	84.79 ± 5.83	104.35 ± 5.92	72.38 ± 11.58
Peak Trunk Forward Acc (m/s^2)	0.67 ± 0.17	0.62 ± 0.20	0.83 ± 0.34
Peak Trunk Vertical Acc (m/s^2)	4.63 ± 1.48	4.02 ± 0.53	4.05 ± 0.94

* One-Way ANOVA across strategies, $p < 0.05$

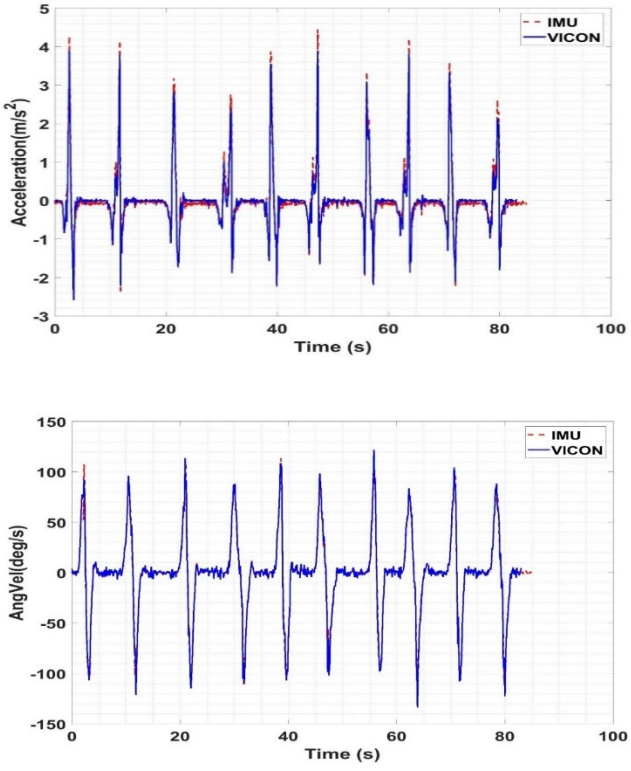

Figure 5.5 The plots of typical example for IMU and VICON during FTSTS. Top graph is the vertical acceleration; Bottom graph is the pitch angular velocity

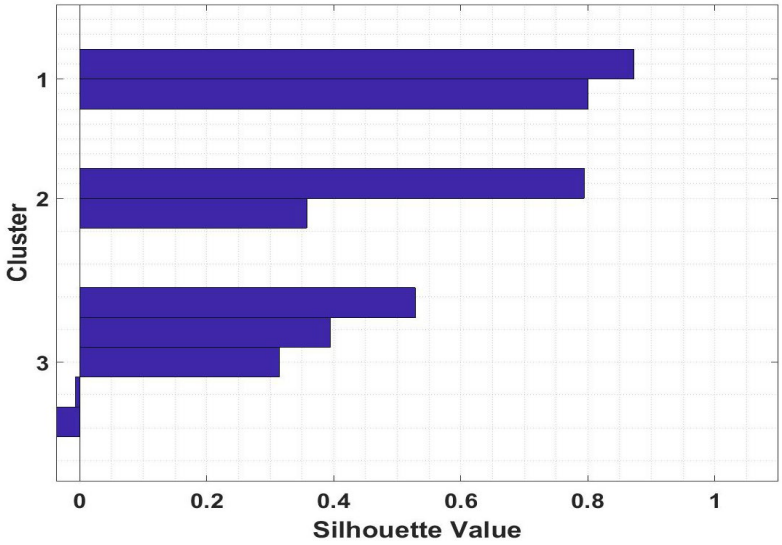

Figure 5.6 The silhouette value of K-means clusters

5.2.4 Discussion

It is feasible to monitor STS with single IMU according to excellent agreement with VICON and force plate. With the help of K-means cluster, it is possible to automatically identify the three strategies based on the four variables of trunk from the IMU. Other possible variables from the sensor can be further investigated to perform clustering. Besides, more IMUs may be put on the other locations of body like thigh and shank which can be used to estimate the hip and knee moment. It is necessary to recruit more subjects due to the small sample size at present.

5.3 Fall risk prediction among the seniors

5.3.1 Introduction

Falling has become one of the major causes to both fatal and non-fatal injuries among the elder adults. There is a high possibility that one third in adults over age 65 and half of the elder over 85 years old will fall in the next year, and a large portion of them will suffer an injury due to falling (Stevens, 2005). The following consequence after a fall will be that the fear of falling can

reduce the daily activities, leading to physical deterioration and social isolation (R. Y. Lee & Carlisle, 2011; Masud & Morris, 2001). Considering the adverse consequences of falls in the older adults, many research has been performed mainly focusing on identifying the factors of fall risk and targeted fall prevention (Buatois et al., 2008; Mirelman et al., 2012; Podsiadlo & Richardson, 1991; Rantz et al., 2015). One research revealed that falls and its related injuries can be predictable and preventable with specific interventions targeting the corresponding risk factors including muscle strength, balance and mobility (Gillespie et al., 2012). The initial step of an effective fall prevention program is to perform fall risk assessment to identify persons at high risk and then target specific interventions to reduce or eliminate falls. The Centers for Disease Control and Prevention (CDC) has recommended the older adults to perform fall risk screening at least annually by physicians (Stevens, 2013). However, due to several reasons such as unreliable subjective measures, high cost and clinical time constraints, effective fall risk assessment is still not routinely integrated into daily clinical practice (Sun & Sosnoff, 2018). Therefore, an accurate, inexpensive and easy-to-use fall risk assessment technique is needed.

With the development of Micro-Electro-Mechanical-System (MEMS), sensors became smaller and smaller. Then the sensors were gradually used in the biomechanics and human motion analysis due to its low cost, portability and convenience while the most commonly used optoelectronic motion capture system at present are very expensive, space-limited and complicated to implement. Taking advantage of wearable sensor technology, there have been a few studies focusing on fall risk assessment using some simple tests such five-time-sit-to-stand (FTSTS), gait and Timed-Up-and-Go (TUG) etc (Anwary, Yu, & Vassallo, 2018; Bautmans, Jansen, Van Keymolen, & Mets, 2011; Begg, Palaniswami, & Owen, 2005; Caby, Kieffer, de Saint Hubert, Cremer, & Macq, 2011; Doheny et al., 2013; Duncan, Leddy, & Earhart, 2011; Howcroft, Lemaire, & Kofman, 2016; Whitney et al., 2005), instead of the burdensome and time-consuming typical

clinical fall risk assessment tool like Tinetti test and Berg Balance Scale (Thorbahn & Newton, 1996; Tinetti, 1986).

FTSTS is a clinically accepted assessment for lower limb strength which is closely associated with balance dysfunction (Lord, Murray, Chapman, Munro, & Tiedemann, 2002) and fall risk (Doheny et al., 2013; Najafi, Aminian, Loew, Blanc, & Robert, 2002). In clinical application, the total time of FTSTS is often used as an indication marker for fall risk that the slower time indicates a higher risk of falling (Buatois et al., 2008; Doheny et al., 2013). Compared to old healthy group, the elder adults prone to fall have high possibility to show abnormalities in postural stability and balance control (Maki, 1997). Among older adults, the gait features such as gait speed and gait asymmetry are possibly reduced with the increasing of age which is related to future falls (Ejupi, Lord, & Delbaere, 2014). The results from several studies have suggested that gait assessment with wearable sensors can discriminate the fallers from non-fallers (Caby et al., 2011; Howcroft et al., 2016; Riva, Toebes, Pijnappels, Stagni, & van Dieen, 2013). As a standard mobility assessment tool, TUG test has been recommended by American Geriatrics Society (AGS) guidelines to identify the older adults with high fall risk (Greene, Doheny, Kenny, & Caulfield, 2014). The performing time of TUG is recorded to assess fall risk in the clinical practice. The classification performance of TUG between fallers and non-fallers have been significantly improved through extracting more spatiotemporal and kinematical data from wearable sensors (Greene et al., 2014).

Some previous studies evaluated the sensor-based fall risk prediction model compared to the data from clinical questionnaire and found that adding wearable sensors improved the fall risk prediction on the basis of clinical data from questionnaire (Greene et al., 2014; Rispens et al., 2015; van Schooten et al., 2015). A fall risk prediction model usually considers the sensor type, sensor location, number of sensors and type of machine learning algorithm (Howcroft, Kofman, &

Lemaire, 2013). One study has investigated the different combinations of two sensor types, four sensor locations and three types of models to classify the fallers among older adults. According to the results from chapter 4, it was shown that chest sensor alone can also achieve very good classification performance. So far, no studies investigated the classification performance using single sensor for fall risk prediction. Meanwhile, the selection of different activities may affect the fall risk prediction results.

This section presents a comprehensive investigation of a single sensor on the chest to predict the fall risk with three types of machine learning algorithms (k-Nearest Neighbor, Support Vector Machine and Naïve Bayesian) during three activities (FTSTS, Ten-meter Walking and TUG) among the older adults in the senior center. The goal of this study is to determine which activity is more effective for fall risk prediction and examine the accuracy of various classifiers provided by single chest sensor.

5.3.2 Method

A group of the older adults over age 60 including 18 males and 47 females were recruited from the senior centers in Charlotte, NC. The participants were divided into two groups - low fall risk (score < 4) and high fall risk (score >=4) according to a fall risk assessment questionnaire (Figure 5.7) suggested by Center for Disease Control and Prevention (CDC) (Rubenstein, Vivrette, Harker, Stevens, & Kramer, 2011). There were 49 subjects (37 females, 12 males, mean age 72.9 ± 7.0) in the low fall risk group and 16 subjects (12 females, 6 males, mean age 70.6 ± 8.5) in the high fall risk group. Potential subjects were excluded if they could not perform all the three activities without any assistive device. The study was conducted following an IRB approved protocol. All the participants were given an information sheet with verbal consent.

Please circle "Yes" or "No" for each statement below.			Why it matters
Yes (2)	No (0)	I have fallen in the past year.	People who have fallen once are likely to fall again.
Yes (2)	No (0)	I use or have been advised to use a cane or walker to get around safely.	People who have been advised to use a cane or walker may already be more likely to fall.
Yes (1)	No (0)	Sometimes I feel unsteady when I am walking.	Unsteadiness or needing support while walking are signs of poor balance.
Yes (1)	No (0)	I steady myself by holding onto furniture when walking at home.	This is also a sign of poor balance.
Yes (1)	No (0)	I am worried about falling.	People who are worried about falling are more likely to fall.
Yes (1)	No (0)	I need to push with my hands to stand up from a chair.	This is a sign of weak leg muscles, a major reason for falling.
Yes (1)	No (0)	I have some trouble stepping up onto a curb.	This is also a sign of weak leg muscles.
Yes (1)	No (0)	I often have to rush to the toilet.	Rushing to the bathroom, especially at night, increases your chance of falling.
Yes (1)	No (0)	I have lost some feeling in my feet.	Numbness in your feet can cause stumbles and lead to falls.
Yes (1)	No (0)	I take medicine that sometimes makes me feel light-headed or more tired than usual.	Side effects from medicines can sometimes increase your chance of falling.
Yes (1)	No (0)	I take medicine to help me sleep or improve my mood.	These medicines can sometimes increase your chance of falling.
Yes (1)	No (0)	I often feel sad or depressed.	Symptoms of depression, such as not feeling well or feeling slowed down, are linked to falls.
Total_____		Add up the number of points for each "yes" answer. If you scored 4 points or more, you may be at risk for falling.	

Figure 5.7 The self-report questionnaire for fall risk assessment (Rubenstein et al., 2011)

Participants were instructed to perform three tests consecutively – FTSTS, Ten-meter Walking (10MWT) and TUG with single sensor placed on the sternum (Figure 5.8). The local coordinate of the sensor was set as anatomical coordinate of human body where X is aligned with superior-inferior (SI) direction, Y is aligned with medial-lateral (ML) direction and Z is aligned with anterior-posterior (AP) direction. A standard height (46 cm) chair with no arm rest was used in the FTSTS. The participants were asked to keep arms folded in front of chest. Each participant performed the sit-to-stand and stand-to-sit five times under the instructions. Between each standing up and sitting down participant rested three seconds for the safety problems. During the 10MWT, each participant was asked to walk at their normal speed. TUG is a combination of sit-to-stand, walking (3 meter), turning and stand-to-sit test. All three tests were performed two times by each

subject. Before each test, subjects were required to keep static with their upper-body straight upward for three seconds.

The sensor used here was Opal IMU (APDM Inc., Portland, OR, USA) that encases 3-axis accelerometer, 3-axis gyroscope and 3-axis magnetometer. The mass is 22 g and the dimensions are 48.4mm x 36.1 mm x 13.4 mm. Data were collected under Robust Synchronized Streaming Mode at sampling frequency 128 Hz. A fourth-order Butterworth filter at cut-off frequency 6 Hz was applied to raw acceleration and angular velocity from sensor.

Figure 5.8 Test set-up with sensor placed on the sternum

For the FTSTS, each individual sit-to-stand and stand-to-sit time were computed through a threshold algorithm applied on the pitch angular velocity (Figure 5.9). Then the mean and coefficient of variation (CV) of the individual transition time were calculated. The maximum flexion/extension angular velocity in each sitting and standing trial were extracted and then mean and CV were computed. The root-mean-square (RMS) and jerk of the acceleration were computed for each individual trial along each direction (Doheny et al., 2013). Then mean and CV of these two features were also examined.

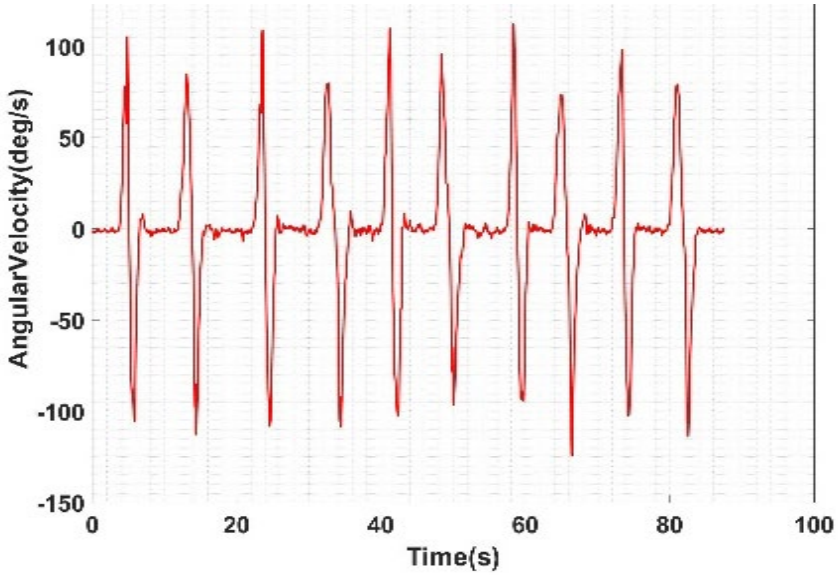

Figure 5.9 Typical example of the pitch angular velocity during FTSTS

In the 10MWT, the average and CV of peak and trough (P2T) values were obtained from acceleration along SI direction and angular velocity about ML direction. The step time was defined as the interval time between two consecutive peaks based on the vertical acceleration. And jerk of the acceleration along ML direction was used to determine the left/right step. Then the asymmetry of step time and P2T acceleration were calculated using the following equation (Balasubramanian, Bowden, Neptune, & Kautz, 2007). The percentage of acceleration frequencies in the first quantile of a Fast Fourier Transform (FFT) frequency plot was computed since a lower percentage indicates that more high frequency acceleration component exists in the signal which is linked to instability

of walking (Drover, Howcroft, Kofman, & Lemaire, 2017; Howcroft, Kofman, & Lemaire, 2017; Prieto, Myklebust, Hoffmann, Lovett, & Myklebust, 1996). Here the raw acceleration without low-pass filter was used to compute first quantile of FFT frequency.

$$Asymmetry(\%) = |(Right - Left)| / \max\{Right, Left\} \times 100 \quad (5\text{-}7)$$

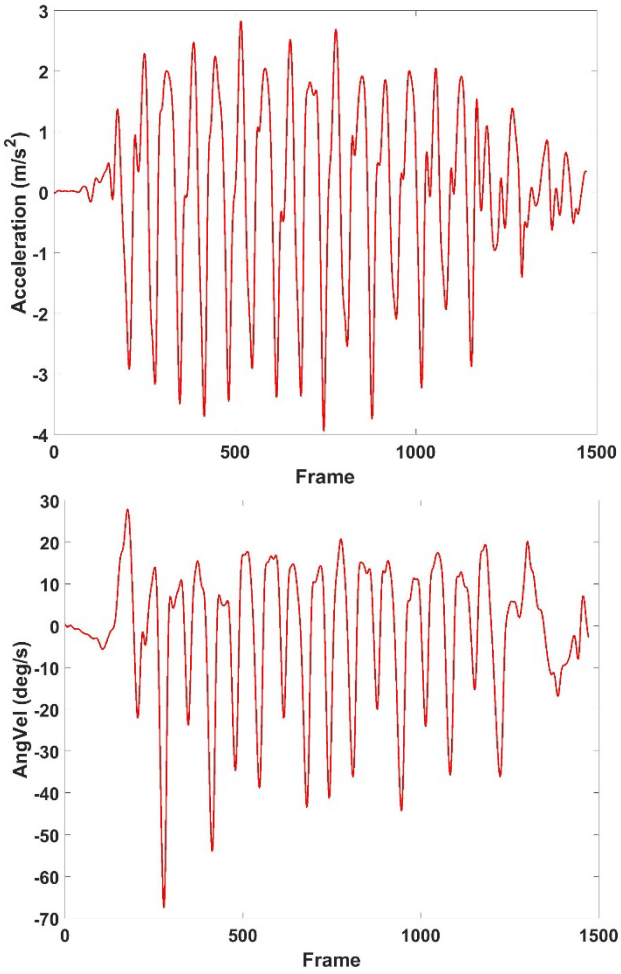

Figure 5.10 Top: typical example of the vertical acceleration during walking; Bottom: typical example of the pitch angular velocity during walking

For the TUG, the whole test was divided into three sections according to the pitch angular velocity of trunk (Figure 5.11): sit-to-stand, walking and stand-to-sit. The same features from each individual sit-to-stand/stand-to-sit and walking test were applied in each TUG segment. The two turning sections were located based on the yaw angular velocity about SI direction (Figure 5.12).

Then the mean maximum yaw angular velocity was obtained to examine the turning ability. The time for each phase: sit-to-stand, walking forward, turning I, walking backward, turning II and stand-to-sit were also calculated.

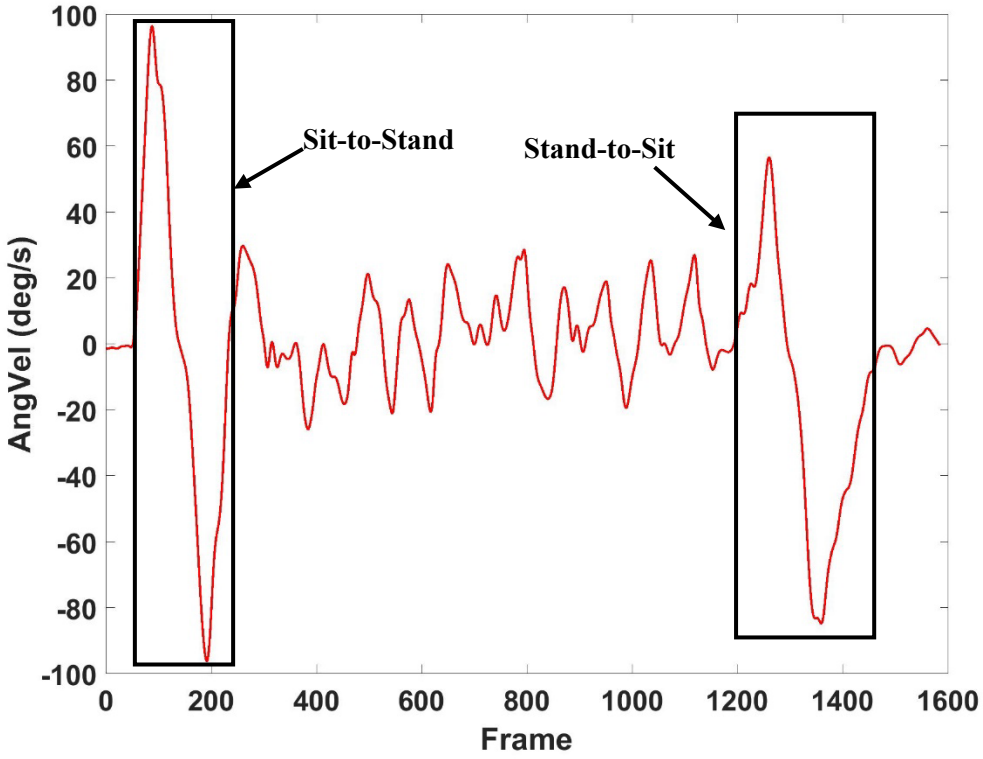

Figure 5.11 Typical example of pitch angular velocity during TUG

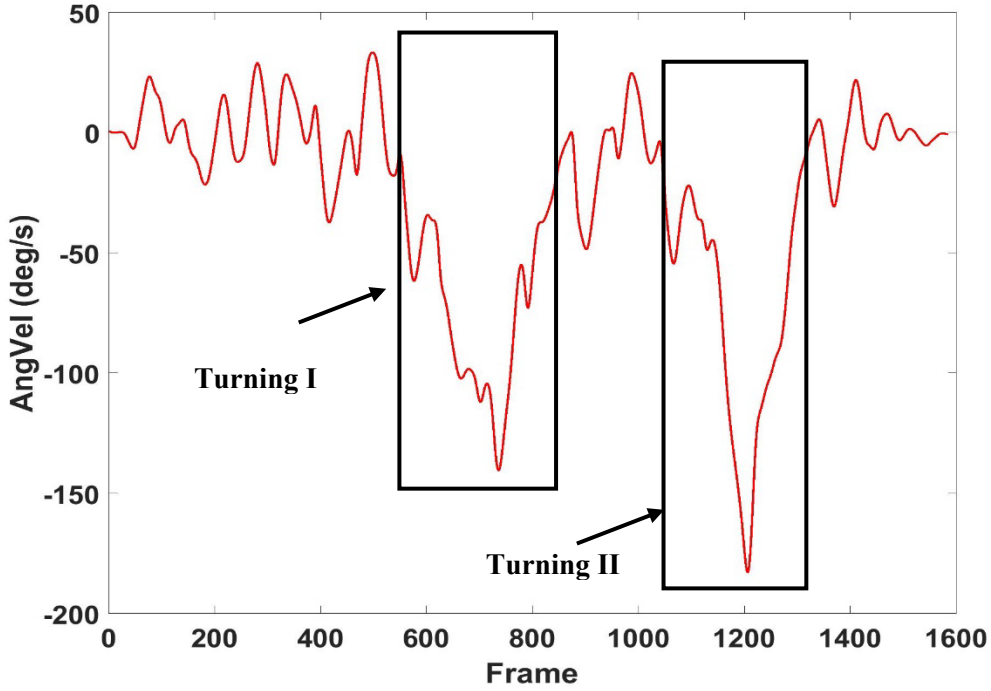

Figure 5.12 Typical example of yaw angular velocity during TUG

The descriptive statistics features including maximum, minimum, mean, variance and RMS of acceleration and angular velocity for all three directions were also computed as features input for classification model. All the features were applied with max-min normalization before inputting to the model.

Three machine learning algorithms were used here for fall risk classification: k-Nearest Neighbor (KNN), Support Vector Machine (SVM), Naïve Bayesian (NB). The models were developed with built-in machine learning algorithms in the MATLAB 2017a. The target variable is the level of risk – low or high determined by the fall risk assessment questionnaire. The whole data set was randomly separated into 80% training data and 20% testing data on the basis of target variable for all models. Accuracy, sensitivity and specificity were utilized to evaluate the performances of machine techniques. To determine the performance parameters, it is necessary to learn four academic terms including true positive (TP), true negative (TN), false positive (FP) and false negative (FN) from a confusion matrix. TP are the cases that the classification technique

shows the risk level of the subject matching the actual result that the subject is high risk. TN are cases when the algorithm predicted the subject as low fall risk which are the same as actual results. TP and TN are true decision given by the classification. Then the false decisions given by algorithms are false positive (FP) and false negative (FN). Accuracy measures how well the algorithm predicts the TP and TN overall (equation 4-2). Sensitivity (equation 4-3) measures the proportion of positives that when the subject is in the high fall risk group, the classifier also grouped this subject into high risk group. This is an important parameter to evaluate the performance of a model for fall risk classification which indicates how well the classifier predicts the risk level. Specificity (equation 4-4) measures the proportion of negatives that are correctly identified as low risk group. It refers to the ability of correctly identify low fall risk people and indicates how well the algorithm predicts the low fall risk group. A good classifier is expected to provide high accuracy, sensitivity and specificity.

For the KNN algorithm, the nearest neighbor k ($k>0$) needs to be selected properly for each specific problem due to its sensitivity to the composition of local dataset. The value of k was set as 3 to produce the best classification performance after ten trials of k from 1 to 10. SVM is originally designed to solve binary classification problems (Cortes & Vapnik, 1995; Greene et al., 2012; Shawe-Taylor, 2004). It is regarded as an important example of kernel methods which is one of the key areas in machine learning (Begg et al., 2005). The basic idea of SVM is to transform the input data into a higher dimensional space by means of a kernel function and then construct an optimal separating hyperplane between two classes in the transformed space (Liu, Zhang, & Lockhart, 2012; Ma et al., 2015). The kernel function used in this study was polynomial function with degrees three after trying the degree from one to seven. NB algorithm is a probabilistic classifier using maximum likelihood in the Bayesian settings which mainly relies on the mean of the training vectors and the covariance matrix of training vectors (Duda, 2001). All the data were processed

with custom MATLAB (The Mathworks Inc., Natick, MA, USA) code and the machine learning algorithms were adjusted based on the standard model in MATLAB.

5.3.3 Results & Discussion

Overall, the best classification result was achieved by TUG test with KNN model (sensitivity: 83.33%, specificity: 94.74%, accuracy: 92%). Among three classifiers, SVM showed the best average classification performance (sensitivity: 57.78% ± 15.40%, specificity: 88.89% ± 19.25%, accuracy: 82.06% ± 13.52%). In both KNN and SVM models, the mean sensitivity was significantly ($p < 0.01$) lower than the mean specificity while the sensitivity and specificity were almost identical in the NB model. The KNN model has largest variance (33.39%) of sensitivity with different test so it is essential to choose the proper test for feature extraction when using KNN algorithm. As NB algorithm achieved the best average sensitivity (70.68% ± 15.85%), it is recommended to use NB algorithm to assess the fall risk level when using single inertial sensor on the chest. The specificity indicating the true prediction rate of low risk group in the KNN and SVM algorithms were significantly higher than that of NB which means that to reach a better prediction results of low risk subjects, KNN and SVM can be either one of the options.

Among three tests, the features from TUG test produced the best mean sensitivity and accuracy (sensitivity: 70.00% ± 12.02%, accuracy: 85.33% ± 11.55%) for fall risk classification while 10MWT test achieved the best specificity (98.25% ± 3.04%). Since the main goal of the study is to predict if the participant has high fall risk according to the sensor measurement, TUG would be the recommended test. The combination of all the tests did not show any significant improvement of classification performance compared to each individual test with KNN and SVM models. This finding is different from the conclusion reported by Greene et al that the combining

sensor data from TUG, Balance test and FTSTS could significantly improve the accuracy of falls classification using SVM algorithm (Greene et al., 2014). There were two main reasons to explain this difference: one reason is the use of different features input and kernel functions in SVM model which will affect the final accuracy, the other reason is the different test like Balance test included. However, the combination sensor data did slight improve the accuracy of classification results using NB algorithm in this study.

Table 5-7 The performance of each classifier model using different features from three activities (unit: %)

KNN model	Sensitivity	Specificity	Accuracy
FTSTS	33.33	77.78	66.67
TUG	83.33	94.74	92.00
10MWT	20.00	94.74	79.17
Combination	33.33	77.78	66.67
NB model	**Sensitivity**	**Specificity**	**Accuracy**
FTSTS	88.89	33.33	75.00
TUG	60.00	75.00	72.00
10MWT	63.16	100.00	70.83
Combination	66.67	100.00	75.00
SVM model	**Sensitivity**	**Specificity**	**Accuracy**
FTSTS	66.67	66.67	66.67
TUG	66.67	100.00	92.00
10MWT	40.00	100.00	87.50
Combination	88.89	60.00	66.67

Compared to previous studies, the classification accuracy of each individual test from single chest IMU in this study were similar to the accuracy from multiple sensors in other fall risk classification research (Doheny et al., 2013; Greene et al., 2010; Howcroft et al., 2016). For the FTSTS, Doheny et al reported 74.4% accuracy of logistic regression model through data from two accelerometers on the thigh and sternum (Doheny et al., 2013). The accuracy of TUG test using logistic regression model from two shank IMUs was 76.8% slightly lower than the accuracy (85.33%) of TUG test achieved by this study (Greene et al., 2010). Then a multi-layer perceptron neural network with input parameters from pressure sensors and head, pelvis, and left shank accelerometers could only provide a slightly higher accuracy (84%) than the mean accuracy (79.17%) of gait test from single chest IMU.

Table 5-8 The mean and standard deviation of sensitivity, specificity and accuracy for each individual test and their combination using three different classifiers (unit: %)

Test	Sensitivity	Specificity	Accuracy
FTSTS	62.96 ± 27.96	59.26 ± 23.13	69.44 ± 4.81
TUG	70.00 ± 12.02	89.91 ± 13.18	85.33 ± 11.55
10MWT	41.05 ± 21.60	98.25 ± 3.04	79.17 ± 8.33
Combination	62.96 ± 27.96	79.26 ± 20.04	69.44 ± 4.81

There were a few limitations about this study. Due to the limited sample size, the classification performance could be varied from the true accuracy. The accuracy may be largely enhanced with more participants involved. In this study, the number of females was about three times higher than that of the male which might also affect the results. Because the female may have higher risk of falling from the statistic that the fall-related injury and death of women are twice

than those of men (Greenberg et al., 2016), the influence of gender factor should be included in future. The other limitation is that the features were directly input to the model without any selection. As so many features exist in each test, the importance of each feature is unknown to the model and some features may have strong correlations which can be removed from the feature vector. It will be promising to improve the performance of classifiers through dimension reduction techniques like Principal Component Analysis (PCA) or filter feature selection methods like Relief-F. In addition, the self-report questionnaire to evaluate fall risks may overestimate the risk level. The future study can examine the performance of each subject with inertial sensors in a longitudinal study design.

5.3.4 Conclusion

A single chest sensor-based fall risk assessment method was developed using different types of tests and classification models. Based on the clinical assessment questionnaire, the sensor-based model could predict the fall risk level through sensor data. The TUG test provided the best classification results for fall risk classification. The combination of multiple tests did not improve the classification performance. SVM model is the best machine learning technique among three models for fall risk classification. Future work could focus on developing more complicated machine learning techniques and using various feature selections methods to choose the optimal features. Overall, the wearable sensor-based fall risk classification model has potential to improve the diagnosis of elder adults with risk of falling and allow pre-intervention to prevent future falls.

CHAPTER 6: SUMMARY AND FUTURE WORK

6.1 Summary

This objective of this dissertation was to investigate the feasibility, reliability and repeatability of using IMU sensors to assess fall risk for clinical use. It is important to find the gaps between usage of IMU and clinical use and develop methods to fill the gaps. Four major contributions were made in this dissertation.

The first contribution was to examine the accuracy of IMU sensors if it meets the need of clinical use and to validate with a stereo-photogrammetry system. The validation tests were performed on both rigid body and human body. The rigid body tests have demonstrated that the commercial Opal IMU has excellent accuracy and precision of acceleration (mean accuracy 0.77 ± 0.41 m/s^2 and mean precision 0.36 ± 0.21 m/s^2) and angle (average accuracy 2.42° ± 2.50° and average precision 1.91° ± 1.48°) output which fits the requirement of clinical study. The static and dynamic RMSE values for sensor orientations on human body were within 2.5°, which is quite close to manufacturer's reported static (roll/pitch: 1.15°, heading: 1.5°) and dynamic accuracy (2.80°) estimates. During the data processing procedure, the detailed signal processing, which mainly focused on minimizing the noise and drift and coordinate transformation were revealed here. A simple method of coordinate transformation was used to compare IMU data and data from the reference system in the same global frame. The proprietary built-in sensor fusion algorithm was verified by a simple complementary filter using gradient descent algorithm. Both of the static and dynamic orientation accuracy from rigid body tests were within 2° achieved by built-in Kalman filter. The two sensor fusion algorithms exhibited no significant difference of RMSE values comparing to the stereo-photogrammetry measuring system. The heading angle showed the largest error among the angle measurements around three axes in both static and dynamic tests from the Opal sensor. Overall, the accuracy and precision of IMU measurements are sufficient for human

motion applications without excluding the soft tissue artifact and unexpected sensor movement on the human body.

The second contribution was that a simple template of magnetic mapping was built to quantify the magnetic disturbances and a simplified interpolation model was developed to compensate the heading angle error in the lab settings. A custom-made device was built to carry out the mapping of magnetic field in the motion lab. Two important factors including the location in three dimensional space and time were considered in the comparison of magnetic field and heading angle error between static and dynamic tests. The heading estimation errors from static tests were significantly larger than that of dynamic tests. The time factor did not show significant influence to the heading angle errors. The simplified interpolation model was derived from multiple locations in the static tests and then was applied on the new locations in-between to validate the model. The compensation method did improve the accuracy of heading angles in the static test. It was concluded that it is essential to map the magnetic field in the test area before experiment and start in an undisturbed field when performing the test with inertial sensors. It was recommended that placing the IMUs away from the floor is better option due to the larger heading angle errors close to the floor.

The third contribution was that multiple sensor configurations were evaluated among young healthy subjects, old healthy subjects and Parkinson's disease (PD) patients with six sensors placed on the body. Then the optimal configurations was explored according to the classification performance from three machine learning techniques. It was shown that the ability of wearable sensors based on gait features can assist to discriminate the patients with PD from the young healthy and old healthy individuals depending on the number and location of sensors placed on the human body. The classification accuracies were not directly affected by the increasing number of sensors. The optimal sensor configuration was achieved by the sensors placed on chest, wrist and shank

together. A single sensor configuration can also produce very high accuracy like the chest sensor. The choice of machine learning techniques did have influence on the final classification performances. Here, the Naïve Bayesian algorithm was recommended to differentiate the PD patients.

The fourth contribution was to apply various machine learning techniques to classify the fall risk among sixty-five older adults from the senior center using only a single IMU placed in front of the chest. Before the fall risk classification test, the feasibility of single chest IMU on the subjects during walking and sitting and standing was validated with a VICON motion capture system. It was concluded that it is feasible to apply single IMU on the sternum in the gait analysis to measure orientation angles of trunk and vertical acceleration, velocity and position. Step time from vertical acceleration and peak-to-trough vertical acceleration of IMU could be used to differentiate the gait between patients and healthy people. Five-time-sit-to-stand could be applied to identify the various chair-rise strategy among the healthy group. A self-report questionnaire was provided as a common clinical assessment to divide sixty-five senior people into two risk levels. The overall results have shown that TUG test provided the best classification results for fall risk classification and the combination of multiple tests did not improve the classification performance. SVM model is the best machine learning technique among three models for fall risk classification. Overall, the wearable IMU sensor-based fall risk classification model has potential to improve the diagnosis of elder adults with risk of falling and allow pre-intervention to prevent future falls.

6.2 Future work

This dissertation is a starting point for wearable inertial sensors in clinical application. It presents a promising analysis tool - IMU that can potentially assess the fall risk and diagnose the

various disease associated with motor dysfunction. Compared to regular physical performance test in clinic, IMU can quantitatively measure the balance and gait of people through consistent and accurate sensor data and continuously monitor the subject's motion and health status, instead of subjective evaluation by clinicians based on their experience. The experimental results of sensor validation, configuration and fall risk classification has proved the feasibility and reliability of proposed technique. However, more work are still needed for further application in clinic. The following section lists the future works.

1. Even though the accuracy and precision of IMU on the rigid body and human body have been validated in the chapter 2, the IMUs used are developed by commercial company which owns their proprietary algorithm and specification. There is no way to improve the accuracy of commercial sensors through the internal hardware part. So it is necessary to develop our own sensor system including hardware and software under the control. A piece of jacket with multiple pre-installed sensors on different locations can save time of set-up and increase the consistency of sensor placement. Then a well-developed software can not only collect the raw data but also preprocess the data and output the specific parameters for different types of test and sensor location.
2. For the magnetic disturbances problem, the compensation algorithm at present is only provided for the static test. The fact that the heading angle errors at the pre-defined points during dynamic tests did not exhibit similar accuracy as those from the results of static test still needs more investigation. There are two possible reasons related to this situation: initial heading angle and convergence rate of Kalman filter. An external magnetic field detector can be used to confirm the starting position without any magnetic disturbances. With self-developed sensors, the convergence rate could be adjusted to verify the reason.

3. The optimal sensor configuration was determined among several locations on the body which is quite limited. In the future, all the subjects will be instructed to take full body scan to generate CAD model. Then this human model can be used in the simulation software through adding the sensors at any locations on the body and providing all kinds of motion test. The error caused by soft tissue artefact can be considered in this rigid human body model based on certain model. This will help the clinicians determine the best sensor placement location for each individual before each test.
4. A large number of subjects is highly recommended to validate the fall risk classification performance of wearable sensors. In this dissertation, only sixty-five elder adults from senior center were recruited. More subjects including healthy seniors and patients with various motion-related disease need to be recruited for future evaluation of fall risk classification with wearable sensors. Different machine learning algorithms can be tested in the later study. Various feature selection methods will be applied to choose the comparatively important features which may improve the classifier performance. A long-term tracking of fall status with IMUs for each subject will be implemented to estimate the risk level, instead of the self-report fall risk questionnaire.

REFERENCES

Allseits, E., Lucarevic, J., Gailey, R., Agrawal, V., Gaunaurd, I., & Bennett, C. (2017). The development and concurrent validity of a real-time algorithm for temporal gait analysis using inertial measurement units. Journal of Biomechanics, 55, 27-33. doi:10.1016/j.jbiomech.2017.02.016

Alvarez, J. C., Gonzalez, R. C., Alvarez, D., Lopez, A. M., & Rodriguez-Uria, J. (2007). Multisensor approach to walking distance estimation with foot inertial sensing. 2007 Annual International Conference of the Ieee Engineering in Medicine and Biology Society, Vols 1-16, 5720-5723.

Aminian, K., Najafi, B., Bula, C., Leyvraz, P. F., & Robert, P. (2002). Spatio-temporal parameters of gait measured by an ambulatory system using miniature gyroscopes. Journal of Biomechanics, 35(5), 689-699.

Anwary, A. R., Yu, H., & Vassallo, M. (2018). An Automatic Gait Feature Extraction Method for Identifying Gait Asymmetry Using Wearable Sensors. Sensors (Basel), 18(2). doi:10.3390/s18020676

Aurora Bueno-Cavanillas, F. P.-R., JJ Jimenez-Moleon, CA Peinado-Alonso, R Galvez-Vargas. (Sep 1, 2000). Risk factors in falls among the elderly according to extrinsic and intrinsic precipitating causes. European journal of epidemiology, 16(9), 849-859.

Bachmann, E. R., Yun, X. P., & Brumfield, A. (2007). Limitations of attitude estimation algorithms for inertial/Magnetic sensor modules. Ieee Robotics & Automation Magazine, 14(3), 76-87. doi:10.1109/M-Ra.2007.901320

Bachmann, E. R., Yun, X. P., & Peterson, C. W. (2004). An investigation of the effects of magnetic variations on inertial/magnetic orientation sensors. 2004 Ieee International Conference on Robotics and Automation, Vols 1- 5, Proceedings, 1115-1122. doi:Doi 10.1109/Robot.2004.1307974

Bae, J., & Tomizuka, M. (2013). A tele-monitoring system for gait rehabilitation with an inertial measurement unit and a shoe-type ground reaction force sensor. Mechatronics, 23(6), 646-651. doi:10.1016/j.mechatronics.2013.06.007

Balasubramanian, C. K., Bowden, M. G., Neptune, R. R., & Kautz, S. A. (2007). Relationship between step length asymmetry and walking performance in subjects with chronic hemiparesis. Arch Phys Med Rehabil, 88(1), 43-49. doi:10.1016/j.apmr.2006.10.004

Bauer, C. M., Rast, F. M., Ernst, M. J., Kool, J., Oetiker, S., Rissanen, S. M., . . . Kankaanpaa, M. (2015). Concurrent validity and reliability of a novel wireless inertial measurement system to assess trunk movement. J Electromyogr Kinesiol, 25(5), 782-790. doi:10.1016/j.jelekin.2015.06.001

Bautmans, I., Jansen, B., Van Keymolen, B., & Mets, T. (2011). Reliability and clinical correlates of 3D-accelerometry based gait analysis outcomes according to age and fall-risk. Gait Posture, 33(3), 366-372. doi:10.1016/j.gaitpost.2010.12.003

Begg, R. K., Palaniswami, M., & Owen, B. (2005). Support vector machines for automated gait classification. IEEE Trans Biomed Eng, 52(5), 828-838. doi:10.1109/TBME.2005.845241

Bergamini, E., Ligorio, G., Summa, A., Vannozzi, G., Cappozzo, A., & Sabatini, A. M. (2014). Estimating Orientation Using Magnetic and Inertial Sensors and Different Sensor Fusion

Approaches: Accuracy Assessment in Manual and Locomotion Tasks. Sensors, 14(10), 18625-18649. doi:10.3390/s141018625

Bianchi, F., Redmond, S. J., Narayanan, M. R., Cerutti, S., & Lovell, N. H. (2010). Barometric Pressure and Triaxial Accelerometry-Based Falls Event Detection. Ieee Transactions on Neural Systems and Rehabilitation Engineering, 18(6), 619-627. doi:10.1109/Tnsre.2010.2070807

Bo, Y., Tian, B., Dingguo, Z., Carender, W., Sienko, K. H., & Shull, P. B. (2015). Determining inertial measurement unit placement for estimating human trunk sway while standing, walking and running. Conf Proc IEEE Eng Med Biol Soc, 2015, 4651-4654. doi:10.1109/EMBC.2015.7319431

Bolink, S. A., Naisas, H., Senden, R., Essers, H., Heyligers, I. C., Meijer, K., & Grimm, B. (2016). Validity of an inertial measurement unit to assess pelvic orientation angles during gait, sit-stand transfers and step-up transfers: Comparison with an optoelectronic motion capture system. Med Eng Phys, 38(3), 225-231. doi:10.1016/j.medengphy.2015.11.009

Bourke, A. K., O'Brien, J. V., & Lyons, G. M. (2007). Evaluation of a threshold-based tri-axial accelerometer fall detection algorithm. Gait Posture, 26(2), 194-199. doi:10.1016/j.gaitpost.2006.09.012

Bourke, A. K., van de Ven, P., Gamble, M., O'Connor, R., Murphy, K., Bogan, E., . . . Nelson, J. (2010). Assessment of waist-worn tri-axial accelerometer based fall-detection algorithms using continuous unsupervised activities. Conf Proc IEEE Eng Med Biol Soc, 2010, 2782-2785. doi:10.1109/IEMBS.2010.5626364

Buatois, S., Miljkovic, D., Manckoundia, P., Gueguen, R., Miget, P., Vancon, G., . . . Benetos, A. (2008). Five times sit to stand test is a predictor of recurrent falls in healthy community-living subjects aged 65 and older. J Am Geriatr Soc, 56(8), 1575-1577. doi:10.1111/j.1532-5415.2008.01777.x

Buckley, C., Galna, B., Rochester, L., & Mazza, C. (2017). Quantification of upper body movements during gait in older adults and in those with Parkinson's disease: impact of acceleration realignment methodologies. Gait Posture, 52, 265-271. doi:10.1016/j.gaitpost.2016.11.047

Caby, B., Kieffer, S., de Saint Hubert, M., Cremer, G., & Macq, B. (2011). Feature extraction and selection for objective gait analysis and fall risk assessment by accelerometry. Biomedical Engineering Online, 10, 1. doi:10.1186/1475-925X-10-1

Caramia, C., Bernabucci, I., D'Anna, C., De Marchis, C., & Schmid, M. (2017). Gait parameters are differently affected by concurrent smartphone-based activities with scaled levels of cognitive effort. PLoS One, 12(10), e0185825. doi:10.1371/journal.pone.0185825

Carcreff, L., Gerber, C. N., Paraschiv-Ionescu, A., De Coulon, G., Newman, C. J., Armand, S., & Aminian, K. (2018). What is the Best Configuration of Wearable Sensors to Measure Spatiotemporal Gait Parameters in Children with Cerebral Palsy? Sensors (Basel), 18(2). doi:10.3390/s18020394

Caruso, M. (1997). Applications of Magnetoresistive Sensors in Navigation Systems. Retrieved from

Chang, L. B., Zha, F., & Qin, F. J. (2017). Indirect Kalman Filtering Based Attitude Estimation for Low-Cost Attitude and Heading Reference Systems. Ieee-Asme Transactions on Mechatronics, 22(4), 1850-1858. doi:10.1109/Tmech.2017.2698639

Clauser, C. (1969). Weight, Volume and Center of Mass of Segments of the Human Body. Retrieved from Wright- Patterson Air Force Base, Ohio:

Cooper, G., Sheret, I., McMillan, L., Siliverdis, K., Sha, N., Hodgins, D., . . . Howard, D. (2009). Inertial sensor-based knee flexion/extension angle estimation. Journal of Biomechanics, 42(16), 2678-2685. doi:10.1016/j.jbiomech.2009.08.004

Cortes, C., & Vapnik, V. (1995). Support-Vector Networks. Machine Learning, 20(3), 273-297. doi:Doi 10.1023/A:1022627411411

Currie, L. (2008). Fall and Injury Prevention. In R. G. Hughes (Ed.), Patient Safety and Quality: An Evidence-Based Handbook for Nurses. Rockville (MD).

Cuzzolin, F., Sapienza, M., Esser, P., Saha, S., Franssen, M. M., Collett, J., & Dawes, H. (2017). Metric learning for Parkinsonian identification from IMU gait measurements. Gait Posture, 54, 127-132. doi:10.1016/j.gaitpost.2017.02.012

de Marina, H. G., Espinosa, F., & Santos, C. (2012). Adaptive UAV attitude estimation employing unscented Kalman Filter, FOAM and low-cost MEMS sensors. Sensors (Basel), 12(7), 9566-9585. doi:10.3390/s120709566

de Vries, W. H. K., Veeger, H. E. J., Baten, C. T. M., & van der Helm, F. C. T. (2009). Magnetic distortion in motion labs, implications for validating inertial magnetic sensors. Gait & Posture, 29(4), 535-541. doi:10.1016/j.gaitpost.2008.12.004

Diebel, J. (2006). Representing Attitude: Euler Angles, Unit Quaternions, and Rotation Vectors. Retrieved from

Doheny, E. P., Walsh, C., Foran, T., Greene, B. R., Fan, C. W., Cunningham, C., & Kenny, R. A. (2013). Falls classification using tri-axial accelerometers during the five-times-sit-to-stand test. Gait Posture, 38(4), 1021-1025. doi:10.1016/j.gaitpost.2013.05.013

Dorsey, E. R., Constantinescu, R., Thompson, J. P., Biglan, K. M., Holloway, R. G., Kieburtz, K., . . . Tanner, C. M. (2007). Projected number of people with Parkinson disease in the most populous nations, 2005 through 2030. Neurology, 68(5), 384-386. doi:10.1212/01.wnl.0000247740.47667.03

Drover, D., Howcroft, J., Kofman, J., & Lemaire, E. D. (2017). Faller Classification in Older Adults Using Wearable Sensors Based on Turn and Straight-Walking Accelerometer-Based Features. Sensors (Basel), 17(6). doi:10.3390/s17061321

Duda, R. H., P.E.; Stork, D.G.,. (2001). Pattern Classification (2nd ed.). New York, NY, USA: Wiley.

Duncan, R. P., Leddy, A. L., & Earhart, G. M. (2011). Five times sit-to-stand test performance in Parkinson's disease. Arch Phys Med Rehabil, 92(9), 1431-1436. doi:10.1016/j.apmr.2011.04.008

Ejupi, A., Lord, S. R., & Delbaere, K. (2014). New methods for fall risk prediction. Curr Opin Clin Nutr Metab Care, 17(5), 407-411. doi:10.1097/MCO.0000000000000081

Eric Udd. (Nov 2, 2016). History of the fiber-optic gyro. Retrieved from http://www.spie.org/newsroom/history-of-the-fiber-optic-gyro-in-spie-professional

Esser, P., Dawes, H., Collett, J., Feltham, M. G., & Howells, K. (2012). Validity and inter-rater reliability of inertial gait measurements in Parkinson's disease: a pilot study. J Neurosci Methods, 205(1), 177-181. doi:10.1016/j.jneumeth.2012.01.005

Esser, P., Dawes, H., Collett, J., & Howells, K. (2009). IMU: Inertial sensing of vertical CoM movement. Journal of Biomechanics, 42(10), 1578-1581. doi:10.1016/j.jbiomech.2009.03.049

Euston, M., Coote, P., Mahony, R., Kim, J., & Hamel, T. (2008). A Complementary Filter for Attitude Estimation of a Fixed-Wing UAV. 2008 Ieee/Rsj International Conference on Robots and Intelligent Systems, Vols 1-3, Conference Proceedings, 340-345. doi:Doi 10.1109/Iros.2008.4650766

Favre, J., Aissaoui, R., Jolles, B. M., de Guise, J. A., & Aminian, K. (2009). Functional calibration procedure for 3D knee joint angle description using inertial sensors. Journal of Biomechanics, 42(14), 2330-2335. doi:10.1016/j.jbiomech.2009.06.025

Galli, M., Cimolin, V., Crivellini, M., & Campanini, I. (2008). Quantitative analysis of sit to stand movement: experimental set-up definition and application to healthy and hemiplegic adults. Gait Posture, 28(1), 80-85.

Gillespie, L. D., Robertson, M. C., Gillespie, W. J., Sherrington, C., Gates, S., Clemson, L. M., & Lamb, S. E. (2012). Interventions for preventing falls in older people living in the community. Cochrane Database Syst Rev(9), CD007146. doi:10.1002/14651858.CD007146.pub3

Godinho, C., Domingos, J., Cunha, G., Santos, A. T., Fernandes, R. M., Abreu, D., . . . Ferreira, J. J. (2016). A systematic review of the characteristics and validity of monitoring technologies to assess Parkinson's disease. J Neuroeng Rehabil, 13, 24. doi:10.1186/s12984-016-0136-7

Godwin, A., Agnew, M., & Stevenson, J. (2009). Accuracy of inertial motion sensors in static, quasistatic, and complex dynamic motion. J Biomech Eng, 131(11), 114501. doi:10.1115/1.4000109

Gonzalez, R. C., Lopez, A. M., Rodriguez-Uria, J., Alvarez, D., & Alvarez, J. C. (2010). Real-time gait event detection for normal subjects from lower trunk accelerations. Gait Posture, 31(3), 322-325. doi:10.1016/j.gaitpost.2009.11.014

Greenberg, M. R., Moore, E. C., Nguyen, M. C., Stello, B., Goldberg, A., Barraco, R. D., . . . Kane, B. G. (2016). Perceived Fall Risk and Functional Decline: Gender Differences in Patient's Willingness to Discuss Fall Risk, Fall History, or to Have a Home Safety Evaluation. Yale J Biol Med, 89(2), 261-267.

Greene, B. R., Doheny, E. P., Kenny, R. A., & Caulfield, B. (2014). Classification of frailty and falls history using a combination of sensor-based mobility assessments. Physiol Meas, 35(10), 2053-2066. doi:10.1088/0967-3334/35/10/2053

Greene, B. R., McGrath, D., Walsh, L., Doheny, E. P., McKeown, D., Garattini, C., . . . Kenny, R. A. (2012). Quantitative falls risk estimation through multi-sensor assessment of standing balance. Physiological Measurement, 33(12), 2049-2063. doi:10.1088/0967-3334/33/12/2049

Greene, B. R., O'Donovan, A., Romero-Ortuno, R., Cogan, L., Scanaill, C. N., & Kenny, R. A. (2010). Quantitative falls risk assessment using the timed up and go test. IEEE Trans Biomed Eng, 57(12), 2918-2926. doi:10.1109/TBME.2010.2083659

Grimpampi, E., Bonnet, V., Taviani, A., & Mazza, C. (2013). Estimate of lower trunk angles in pathological gaits using gyroscope data. Gait Posture, 38(3), 523-527. doi:10.1016/j.gaitpost.2013.01.031

Grimpampi, E., Oesen, S., Halper, B., Hofmann, M., Wessner, B., & Mazza, C. (2015). Reliability of gait variability assessment in older individuals during a six-minute walk test. Journal of Biomechanics, 48(15), 4185-4189. doi:10.1016/j.jbiomech.2015.10.008

Haines, T. P., Nitz, J., Grieve, J., Barker, A., Moore, K., Hill, K., . . . Robinson, A. (2013). Cost per fall: a potentially misleading indicator of burden of disease in health and residential care settings. J Eval Clin Pract, 19(1), 153-161. doi:10.1111/j.1365-2753.2011.01786.x

Hajdu, S., Brassai, S. T., & Szekely, I. (2017). Complementary filter based sensor fusion on FPGA platforms. 2017 International Conference on Optimization of Electrical and Electronic Equipment (Optim) & 2017 Intl Aegean Conference on Electrical Machines and Power Electronics (Acemp), 851-856.

Henriksen, M., Lund, H., Moe-Nilssen, R., Bliddal, H., & Danneskiod-Samsoe, B. (2004). Test-retest reliability of trunk accelerometric gait analysis. Gait Posture, 19(3), 288-297. doi:10.1016/S0966-6362(03)00069-9

Hitcho, E. B., Krauss, M. J., Birge, S., Claiborne Dunagan, W., Fischer, I., Johnson, S., . . . Fraser, V. J. (2004). Characteristics and circumstances of falls in a hospital setting: a prospective analysis. J Gen Intern Med, 19(7), 732-739. doi:10.1111/j.1525-1497.2004.30387.x

Howcroft, J., Kofman, J., & Lemaire, E. D. (2013). Review of fall risk assessment in geriatric populations using inertial sensors. J Neuroeng Rehabil, 10(1), 91. doi:10.1186/1743-0003-10-91

Howcroft, J., Kofman, J., & Lemaire, E. D. (2017). Feature selection for elderly faller classification based on wearable sensors. J Neuroeng Rehabil, 14(1), 47. doi:10.1186/s12984-017-0255-9

Howcroft, J., Lemaire, E. D., & Kofman, J. (2016). Wearable-Sensor-Based Classification Models of Faller Status in Older Adults. PLoS One, 11(4), e0153240. doi:10.1371/journal.pone.0153240

Islam, T., Islam, M. S., Shajid-Ul-Mahmud, M., & Hossam-E-Haider, M. (2017). Comparison of Complementary and Kalman Filter Based Data Fusion for Attitude Heading Reference System. Proceedings of the 1st International Conference on Mechanical Engineering and Applied Science (Icmeas 2017), 1919. doi:Unsp 020002

10.1063/1.5018520

jadmin. (April 19, 2016). Gyroscope. Retrieved from http://sensorwiki.org/doku.php/sensors/gyroscope

Johnston, W., Patterson, M., O'Mahony, N., & Caulfield, B. (2016). Validation and comparison of shank and lumbar-worn IMUs for step time estimation. Biomed Tech (Berl). doi:10.1515/bmt-2016-0120

Kangas, M., Konttila, A., Lindgren, P., Winblad, I., & Jamsa, T. (2008). Comparison of low-complexity fall detection algorithms for body attached accelerometers. Gait Posture, 28(2), 285-291. doi:10.1016/j.gaitpost.2008.01.003

Kangas, M., Konttila, A., Winblad, I., & Jamsa, T. (2007). Determination of simple thresholds for accelerometry-based parameters for fall detection. 2007 Annual International Conference of the Ieee Engineering in Medicine and Biology Society, Vols 1-16, 1367-1370. doi:Doi 10.1109/Iembs.2007.4352552

Kavanagh, J. J., Barrett, R. S., & Morrison, S. (2004). Upper body accelerations during walking in healthy young and elderly men. Gait Posture, 20(3), 291-298. doi:10.1016/j.gaitpost.2003.10.004

Kavanagh, J. J., Morrison, S., James, D. A., & Barrett, R. (2006). Reliability of segmental accelerations measured using a new wireless gait analysis system. Journal of Biomechanics, 39(15), 2863-2872. doi:10.1016/j.jbiomech.2005.09.012

Keijsers, N. L., Horstink, M. W., & Gielen, S. C. (2006). Ambulatory motor assessment in Parkinson's disease. Mov Disord, 21(1), 34-44. doi:10.1002/mds.20633

Kendell, C., & Lemaire, E. D. (2009). Effect of mobility devices on orientation sensors that contain magnetometers. Journal of Rehabilitation Research and Development, 46(7), 957-962. doi:10.1682/Jrrd.2008.09.0132

Kleiner, A. F. R., Pacifici, I., Vagnini, A., Camerota, F., Celletti, C., Stocchi, F., . . . Galli, M. (2018). Timed Up and Go evaluation with wearable devices: Validation in Parkinson's disease. J Bodyw Mov Ther, 22(2), 390-395. doi:10.1016/j.jbmt.2017.07.006

Kose, A., Cereatti, A., & Della Croce, U. (2012). Bilateral step length estimation using a single inertial measurement unit attached to the pelvis. J Neuroeng Rehabil, 9, 9. doi:10.1186/1743-0003-9-9

Leccadito, M. (2013). A Kalman Filter Based Attitude Heading Reference System Using a Low Cost Inertial Measurement Unit. Virginia Commonwealth University,

Lee, J. K., & Choi, M. J. (2017). A Sequential Orientation Kalman Filter for AHRS Limiting Effects of Magnetic Disturbance to Heading Estimation. Journal of Electrical Engineering & Technology, 12(4), 1675-1682. doi:10.5370/Jeet.2017.12.4.1675

Lee, R. Y., & Carlisle, A. J. (2011). Detection of falls using accelerometers and mobile phone technology. Age Ageing, 40(6), 690-696. doi:10.1093/ageing/afr050

Ligorio, G., Bergamini, E., Pasciuto, I., Vannozzi, G., Cappozzo, A., & Sabatini, A. M. (2016). Assessing the Performance of Sensor Fusion Methods: Application to Magnetic-Inertial-Based Human Body Tracking. Sensors (Basel), 16(2), 153. doi:10.3390/s16020153

Liu, J., Zhang, X., & Lockhart, T. E. (2012). Fall risk assessments based on postural and dynamic stability using inertial measurement unit. Saf Health Work, 3(3), 192-198. doi:10.5491/SHAW.2012.3.3.192

Lord, S. R., Murray, S. M., Chapman, K., Munro, B., & Tiedemann, A. (2002). Sit-to-stand performance depends on sensation, speed, balance, and psychological status in addition to strength in older people. J Gerontol A Biol Sci Med Sci, 57(8), M539-543.

Luinge, H. J., & Veltink, P. H. (2005a). Measuring orientation of human body segments using miniature gyroscopes and accelerometers. Medical & Biological Engineering & Computing, 43(2), 273-282.

Luinge, H. J., & Veltink, P. H. (2005b). Measuring orientation of human body segments using miniature gyroscopes and accelerometers. Medical & Biological Engineering & Computing, 43(2), 273-282. doi:Doi 10.1007/Bf02345966

Ma, H. T., Zhang, X. R., Yang, H. T., Liu, J. X., Chen, M. T., & Gong, P. (2015). SVM-based Approach for Human Daily Motion Recognition. Tencon 2015 - 2015 Ieee Region 10 Conference.

Madgwick, S. O. H., Harrison, A. J. L., & Vaidyanathan, R. (2011). Estimation of IMU and MARG orientation using a gradient descent algorithm. 2011 Ieee International Conference on Rehabilitation Robotics (Icorr).

Maki, B. E. (1997). Gait changes in older adults: predictors of falls or indicators of fear. J Am Geriatr Soc, 45(3), 313-320.

Maklouf, O. A. A. (2014). Performance Evaluation of GPS\ INS Main Integration Approach. International Journal of Mechanical,Aerospace, Industrial, Mechatronic and Manufacturing Engineering, 8(2), 476-484.

Mancini, M., Priest, K. C., Nutt, J. G., & Horak, F. B. (2012). Quantifying freezing of gait in Parkinson's disease during the instrumented timed up and go test. Conf Proc IEEE Eng Med Biol Soc, 2012, 1198-1201. doi:10.1109/EMBC.2012.6346151

Masud, T., & Morris, R. O. (2001). Epidemiology of falls. Age Ageing, 30 Suppl 4, 3-7.

Mayo Clinic. (2018). Parkinson's disease. Retrieved from https://www.mayoclinic.org/diseases-conditions/parkinsons-disease/symptoms-causes/syc-20376055

Mazza, C., Donati, M., McCamley, J., Picerno, P., & Cappozzo, A. (2012). An optimized Kalman filter for the estimate of trunk orientation from inertial sensors data during treadmill walking. Gait Posture, 35(1), 138-142. doi:10.1016/j.gaitpost.2011.08.024

McCamley, J., Donati, M., Grimpampi, E., & Mazza, C. (2012). An enhanced estimate of initial contact and final contact instants of time using lower trunk inertial sensor data. Gait Posture, 36(2), 316-318. doi:10.1016/j.gaitpost.2012.02.019

Mirelman, A., Herman, T., Brozgol, M., Dorfman, M., Sprecher, E., Schweiger, A., . . . Hausdorff, J. M. (2012). Executive function and falls in older adults: new findings from a five-year prospective study link fall risk to cognition. PLoS One, 7(6), e40297. doi:10.1371/journal.pone.0040297

Moon, Y., McGinnis, R. S., Seagers, K., Motl, R. W., Sheth, N., Wright, J. A., Jr., . . . Sosnoff, J. J. (2017). Monitoring gait in multiple sclerosis with novel wearable motion sensors. PLoS One, 12(2), e0171346. doi:10.1371/journal.pone.0171346

Morello, R. T., Lowthian, J. A., Barker, A. L., McGinnes, R., Dunt, D., & Brand, C. (2013). Strategies for improving patient safety culture in hospitals: a systematic review. BMJ Qual Saf, 22(1), 11-18. doi:10.1136/bmjqs-2011-000582

Muro-de-la-Herran, A., Garcia-Zapirain, B., & Mendez-Zorrilla, A. (2014). Gait analysis methods: an overview of wearable and non-wearable systems, highlighting clinical applications. Sensors (Basel), 14(2), 3362-3394. doi:10.3390/s140203362

Najafi, B., Aminian, K., Loew, F., Blanc, Y., & Robert, P. A. (2002). Measurement of stand-sit and sit-stand transitions using a miniature gyroscope and its application in fall risk evaluation in the elderly. IEEE Trans Biomed Eng, 49(8), 843-851. doi:10.1109/TBME.2002.800763

National Council on Aging. (2016). Falls Prevention Facts. Retrieved from https://www.ncoa.org/news/resources-for-reporters/get-the-facts/falls-prevention-facts/

National Council on Aging. (2018). Healthy Aging Facts. Retrieved from https://www.ncoa.org/news/resources-for-reporters/get-the-facts/healthy-aging-facts/

Oberländer, K. (September 2015). Inertial Measurement Unit (IMU) Technology - Inverse Kinematics: Joint Considerations and the Maths for Deriving Anatomical Angles. Retrieved from

Ozdemir, A. T. (2016). An Analysis on Sensor Locations of the Human Body for Wearable Fall Detection Devices: Principles and Practice. Sensors (Basel), 16(8). doi:10.3390/s16081161

Ozdemir, A. T., & Barshan, B. (2014). Detecting falls with wearable sensors using machine learning techniques. Sensors (Basel), 14(6), 10691-10708. doi:10.3390/s140610691

Palermo, E., Rossi, S., Marini, F., Patane, F., & Cappa, P. (2014). Experimental evaluation of accuracy and repeatability of a novel body-to-sensor calibration procedure for inertial sensor-based gait analysis. Measurement, 52, 145-155. doi:10.1016/j.measurement.2014.03.004

Parisi, F., Ferrari, G., Baricich, A., D'Innocenzo, M., Cisari, C., & Mauro, A. (2016). Accurate Gait Analysis in Post-Stroke Patients using a Single Inertial Measurement Unit. 2016 Ieee 13th International Conference on Wearable and Implantable Body Sensor Networks (Bsn), 335-340.

Parkinson's Foundation. (2018). Understanding Parkinson's Statistics. Retrieved from http://parkinson.org/Understanding-Parkinsons/Causes-and-Statistics/Statistics

Perell, K. L., Nelson, A., Goldman, R. L., Luther, S. L., Prieto-Lewis, N., & Rubenstein, L. Z. (2001). Fall risk assessment measures: an analytic review. J Gerontol A Biol Sci Med Sci, 56(12), M761-766.

Pettinger, T. (July 20, 2016). The impact of an aging population on the economy. Retrieved from https://www.economicshelp.org/blog/8950/society/impact-ageing-population-economy/

Podsiadlo, D., & Richardson, S. (1991). The timed "Up & Go": a test of basic functional mobility for frail elderly persons. J Am Geriatr Soc, 39(2), 142-148.

Powell, L. M., AM,. (1995). The Activities-specific Balance Confidence (ABC) Scale. Journal of Gerontology Med Sci, 50(1), M28-34.

Preeti Jain. (2012). Magnetometers. Retrieved from https://www.engineersgarage.com/articles/magnetometer

Prieto, T. E., Myklebust, J. B., Hoffmann, R. G., Lovett, E. G., & Myklebust, B. M. (1996). Measures of postural steadiness: differences between healthy young and elderly adults. IEEE Trans Biomed Eng, 43(9), 956-966. doi:10.1109/10.532130

Rantz, M., Skubic, M., Abbott, C., Galambos, C., Popescu, M., Keller, J., . . . Petroski, G. F. (2015). Automated In-Home Fall Risk Assessment and Detection Sensor System for Elders. Gerontologist, 55 Suppl 1, S78-87. doi:10.1093/geront/gnv044

Rhudy, M. (2015). Increasing the Convergence Rate of the Extended Kalman Filter. Paper presented at the AIAA SciTech, Kissimmee, Florida.

Rispens, S. M., van Schooten, K. S., Pijnappels, M., Daffertshofer, A., Beek, P. J., & van Dieen, J. H. (2015). Identification of fall risk predictors in daily life measurements: gait characteristics' reliability and association with self-reported fall history. Neurorehabil Neural Repair, 29(1), 54-61. doi:10.1177/1545968314532031

Riva, F., Toebes, M. J., Pijnappels, M., Stagni, R., & van Dieen, J. H. (2013). Estimating fall risk with inertial sensors using gait stability measures that do not require step detection. Gait Posture, 38(2), 170-174. doi:10.1016/j.gaitpost.2013.05.002

Rob van Lummel. (Mar 30, 2017). Assessing Sit-to-Stand for Clinical Use. (Doctor), VRIJE UNIVERSITEIT,

Robert-Lachaine, X., Mecheri, H., Larue, C., & Plamondon, A. (2017). Effect of local magnetic field disturbances on inertial measurement units accuracy. Appl Ergon, 63, 123-132. doi:10.1016/j.apergo.2017.04.011

Roetenberg, D., Baten, C. T. M., & Veltink, P. H. (2007). Estimating body segment orientation by applying inertial and magnetic sensing near ferromagnetic materials. Ieee Transactions on Neural Systems and Rehabilitation Engineering, 15(3), 469-471. doi:10.1109/Tnspe.2007.903946

Roetenberg, D., Luinge, H. J., Baten, C. T., & Veltink, P. H. (2005). Compensation of magnetic disturbances improves inertial and magnetic sensing of human body segment orientation. IEEE Trans Neural Syst Rehabil Eng, 13(3), 395-405. doi:10.1109/TNSRE.2005.847353

Rubenstein, L. Z., Vivrette, R., Harker, J. O., Stevens, J. A., & Kramer, B. J. (2011). Validating an evidence-based, self-rated fall risk questionnaire (FRQ) for older adults. J Safety Res, 42(6), 493-499. doi:10.1016/j.jsr.2011.08.006

Sabatini, A. M. (2006). Quaternion-based extended Kalman filter for determining orientation by inertial and magnetic sensing. Ieee Transactions on Biomedical Engineering, 53(7), 1346-1356. doi:10.1109/Tmbe.2006.875664

Sabatini, A. M. (2011a). Estimating three-dimensional orientation of human body parts by inertial/magnetic sensing. Sensors (Basel), 11(2), 1489-1525. doi:10.3390/s110201489

Sabatini, A. M. (2011b). Kalman-Filter-Based Orientation Determination Using Inertial/Magnetic Sensors: Observability Analysis and Performance Evaluation. Sensors, 11(10), 9182-9206. doi:10.3390/s111009182

Sabatini, A. M., & Mannini, A. (2016). Ambulatory Assessment of Instantaneous Velocity during Walking Using Inertial Sensor Measurements. Sensors (Basel), 16(12). doi:10.3390/s16122206

Scarborough, D. M., McGibbon, C. A., & Krebs, D. E. (2007). Chair rise strategies in older adults with functional limitations. Journal of Rehabilitation Research and Development, 44(1), 33-42.

Seel, T., Raisch, J., & Schauer, T. (2014). IMU-based joint angle measurement for gait analysis. Sensors (Basel), 14(4), 6891-6909. doi:10.3390/s140406891

Shawe-Taylor, D. (2004). The Irish face: Redefining the Irish portrait. Apollo-the International Magazine of Art and Antiques, 160(512), 86-87.

Shiau, J. W., IC; . (2013). Unscented Kalman Filtering for Attitude Determination Using Mems Sensors. J. Appl. Sci. Eng., 16, 165-176.

Shumway-Cook, A., Brauer, S., & Woollacott, M. (2000). Predicting the probability for falls in community-dwelling older adults using the Timed Up & Go Test. Physical Therapy, 80(9), 896-903.

Sivaranjith. (Mar 12, 2018). Piezoelectric-Accelerometer. Retrieved from https://automationforum.co/vibration-measuring-insruments-accelerometers/piezoelectric-accelerometer/

Spoor, C. W., & Veldpaus, F. E. (1980). Rigid body motion calculated from spatial co-ordinates of markers. Journal of Biomechanics, 13(4), 391-393.

Steins, D., Sheret, I., Dawes, H., Esser, P., & Collett, J. (2014). A smart device inertial-sensing method for gait analysis. Journal of Biomechanics, 47(15), 3780-3785. doi:10.1016/j.jbiomech.2014.06.014

Stevens, J. A. (2005). Falls among older adults--risk factors and prevention strategies. J Safety Res, 36(4), 409-411. doi:10.1016/j.jsr.2005.08.001

Stevens, J. A. (2013). The STEADI Tool Kit: A Fall Prevention Resource for Health Care Providers. IHS Prim Care Provid, 39(9), 162-166.

Sun, R., & Sosnoff, J. J. (2018). Novel sensing technology in fall risk assessment in older adults: a systematic review. BMC Geriatr, 18(1), 14. doi:10.1186/s12877-018-0706-6

Tanaka, S., Motoi, K., Nogawa, M., & Yamakoshi, K. (2004). A new portable device for ambulatory monitoring of human posture and walking velocity using miniature accelerometers and gyroscope. Conf Proc IEEE Eng Med Biol Soc, 3, 2283-2286. doi:10.1109/IEMBS.2004.1403663

Taylor, L., Miller, E., & Kaufman, K. R. (2017). Static and dynamic validation of inertial measurement units. Gait Posture, 57, 80-84. doi:10.1016/j.gaitpost.2017.05.026

Thorbahn, L. D. B., & Newton, R. A. (1996). Use of the Berg balance test to predict falls in elderly persons. Physical Therapy, 76(6), 576-583. doi:DOI 10.1093/ptj/76.6.576

Tinetti, M. E. (1986). Performance-oriented assessment of mobility problems in elderly patients. J Am Geriatr Soc, 34(2), 119-126.

Titterton, D. W., J,. (2004). Strapdown Inertial Navigation Technology (Electromagnetics and Radar) (2nd ed.).

Trawny, N. R., SI. (2005). Indirect Kalman Filter for 3D Attitude Estimation. Retrieved from

Trojaniello, D., Ravaschio, A., Hausdorff, J. M., & Cereatti, A. (2015a). Comparative assessment of different methods for the estimation of gait temporal parameters using a single inertial sensor: application to elderly, post-stroke, Parkinson's disease and Huntington's disease subjects. Gait Posture, 42(3), 310-316. doi:10.1016/j.gaitpost.2015.06.008

Trojaniello, D., Ravaschio, A., Hausdorff, J. M., & Cereatti, A. (2015b). Comparative assessment of different methods for the estimation of gait temporal parameters using a single inertial sensor: application to elderly, post-stroke, Parkinson's disease and Huntington's disease subjects. Gait & Posture, 42(3), 310-316. doi:10.1016/j.gaitpost.2015.06.008

van Schooten, K. S., Pijnappels, M., Rispens, S. M., Elders, P. J., Lips, P., & van Dieen, J. H. (2015). Ambulatory fall-risk assessment: amount and quality of daily-life gait predict falls in older adults. J Gerontol A Biol Sci Med Sci, 70(5), 608-615. doi:10.1093/gerona/glu225

VectorNav Technologies, L. (2011). Magnetometer. Retrieved from https://www.vectornav.com/support/library/magnetometer

Veltink, P. H., Bussmann, H. B., de Vries, W., Martens, W. L., & Van Lummel, R. C. (1996). Detection of static and dynamic activities using uniaxial accelerometers. IEEE Trans Rehabil Eng, 4(4), 375-385.

Welch, G., & Foxlin, E. (2002). Motion tracking: No silver bullet, but a respectable arsenal. Ieee Computer Graphics and Applications, 22(6), 24-38. doi:Doi 10.1109/Mcg.2002.1046626

Whitney, S. L., Wrisley, D. M., Marchetti, G. F., Gee, M. A., Redfern, M. S., & Furman, J. M. (2005). Clinical measurement of sit-to-stand performance in people with balance disorders: validity of data for the Five-Times-Sit-to-Stand Test. Physical Therapy, 85(10), 1034-1045.

Wikipedia. (2018). Extended Kalman Filter. Retrieved from https://en.wikipedia.org/wiki/Extended_Kalman_filter

Winter, D. (1990). Biomechanics and Motor Control of Human Movement. Hoboken, NJ: John Wiley & Sons.

Wu, J., Zhou, Z. B., Chen, J. J., Fourati, H., & Li, R. (2016). Fast Complementary Filter for Attitude Estimation Using Low-Cost MARG Sensors. Ieee Sensors Journal, 16(18), 6997-7007. doi:10.1109/Jsen.2016.2589660

Yang, S., Zhang, J. T., Novak, A. C., Brouwer, B., & Li, Q. (2013). Estimation of spatio-temporal parameters for post-stroke hemiparetic gait using inertial sensors. Gait Posture, 37(3), 354-358. doi:10.1016/j.gaitpost.2012.07.032

Yogev, G., Plotnik, M., Peretz, C., Giladi, N., & Hausdorff, J. M. (2007). Gait asymmetry in patients with Parkinson's disease and elderly fallers: when does the bilateral coordination of gait require attention? Exp Brain Res, 177(3), 336-346. doi:10.1007/s00221-006-0676-3

Yuan, X. B., Yu, S., Zhang, S. Z., Wang, G. P., & Liu, S. (2015). Quaternion-Based Unscented Kalman Filter for Accurate Indoor Heading Estimation Using Wearable Multi-Sensor System. Sensors, 15(5), 10872-10890. doi:10.3390/s150510872

Yun, X. P., & Bachmann, E. R. (2006). Design, implementation, and experimental results of a quaternion-based Kalman filter for human body motion tracking. Ieee Transactions on Robotics, 22(6), 1216-1227. doi:10.1109/Tro.2006.886270

Yuwono, M., Moulton, B. D., Su, S. W., Celler, B. G., & Nguyen, H. T. (2012). Unsupervised machine-learning method for improving the performance of ambulatory fall-detection systems. Biomedical Engineering Online, 11. doi:Artn 910.1186/1475-925x-11-9

Zago, M., Sforza, C., Pacifici, I., Cimolin, V., Camerota, F., Celletti, C., . . . Galli, M. (2018). Gait evaluation using inertial measurement units in subjects with Parkinson's disease. J Electromyogr Kinesiol, 42, 44-48. doi:10.1016/j.jelekin.2018.06.009

Zampella, F. K., M.; Robertson, P.; Jiménez, A. (2012). Unscented Kalman Filter and Magnetic Angular Rate Update (MARU) for an Improved Pedestrian Dead-Reckoning. Paper presented at the In Proceedings of the IEEE/ION Position Location and Navigation Symposium, Myrtle Beach, SC, USA,.

Zhao, L., & Yeatman, E. M. (2007). Micro Capacitive Tilt Sensor for Human Body Movement Detection. In S. Leonhardt, T. Falck, & P. Mähönen (Eds.), 4th International Workshop on Wearable and Implantable Body Sensor Networks (BSN 2007) (Vol. 13, pp. 195-200): Springer Berlin Heidelberg.

Zijlstra, W. (2004). Assessment of spatio-temporal parameters during unconstrained walking. Eur J Appl Physiol, 92(1-2), 39-44. doi:10.1007/s00421-004-1041-5

Zijlstra, W., & Hof, A. L. (2003). Assessment of spatio-temporal gait parameters from trunk accelerations during human walking. Gait Posture, 18(2), 1-10.